



TALLINN UNIVERSITY OF TECHNOLOGY
SCHOOL OF ENGINEERING
DEPARTMENT OF CIVIL ENGINEERING AND ARCHITECTURE

**NUMERICAL STUDIES OF THE BEHAVIOUR OF
COMPOSITE BEAMS IN FIRE**

KOMPOSIITTALADE KÄITUMISE ANALÜÜS TULEKAHJUS

MASTER THESIS

Student: Mohamed Anas Mahmoud Sakr

Student code: 204228 EAXM

Supervisor: Ivar Talvik, Associate Professor
TalTech University

Advisor: Jari Puttonen, Professor
Aalto University

Advisor: Wei Lu, Senior Lecturer
Aalto University

Tallinn 2022

AUTHOR'S DECLARATION

Hereby I declare that I have written this thesis independently.

No academic degree has been applied for based on this material. All works, major viewpoints and data of the other authors used in this thesis have been referenced.

"May" 15th, 2022

Author:

/signature /

Thesis is in accordance with terms and requirements

"....." 20....

Supervisor:

/signature/

Accepted for defence

"....."20...

Chairman of theses defence commission:

/name and signature/

Non-exclusive licence for reproduction and publication of a graduation thesis¹

I Mohamed Anas Mahmoud Sakr

1. grant Tallinn University of Technology free licence (non-exclusive licence) for my thesis
NUMERICAL STUDIES OF THE BEHAVIOUR OF COMPOSITE BEAMS IN FIRE
supervised by Ivar Talvik

1.1 to be reproduced for the purposes of preservation and electronic publication of the
graduation thesis, incl. to be entered in the digital collection of the library of Tallinn
University of Technology until expiry of the term of copyright;

1.2 to be published via the web of Tallinn University of Technology, incl. to be entered
in the digital collection of the library of Tallinn University of Technology until expiry
of the term of copyright.

2. I am aware that the author also retains the rights specified in clause 1 of the non-
exclusive licence.

3. I confirm that granting the non-exclusive licence does not infringe other persons'
intellectual property rights, the rights arising from the Personal Data Protection Act or
rights arising from other legislation.

15.05.2022

¹ *The non-exclusive licence is not valid during the validity of access restriction indicated in the student's application for restriction on access to the graduation thesis that has been signed by the school's dean, except in case of the university's right to reproduce the thesis for preservation purposes only. If a graduation thesis is based on the joint creative activity of two or more persons and the co-author(s) has/have not granted, by the set deadline, the student defending his/her graduation thesis consent to reproduce and publish the graduation thesis in compliance with clauses 1.1 and 1.2 of the non-exclusive licence, the non-exclusive license shall not be valid for the period.*

DEPARTMENT OF CIVIL ENGINEERING AND ARCHITECTURE
THESIS TASK

Student: Mohamed Anas Mahmoud Sakr, 204228 EAXM

Study programme, EAXM15/18 - Building and Infrastructure Engineering

main speciality: structural engineering

Supervisor: Associate Professor, Ivar Talvik, +3726202410, ivar.talvik@taltech.ee

Advisor: Professor, Jari Puttonen, +358503841782, jari.puttonen@aalto.fi

Advisor: Senior Lecturer, Wei Lu, +358503502974, wei.2.lu@aalto.fi

Thesis topic:

(in English) NUMERICAL STUDIES OF THE BEHAVIOUR OF COMPOSITE BEAMS IN FIRE

(in Estonian) KOMPOSIITTALADE KÄITUMISE ANALÜÜS TULEKAHJUS

Thesis main objectives:

1. Understanding the different fire scenarios and its effect on structures
2. Understanding structural fire analysis procedure and collecting thermal and mechanical material data for simulation.
3. Understanding the advanced calculation method and how to simulate the steel and composite beam in different fire scenarios.
4. Understanding the behaviour of the steel and composite beam under fire.

Thesis tasks and time schedule:

No	Task description	Deadline
1.	Verify the FE model by the simple steel beam exposed to ISO fire.	March 22
2.	Study the behaviour of composite beam with simple shear connection and validate with benchmarking	April 22
3.	Study the load-carrying mechanism of the composite beam exposed to different fire scenarios	May 22

Language: English **Deadline for submission of thesis:** "May" 19th, 2022 a

Student: Mohamed Anas Mahmoud Sakr *Mohamed Sakr* "May" 15th, 2022 a
.....
/signature/

Supervisor: Ivar Talvik "May" 15th, 2022 a
/signature/

Advisor: Jari Puttonen *Jari* "May" 15th, 2022 a
/signature/

Advisor: Wei Lu *Wei* "May" 15th, 2022 a
/signature/

Head of study programme: Simo Ilomets "May" 15th, 2022 a
/signature/

Terms of thesis closed defence and/or restricted access conditions to be formulated on the reverse side

ACKNOWLEDGMENTS

This master's thesis has been written for Tallinn University of technology with the collaboration of Aalto university with an aim to study the behaviour of steel-concrete composite beams and find the criteria to characterize the limit state of composite beams exposed to fire using Abaqus. The thesis is financially supported by the European Union, namely the Erasmus+ Scholarship, as without this funding I would not have the opportunity to participate in this master's degree course.

Firstly, thanks be to God almighty for the completion of the research.

I would like to express my gratitude to my supervisor prof. Ivar Talvik for his support and encouragement. I would like to express my deepest gratitude to my advisors Prof. Jari Puttonen and Dr Wei Lu, for their continuous support, guidance, and constructive criticism during this thesis period. Their ideas, recommendations, and contributions were very beneficial and very well-acknowledged to this work and me as a person. For their support and motivation despite all the circumstances that occurred during this work.

I would also like to express my appreciation to Mr Saani Shakil for his endeavours and time in helping me run this project. To my friends, who showed generous support and motivation for me while working on my thesis.

Most importantly, I would like to thank my family, the most important persons in my life for everything they did and keep doing to support me. I would not reach this point in my life without you. Thank you for being in my life.

CONTENTS

CONTENTS.....	VII
LIST OF FIGURES	IX
LIST OF TABLES	XII
1. INTRODUCTION	1
1.1 Background	1
1.2 Objectives and scope of the research.....	3
1.3 Outline of the project work	4
2. LITERATURE REVIEW	5
2.1 Fire scenarios	6
2.1.1 Standard fire	6
2.1.2 Parametric fire	7
2.2 Load-carrying mechanism and limit state of beams.....	9
2.3 Design guidelines	11
2.3.1 Fire model.....	12
2.3.2 Thermal response model.....	12
2.3.3 Structural response model	12
2.4 Previous research on structural fire resistance of elements and connection.....	13
3. FINITE ELEMENT MODELLING OF STEEL BEAM EXPOSED TO NOMINAL FIRE	14
3.1 Studied steel beam	14
3.2 Thermal analysis model	16
3.2.1 FE meshes and boundary conditions.....	16
3.2.2 Thermal material properties of steel	18
3.3 Structural analysis model.....	20
3.3.1 FE meshes and boundary conditions.....	20
3.3.2 Mechanical material properties of steel S355	22
3.4 Verification of FE models	25
3.4.1 verification of thermal analysis model	25
3.4.2 Verification of the model for mechanical analysis	27
3.5 Load-bearing mechanism of steel beam.....	29
3.5.1 Four-stage mechanism	29
4. BEHAVIOUR OF COMPOSITE BEAM EXPOSED TO FIRE	35
4.1 Benchmark tests on composite beams at elevated temperatures	35

4.1.1	Fire test description.....	35
4.1.2	Test CB-3.....	37
4.2	Model for thermal analysis.....	40
4.2.1	FE geometry and meshes.....	40
4.2.2	Thermal boundary conditions.....	43
4.2.3	Thermal material properties of concrete.....	46
4.3	Model for structural analyses.....	48
4.3.1	FE geometry and meshes.....	48
4.3.2	Mechanical properties of the material.....	51
4.4	Validation of FE models.....	58
4.4.1	Validation of thermal analysis models.....	58
4.4.2	Validation of mechanical analysis models.....	65
4.5	Load-bearing mechanism of composite beam.....	67
4.5.1	Four-stage mechanism based on Case 1.....	67
4.5.2	Four-stage mechanism: Case 2.....	69
4.6	Effect of load ratio on the behaviour of the composite beam.....	75
4.6.1	Response of composite beam with smaller load: Case 4.....	75
4.6.2	Behaviour of shear studs at different load ratios.....	79
4.6.3	Behaviour of beam-to-column connections at different load ratios.....	83
5.	CONCLUSIONS AND FUTURE RESEARCH.....	86
	SUMMARY.....	88
	KOKKUVÕTE.....	89
	REFERENCES.....	90

LIST OF FIGURES

Figure 2-1: The three main criteria for fire resistance analysis and design [9].....	5
Figure 2-2: Schematic representation of the fire curves [17]	7
Figure 2-3: Comparison between parametric fire and real fire	8
Figure 2-4: The comparison between ISO standard fire and Parametric fire	8
Figure 2-5: Typical fire response of a restrained steel beam that fails by yielding [24].	10
Figure 2-6: Structural fire design approaches [26].....	11
Figure 3-1: Simply supported beam with a profile of IPE 200 (a) beam layout [mm] (b) dimension of the cross-section [mm].....	14
Figure 3-2: Standard fire curve [17].	15
Figure 3-3: Cross-section of FE model with heating boundary conditions for IPE200 FE model with heating sides.....	16
Figure 3-4: Thermal conductivity of steel as a function of temperature [32].....	18
Figure 3-5: Specific heat of steel as a function of the temperature [32]	19
Figure 3-6: FE model of I-beam	20
Figure 3-7: Load curve for applying mechanical loading.....	21
Figure 3-8: Curve for applying temperature loading due to fire.....	21
Figure 3-9: Reduction factors of the steel S355 stress-strain relationship at elevated temperatures [32]	23
Figure 3-10: Modulus of elasticity for steel S355 as a function of temperature [32].....	23
Figure 3-11: stress-strain curves for S355 at different temperatures [32]	23
Figure 3-12: Relative thermal elongation of steel as a function of the temperature [32] .	24
Figure 3-13: Comparison of temperature history for bottom flange.....	25
Figure 3-14: Comparison of temperature history for web.....	26
Figure 3-15: Comparison of temperature history for top flange	26
Figure 3-16: Temperature distribution of the beam cross-section.....	26
Figure 3-17: Deflection manually calculation.....	27
Figure 3-18: Displacement calculated by the FEM and manually	27
Figure 3-19: Critical temperature manually calculation based on Normogram curves.....	28
Figure 3-20: Max principal stresses at the mid-span of the beam as a function of time ...	29
Figure 3-21: Axial reactions at the supports as a function of time	30
Figure 3-22: Mid-span deflection as a time function	30
Figure 3-23: Beam stresses after loading step - 0.25 ratio	31
Figure 3-24: Beam stresses at 110 sec– 0.25 ratio.....	32
Figure 3-25: Beam stresses at 700 sec– 0.25 ratio.....	32
Figure 3-26: Beam stresses at 1200 sec– 0.25 ratio.....	32
Figure 3-27: Beam stresses after fire step catenary action stage - 0.25 ratio	33
Figure 3-28: Beam stresses after loading step - 0.5 ratio	33
Figure 3-29: Beam stresses at 110 sec – 0.5 ratio	33
Figure 3-30: Beam stresses at 500 sec– 0.5 ratio.....	34
Figure 3-31: Beam stresses at 730 sec – 0.5 ratio	34
Figure 3-32: Beam stresses after fire step catenary action stage - 0.5 ratio	34
Figure 4-1: Test setup for composite beam exposed to fire [28].....	36

Figure 4-2: Elevation of loading for composite beam specimens [29].....	36
Figure 4-3: Shear-tab connection geometry [29]	37
Figure 4-4: Loading and heating configuration [28]	38
Figure 4-5: Heating layout of the composite beam cross-section [29]	38
Figure 4-6: Heating and cooling curves for the steel beam and concrete slab in test.....	39
Figure 4-7: Frame cross-section geometry.....	40
Figure 4-8: Overall 3D FEM model.....	41
Figure 4-9: Zoom-in view of the connection	42
Figure 4-10: Exposed surface to fire.....	43
Figure 4-11: Unexposed surface to fire	43
Figure 4-12: Beam and slab heating and cooling rate.....	44
Figure 4-13: heated surface temperature histories	45
Figure 4-14: thermal conductivity of normal weight concrete as a function of temperature [34].....	46
Figure 4-15: Specific heat as a function of temperature [34]	47
Figure 4-16: Temperature-dependent force–slip behaviour for shear connectors with flat concrete slab [30]	48
Figure 4-17: Close view of the lateral bracing boundary condition	50
Figure 4-18: Close view of FE model loading step.....	50
Figure 4-19: Reduction factors for the stress-strain relationship of bolts at elevated temperatures [32]	52
Figure 4-20: stress-strain curves for bolt 8.8 at different temperatures [32].....	52
Figure 4-21: Reduction factors of the steel A500 stress-strain relationship at elevated temperatures [34]	54
Figure 4-22: Modulus of elasticity for steel A500 as a function of temperature [34]	54
Figure 4-23: Stress-strain curves for A500 at different temperatures [32]	54
Figure 4-24: Values of two main parameters of the stress-strain relationships of normal weight concrete (NC) and lightweight concrete (LC) at elevated temperatures [34].....	55
Figure 4-25: Modulus of elasticity as a function of temperature [34]	56
Figure 4-26: Stress-strain curves for compression in concrete at different temperatures [34].....	56
Figure 4-27: Stress-strain curves for tension in C30 at elevated temperatures [32].....	56
Figure 4-28: thermal elongation of concrete as a function of the temperature according to EN1992-1-2 [2004].....	57
Figure 4-29: Thermocouple instrumentation layout.....	58
Figure 4-30: Temperature verification for composite beam Test CB-3 with Case 1 results	59
Figure 4-31: Bottom flange temperature history Case 1	59
Figure 4-32: Web temperature history Case 1	60
Figure 4-33: Bottom slab temperature history Case 1	60
Figure 4-34: Cross-section temperature profile at the end of heating phase Case 1	61
Figure 4-35: Cross-section temperature profile at the end of cooling phase Case 1	61
Figure 4-36: Temperature verification for composite beam Test CB-3 with Case 2 results	62
Figure 4-37: Temperature profile at the end of heating phase Case 2	62
Figure 4-38: Temperature profile at the end of cooling phase Case 2	62

Figure 4-39: Temperature verification for composite beam Test CB-3 with Case 3 results	63
Figure 4-40: Temperature profile at the end of heating phase Case 3	63
Figure 4-41: Temperature profile at the end of cooling phase Case 3	64
Figure 4-42: Midspan displacement versus average bottom flange temperature	66
Figure 4-43: Quarter-point displacement versus average bottom flange temperature	66
Figure 4-44: Axial force in the connection as a function of time in case 1	68
Figure 4-45: Vertical displacement of the beam as a function of time in case 1	68
Figure 4-46: Axial force in the connection as a function of time in case 2	70
Figure 4-47: Vertical mid-span displacement of the beam as a function of time in case 2	70
Figure 4-48: Vertical quarter-span displacement of the beam as a function of time in case 2	71
Figure 4-49: Beam stresses after loading step	71
Figure 4-50: Beam stresses before material degradation	72
Figure 4-51: Beam stresses maximum compressive force	72
Figure 4-52: Beam stresses before runaway behaviour	73
Figure 4-53: Beam stresses after the heating phase	73
Figure 4-54: Beam stresses at zero axial force	74
Figure 4-55: Beam stresses after cooling phase	74
Figure 4-56: Heating and cooling rate for the structure Case 4	75
Figure 4-57: Temperature histories of the structure Case 4	76
Figure 4-58: Temperature profile at the end of heating phase at 100 minutes Case 4	76
Figure 4-59: Temperature profile at the end of cooling phase at 150 minutes Case 4	76
Figure 4-60: Axial force at the connection as a function of time in case 4	77
Figure 4-61: Vertical mid-span deflection as a function of time in case 4	78
Figure 4-62: Vertical quarter-span displacement of the beam as a function of time in case 4	78
Figure 4-63: Temperature histories in the shear studs	79
Figure 4-64: Shear studs' slip as a function of time	80
Figure 4-65: Maximum absolute principal stress contour at the bottom surface of concrete slab at (a) Point 0 (b) Point 3	81
Figure 4-66: Maximum absolute principal stress contour at the bottom surface of concrete slab at (a) Point 3* (b) Point 4 (c) Point 5	82
Figure 4-67: Von-Mises stress in the shear plate at Point 2	84
Figure 4-68: Von-Mises stress in bolts at Point 2	84
Figure 4-69: Von-Mises stress in the shear plate at Point 5	85
Figure 4-70: Von-Mises stress in bolts at Point 5	85

LIST OF TABLES

Table 3-1: Properties of steel S355 at the ambient temperature of 20°C	22
Table 3-2: Temperature at 200 mm deflection	28
Table 4-1: Test Matrix for Simple (Shear) Connections of Composite Beams [27].....	37
Table 4-2: Summary of the studied cases	39
Table 4-3: Properties of steel grade 8.8 at ambient temperature	51
Table 4-4: Properties of steel A500 at ambient temperature.....	53
Table 4-5: Properties of siliceous concrete at ambient temperature	55

1. INTRODUCTION

1.1 Background

The composite structure is a component composed of two or more parts of different materials. The main advantage of composite elements is that the properties of individual materials are often combined into a single entity and typically perform better than individual parts. The most common type of composite element in construction is steel and concrete composites, which are very efficient and lightweight units. The composite action between steel and concrete allows for creative structures with large open spaces, thus providing savings of volume and reducing carbon dioxide emissions during the design stage and construction. The use of composite structures increased recently in the construction industry due to their improved durability, lower labour costs, a good bond between the components, improved integrity, and accelerated project schedules. Carbon dioxide emissions can be effectively reduced by applying environmentally friendly design strategies to determine the proportions of the material components in the composite members [1].

Composite floor systems use steel beams to connect them to concrete floor slabs. It uses the advantage of both steel and concrete [2]. The most commonly used type of floor slab in a composite deck system is a concrete slab placed on a profiled metal deck with shear studs to connect them to the steel beam. Sheet metal acts as a framework for casting slabs, resulting in faster construction speeds, shorter overall project times and reduced weight of steel members [2]. Composite beams with precast hollow core slabs are another composite slab system. Precast slabs are used with chemical anchors to work with steel beams. The slim floor uses a special beam with a lower flange that is wider than the upper flange. This arrangement enables the floor slabs to be mounted directly on the lower flange of the beam. This type of slab system has some advantages. It reduces the floor thickness, increases fire resistance, and leads to lighter structures. Therefore, it is widely used in multi-storey designs and tall buildings [3]. However, due to the bottom flange of the beam being directly exposed to fire, either fire protections or fire reinforcement are necessary to reach a higher fire resistance rate.

Fire poses an ongoing danger to these structural components. Therefore, the impact of fire on the behaviour of composite structures must be evaluated and included in the design. The fire scenario is one of the main factors affecting the disproportionate collapse of structures, and an essential step for performance-based fire safety structural design. The impact of fire scenarios depends on the size of compartments (small or large) and the heating location of the fire regarding the location of the member. It is reasonable to assume uniform heating in a small-size compartment. In the large size compartment, the member can be heated locally or non-uniformly. Temperature growth rate varies in different elements of the composite floor system depending on the physical material properties and exposition to fire. The steel beam is directly exposed to fire, concrete has better heat resistance than steel, and shear studs are embedded in concrete but experience elevated temperatures indirectly through heat transfer from the upper flange of the steel beam, which affects the composite action. A large amount of experimental and theoretical investigations have been carried out on the

interaction of protected and unprotected composite beams with slabs in floor systems in different fire scenarios [4].

Fire-rated building design options in the European Building Design Code (EN EN1994-1-2 [2005]) are standard fire and parametric time-temperature curves. Standard fires are used for performing rating structural members by fire tests. Standard fire curves cannot show the behaviour of real fires, the four stages of which are ignition, growth, full development, and disintegration of fire. Standard fire curves only represent the fully developed fire stage and are the worst fire case in an enclosure.

To better represent a realistic fire, natural fire (or parametric fire) curves are developed by considering space geometry, ventilation condition, fire load density, and thermal properties of materials of building enclosures. One difference between standard and normal fire curves from a structural fire design point of view is that the latter represents the cooling stage. It was found that the frame may collapse during the cooling phase of a well-ventilated fire because the temperature does not drop quickly in the column due to the large cross-section compared to the beam cross-section in multi-floor structures with small and medium spans [5].

However, the parametric fire curves are based on tests in a small compartment and therefore have limitations in their applicability to large compartments over 100m². In addition, the standard fire curves and the parametric time-temperature curves are based on an unrealistic assumption of uniform fire conditions in the room. In large open-plan compartments, travelling fires have been observed resulting in highly non-uniform temperature distributions within the compartment [6]. The travelling fire methodology postulates that fires may burn locally and move across the entire floor plate over a while in large compartments [7]. It became determined that the travelling fires produce non-uniform temperatures inside the compartment irrespective of the airflow situation even though the value of this non-uniformity is associated with the hole sizes.

1.2 Objectives and scope of the research

The objective of this research is to study the behaviour of composite beams under different fire load scenarios. A sequentially coupled thermal and structural analysis procedure will be performed using ABAQUS finite element (FE) software. A heat transfer analysis is performed to predict the temperature development of composite members. By using the temperature received from the thermal analyses, a subsequent structural analysis is performed to study the response of the composite beams inside a simple composite frame.

The research will be carried out in the following steps:

- Study the behaviour of the steel beam exposed to nominal fire
- Study the behaviour of the composite steel beam exposed to test fire with heating and cooling phases using the FE models validated by benchmark tests.
- Study the interactions between the steel beam and concrete slab and beam-to-column connections of the same composite beam under different loading and test fire scenarios.

The expected results include:

- Characterization of the behaviour of the steel beam exposed to the nominal fire
- Characterization of the behaviour of the composite beam and connections exposed to the different loading and fire scenarios.
- Characterization of interactions of the steel beam, concrete slab and beam-to-column connections of composite beams exposed to the different loading and fire scenarios.

For the nominal fire, a simple steel beam is simulated as a 3D element with pinned-pinned support to get the temperature inside the beam during the heating step, the displacement in the mid-span and axial force at the boundary condition of the beam during the mechanical loading and fire step. The model will be validated with the theoretical prediction equation from Eurocode.

For the test fires, the structure studied is a 3D composite beam with a connection with steel columns. The composite beam is connected to the steel columns at the ends with simple shear tab connections. The studied frame is exposed to test fires with both heating and cooling phases. This model will be validated with the actual experimental results.

The mechanical fire load applied to the studied frame include the self-weight of the concrete slab and the mechanical load taken according to the design code. The thermal elongation of the structural members is considered inside the FE models.

1.3 Outline of the project work

The report consists of five chapters. Following the current introduction chapter, the four remaining chapter's purposes is being outlined within this section

- Chapter 2 contains a literature review of the basic knowledge of structural fire design and the finite element method. This chapter aims to introduce the structural fire engineering design approach and use the finite element method for performance-based fire design. The chapter provides also an overview of nominal and parametric fire scenarios, and further dived into structural fire design and structural fire analysis using FEM. Summaries of previous research related to the performance of composite structures during fire scenarios have been used in the report.
- Chapter 3 contains the finite element model of a simple steel beam exposed to nominal fire. Including the studied structure, and thermal and mechanical material properties of steel that has been used in thermal and structural analyses. Validation of the model and the results with the theoretical prediction equation from Eurocode. Defining beam load-carrying mechanism during different stages of the fire.
- Chapter 4 contains the finite element model of the composite beam and connections exposed to test-fire scenarios. thermal and mechanical material properties at an ambient and elevated temperature for concrete slab, bolts, and reinforcing steel that has been used in a thermal and mechanical model. Different methods to validate the thermal and mechanical models with the test results. Defining beam load-carrying mechanism during different stages of the fire. The beam behaviour under different loading and test fire scenarios. Beam to column connection and shear stud behaviour during different load and fire cases
- Chapter 5 contains the conclusion and future research

2. LITERATURE REVIEW

This chapter provides basic knowledge of structural fire design and finite element methods. The objective of this chapter is to introduce different fire scenarios, loading beam behaviour under fire, structural fire engineering design approaches and implementation of finite element methods for heat transfer analysis and structural analysis for performance-based fire design.

Experimental studies have shown that to model the mechanical behaviour of steel sections at elevated temperatures, an appropriate form of fire testing will be required. McCann et al. [8], found that the transient state or time-dependent test method is a close simulation for the steel material in fire, by increasing the heat at a constant rate of about 10 degrees Celsius. Transient state tests allow the development of stress-strain characteristics, which is important when studying potential relationships of heat stress.

To analyse the load-bearing capacity and to allocate the appropriate level of fire safety at intervals during exposure to fire, in-depth knowledge of the mechanical and thermal properties of steel must first be understood. Buchanan et al. [9] explained that some factors such as mechanical properties of the section, fire loading, geometry of the element, fire properties, etc., all help in determining the bearing capacity of a structure. The fire resistance of the structure constitutes three main criteria for the design and analysis of fire resistance in the Eurocode (R, E, I) as shown in Figure 2-1 which are

- The load-bearing ability of the structure "R"
- Thermal insulation separation "E"
- The integrity separation function "I"

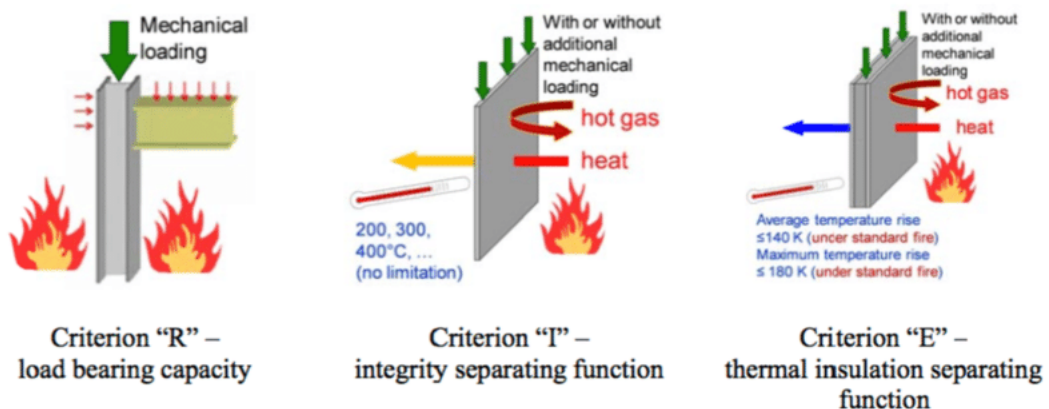


Figure 2-1: The three main criteria for fire resistance analysis and design [10]

2.1 Fire scenarios

EN1994-1-2 [2005] states that advanced computation models should provide a realistic analysis of structures exposed to fire. It should be based on the underlying physical behaviour in such a way that it results in a reliable approximation of the expected behaviour of the relevant structural component under fire conditions. The advanced calculation models may be used for separate members, subassemblies, or the entire structure [11].

Advanced calculation methods, also called thermomechanical methods, include two calculation steps: thermal analysis, which is intended to assess the temperature development inside structural elements, and mechanical analysis considers the effects of temperature and other loads on the structural behaviour. Thermal response analysis should be based on the recognized principles and assumptions of heat transfer theory, considering the relevant thermal actions and temperature-dependent thermal properties of materials. Mechanical response analysis should be based on the recognized principles and assumptions of structural mechanics, considering the effects of deterioration of mechanical properties with temperature. The main studied beam is exposed to test fire with heating and cooling phases.

2.1.1 Standard fire

The first attempts at testing to understand structural performance in fire led to the Standard Temperature-time Curve, first published in 1917 [12]. The curve and associated test methods are given in standards, such as BS 476 [13], ISO 834 [14], and ASTM E119 [15], which have formed the basis for the fire rating systems in most buildings codes and standards worldwide. The curve came from aggregating the results of various post-flashover fire tests into a single perfect curve. The tests that fuelled the development of the standard fire were intended to represent the worst-case fires in enclosures to determine if the structure could withstand fatigue. However, these tests and the creation of a standard fire were conducted before much scientific understanding of fire dynamics was available. Thus, standard fire, unlike real fire, has a relatively slow rate of growth which was largely driven using kilns heated with hand-heated wood fuel. Its temperature never drops due to fire decay and is independent of building properties such as engineering, ventilation, and fuel loading [16] [9]. Moreover, standard fire does not accurately reflect the nature of real fires that do not heat building elements uniformly [17].

Traditional methods have known limitations in their application. For example, EN1991-1-2 [2002] states that parametric curves are only valid for compartments with floor areas of up to 500 m² and heights up to 4 m. The enclosure must also not have openings through the roof and compartment liners are limited to thermal inertia between 1000 and 2200 J/m² s^{1/2} K, which means that highly conductive linings such as glass and highly insulating material cannot be considered [18]. As a result, common features in modern construction such as large enclosures, high ceilings, atria, large open spaces, multiple floors connected by voids and glass facades are excluded from the scope of application of current methodologies [19]. It should be noted that no definition of a large compartment could be found in the literature. In terms of the standard, the interpretation may be that large means an area of more than 500 m². Furthermore, there is not enough empirical data and theoretical knowledge to enable the development of such a definition.

In general, for the purposes of structural analysis, the effect of fire is calculated utilizing the temperature-time curve affecting the structural system to be evaluated. This temperature is the temperature of the gas around the members exposed to fire. The basic form for representing the evolution of gas temperature is based on so-called nominal temperature-time curves. The nominal curves allowed by EN1991-1-2 [2002] are the standard curve (ETK), the external fire curve, and the hydrocarbon curve [20]. These fire curves are not dependent on any properties of the fire-exposed structure, such as fire carrying or ventilation properties, and therefore do not represent any real fire. Nominal curves present a schematically drawn exponential mathematical formula shown in Figure 2-2.

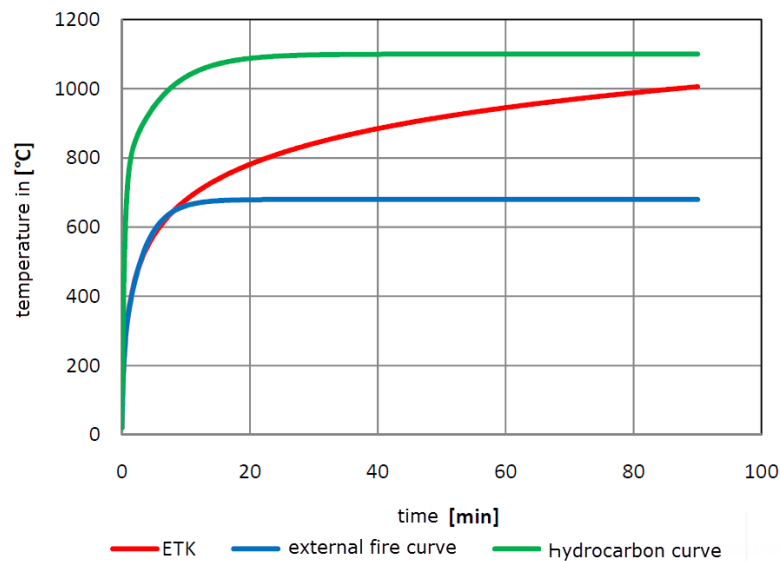


Figure 2-2: Schematic representation of the fire curves [18]

2.1.2 Parametric fire

A more realistic approach is also permitted by EN1991-1-2 [2002] based on simulations of natural fire. Parametric temperature curves are the simplest way to simulate a natural fire, where the temperature evolution is assumed to be constant over the entire chamber in the same way as it is assumed for the case of nominal fire curves. However, the temperature evolution of the parametric curves depends on the physical parameters of the compartment and thus represents a realistic approach to the evolution of a real fire. The distinguishing feature of the parametric curves is the presence of a descending branch representing the cooling (or decay) phase of the fire which is not accounted for in the nominal curves.

Real fire undergoes characteristic changes compared to other design fires, due to many factors such as growth stage, duration of the outbreak, and the peak temperature of the outbreak as shown in Figure 2-3

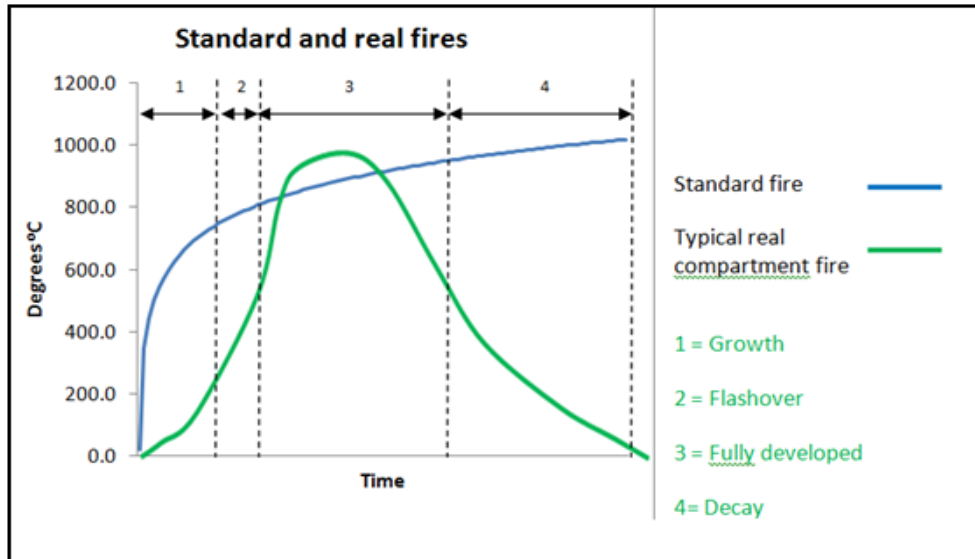


Figure 2-3: Comparison between parametric fire and real fire

According to the Steel Construction Institute [21], there are some similarities between parametric fires and real fires due to similar stages such as the flashover stage, cooling stage, and fire growth stage, as shown in Figure 2-4.

One drawback associated with the application of fire curves that represent compartments in gas temperature evolution is the inability to simulate the nature of fire propagation from one compartment to another since only synchronous compartments can be assumed in a fire Bailey et al. [22] provided a procedure for calculating the spread of a compartment fire within the natural range of fire curves. This procedure consists of assuming an initial scenario for the compartments, and after the temperature in these compartments reaches a peak, a curve of fire is applied to the adjacent compartments. When flashing is unlikely, i.e., simultaneous ignition of all fire loads in the compartment, the action of the fire shall be similar to the spot fire model [20].

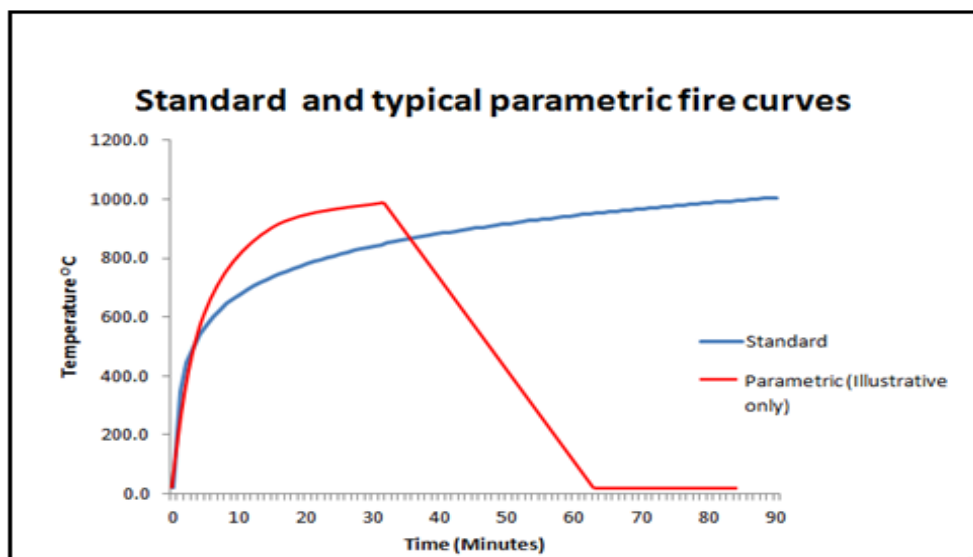


Figure 2-4: The comparison between ISO standard fire and Parametric fire

2.2 Load-carrying mechanism and limit state of beams

When evaluating the performance of steel beams in the event of a fire, the evaluation is often based on the bending behaviour of the beam at elevated temperatures. Therefore, the effect of axial end constraints on the beam is usually not taken into account. The end rotation can reduce the deflection of the beam in order to increase the bending strength of the beam in the event of fire [23]. However, the bending behaviour of the beam is associated with small deflections, and the behaviour of the beam with large deflections is very different. An important characteristic of beam operation under large deflections is that axial end constraints are not negligible. These axial end constraints can avoid the beam running away by behaving in catenary action that becomes the beam's primary load-bearing mechanism [24].

When the steel beam is reliably constrained in the axial direction, catenary action occurs, and the beam survival rate is improved at elevated temperatures. The temperature distribution, rotational constraints, or whether the beam experiences lateral-torsional buckling or not, have an insignificant effect on the beam behaviour. The axial level of constraint is the key factor that affects the deflection and catenary force of the beam. The higher the axial constraint, the less the beam deflects in catenary action. This helps with the integrity of the fire compartment where the constrained beam is located. However, the higher the axial constraint stiffness, the greater the catenary force applied to the structure adjacent to the beam is. Also, beam constraints arise from adjacent structures, so the higher the axial constraint, the more rigid the structure adjacent to the beam needs to be. Therefore, to take advantage of the catenary effect in a realistic application, the structure adjacent to the beam, including the connection, must be carefully considered. Their design is a compromise between the requirement to provide constraining stiffness, resistance to the catenary force of the beam, and the allowable deflection of the beam. If the large deflection of the beam is not a design restriction and if the adjacent structure is sufficiently resistant to the catenary force of the beam, it should be as flexible as possible to reduce the catenary force of the beam in the fire as shown in Figure 2-5 [25] [26].

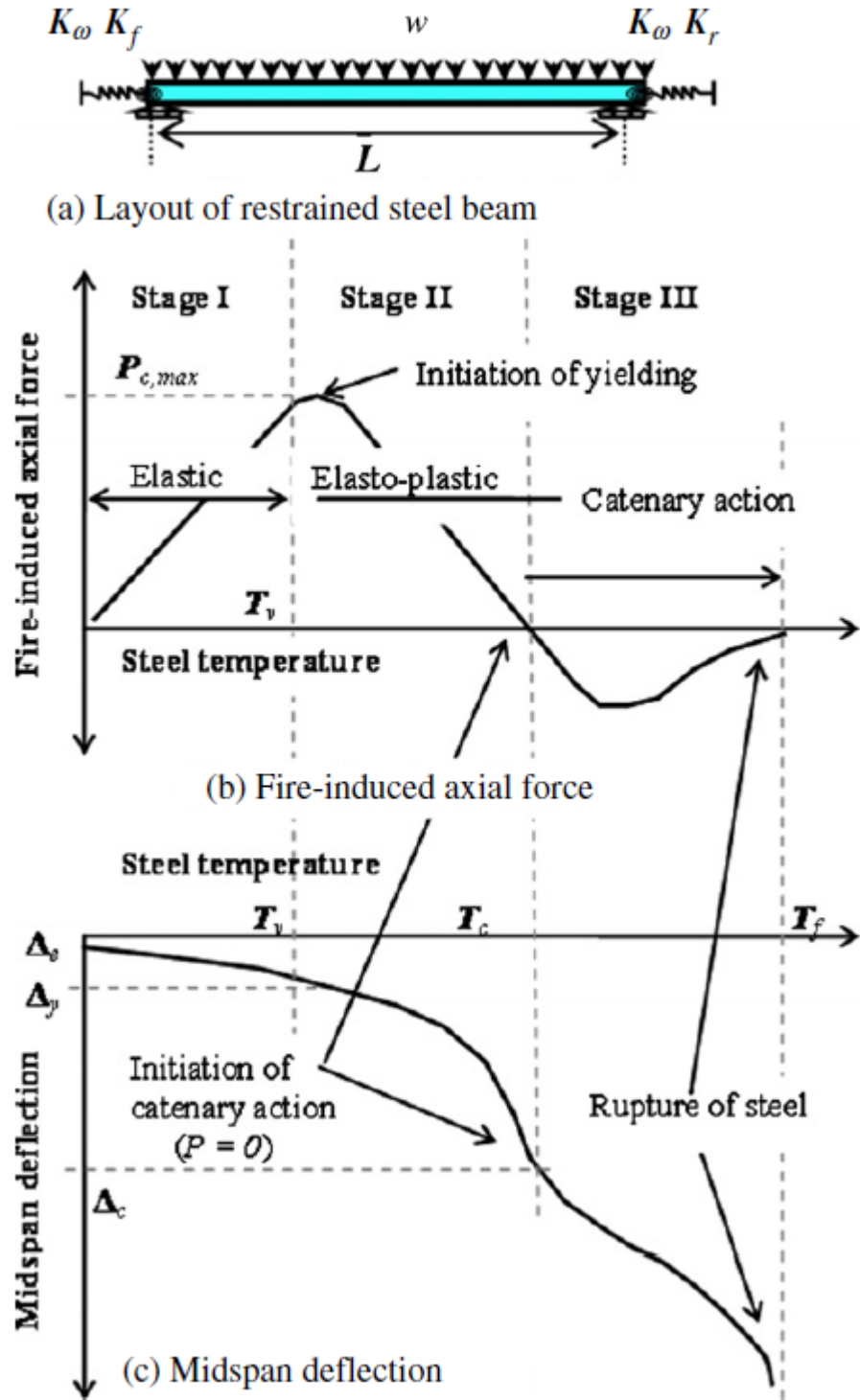


Figure 2-5: Typical fire response of a restrained steel beam that fails by yielding [25].

2.3 Design guidelines

Structural fire design is a design process for determining the performance of structures subjected to fire. This design process can be obtained mainly using three methods; Modelling of fire behaviour on the structure, calculation of the thermal response of the structure when exposed to fire and calculation of the structural response of the structure exposed to fire with mechanical loading. The primary goals of fire-resistant structural design are to ensure the safety of life for all occupants within the building, firefighters, and people around the building. It must be ensured that the occupants of the building have sufficient time to escape from the building during a fire. Structural fire design codes such as the Eurocode will be conducted during the building design phase. To meet these safety requirements and legislative approval of the building design, either prescriptive based design method or performance-based design method is used in the design codes. The prescriptive-based design method is a simple design method based on the rules described in the design codes, while the performance-based method is an advanced method based on the real behaviour of fire. These behaviours must be approximated using numerical simulation [27].

Figure 2-6 shows the three methods of structural fire design. The arrow and the number in Figure 2-6 indicate the complexity of the modelling, meaning that the number four is the most difficult procedure. In this thesis, the fire model has been taken from the fire test and the ISO standard fire curve. Advanced heat transfer and structural analysis of the member or frame are performed using FEM in thermal and structural analyses. This is the most complex method for modelling the thermal and structural response.

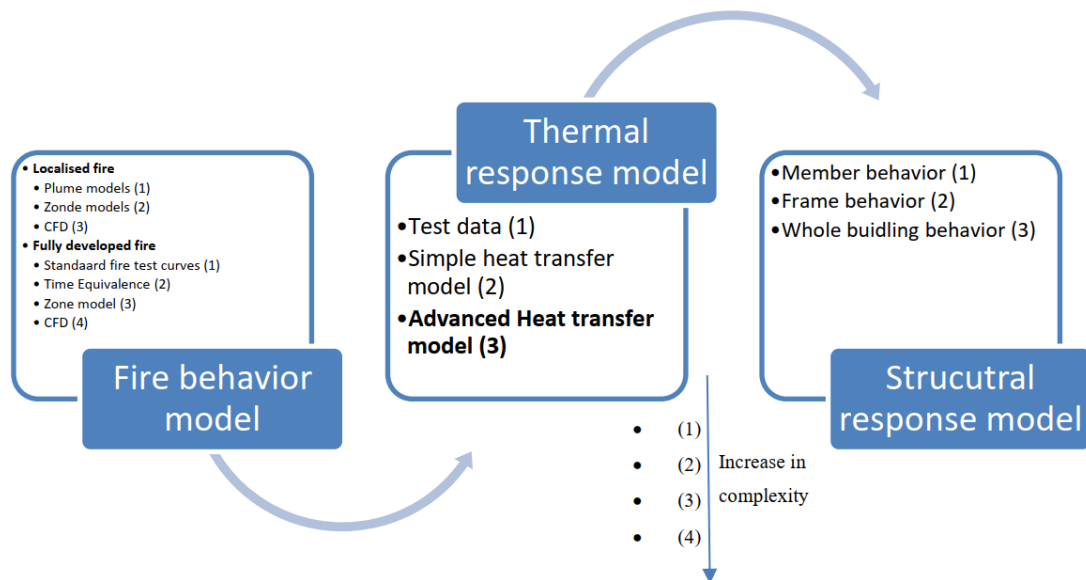


Figure 2-6: Structural fire design approaches [27]

2.3.1 Fire model

The first stage in the structural design for a fire is to estimate the realistic temperature for the gas above the structural part during the fire. The time-temperature curve is used as an input to the thermal response model. There are two types of fires, pre-flashover, and post-flashover fires [9]. For structural fire design, the post-flashover temperature is usually considered and can be obtained by localized fire and fully developed fire [27]. The realistic gas temperature of fire can be obtained from standard fire test, natural fire model, area model and computational fluid dynamic (CFD) model. The most accurate fire behaviour model is obtained using CFD fire models. As explained in section 2.1.1, Eurocode presents three time-temperature curves. The most commonly used is the standard temperature-time curve, also called the ISO curve.

2.3.2 Thermal response model

The second stage in the structural design of fire resistance is to predict the temperature distribution in the structural elements during a fire. This can be performed by analysing heat transfer between fire and structural members and inside structural members. The temperature distribution in members depends on the heat transfer by conduction, convection, and radiation of heat transfer on the member. If structures have complex geometry, nonlinear boundary conditions, thermal contact, cavity radiation, and temperature-dependent material properties; Solving the Fourier equation is nonlinear and must be done using numerical methods. There are three approaches to modelling the thermal response of a structure [27]; Test data, simple heat transfer models and advanced heat transfer models. In this thesis, the advanced model of heat transfer has been implemented. The advanced heat transfer model requires the use of the finite element method or the finite difference method. Temperature-dependent materials such as thermal conductivity, specific heat, and density are modelled in this approach.

2.3.3 Structural response model

The final stage in fire structural design is to anticipate the structural response of a structural member during a fire. The studied structure can be modelled as a single member or frame, or an entire building, as described in Figure 2-6. The structural analysis procedure for fire is a highly nonlinear analysis procedure due to the high temperature-dependent nonlinear materials, potential connectivity, and collapse behaviour. The structural analysis simulates the response of a structure to mechanical loading and fire. The main objective of structural analysis is to find the displacement and stress distributions under static or dynamic loading and boundary conditions. Structural analysis can be both static and dynamic. In fire design, structure analysis predicts the time that a structure can withstand mechanical loading until it collapses. Due to the dynamic nature and nonlinearity of the fire temperature curve, a nonlinear structural analysis should be considered for the fire analysis of structural.

2.4 Previous research on structural fire resistance of elements and connection

- Previous research by Erica C. Fischer and Amit H. Varma (2015) [28], which focused on the benchmarking of 3D element models to predict the behaviour of composite beams with simple shear connections in a fire condition, has shown that the detailed models reasonably predict the experimental deformation histories and observed failure modes. They have provided additional insight into axial forces developed in the connections, particularly during the cooling phase thence promoting the experimental findings.
- Research by Kristi L. Selden; Erica C. Fischer; and Amit H. Varma [29], which focused on the experimental investigations of the thermal and structural behaviour of composite beams with shear connections subjected to fire where vertical loading was applied to the composite beams with variations in the loading and heating protocol provided insight into the mechanical response and failure modes of composite beams and connections.
- Research by Erica C. Fischer; Kristi L. Selden; and Amit H. Varma [30], which provides more data about the test under consideration. They examined different types of simple connections that are most commonly used in buildings. The specimens were subjected to controlled heating and cooling curves.
- Report by B. Zhao, and J. Kruppa [31], which studied shear connectors with different slab types to derive force-slipping relationships versus elevated temperature. They investigated the fire behaviour of composite beams with simply and continuous supports.

3. FINITE ELEMENT MODELLING OF STEEL BEAM EXPOSED TO NOMINAL FIRE

This chapter contains the finite element model of a simple steel beam exposed to nominal fire. Including the studied structure, and thermal and mechanical material properties of steel that has been used in thermal and structural analyses. Validation of the model and the results with the theoretical prediction equation from Eurocode. Defining beam load-carrying mechanism during different stages of the fire.

3.1 Studied steel beam

A simply supported beam (IPE 200) exposed to standard fire was used to verify the FE models. This model was generated to get a better understanding of the simple steel beam behaviour under loading and heating phases.

The pressure load was applied to the beam on the top face of the upper flange. The load was equivalent to the uniformly distributed load of 10 kN/m and 19.6 kN/m. These two load cases were considered to represent the 0.25 and 0.5 load ratio of the beam. The length of the I-beam was 4 m, as shown in Figure 3-1(a). The dimension of the I-beam cross-section is given in Figure 3-1(b).

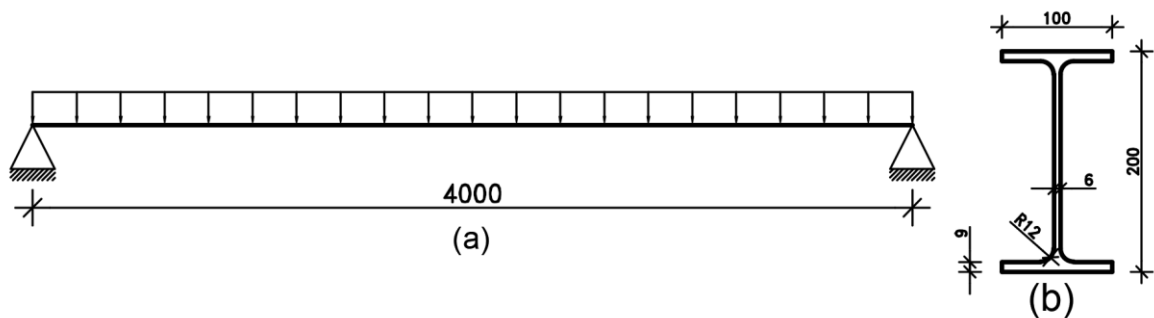


Figure 3-1: Simply supported beam with a profile of IPE 200 (a) beam layout [mm] (b) dimension of the cross-section [mm].

When exposed to fire, the simply supported beam was heated with elevated gas temperature. All sides of the beam were exposed to fire, except the upper surface of the top flange was exposed to air. The air temperature was considered room temperature. . The fire is modelled using standard fire by Equation 1

$$\theta = \theta_0 + 345 \cdot \log_{10}(8t + 1)$$

Equation 1

Where $\theta_0 = 20$, t is time in min. Thus produced gas temperature is shown as shown in Figure 3-2

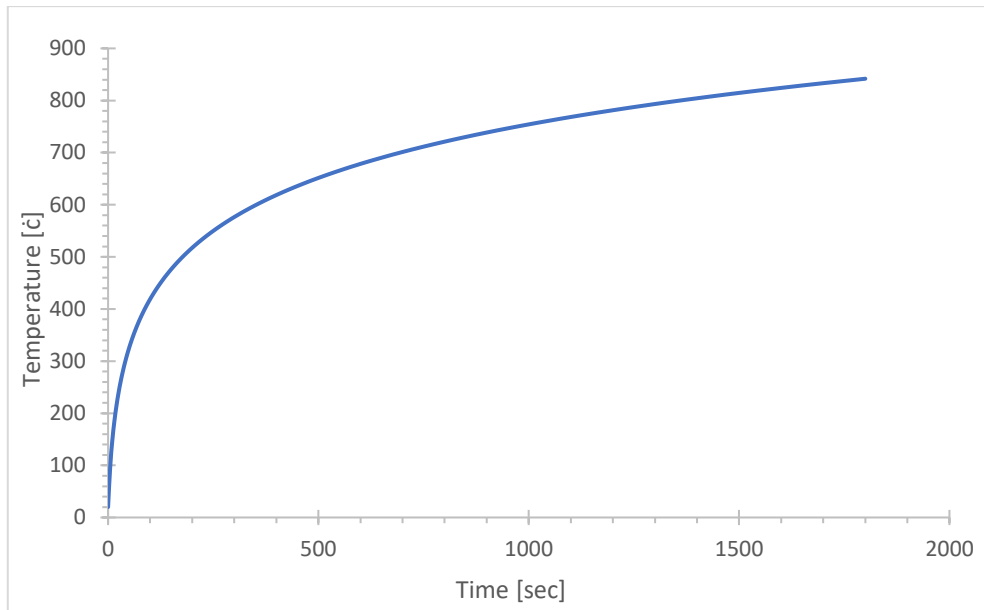


Figure 3-2: Standard fire curve [18].

3.2 Thermal analysis model

The target of thermal analysis was to predict the temperature distribution in the beam cross-section. The details of the FE model for the thermal analysis are explained in this section.

3.2.1 FE meshes and boundary conditions

3.2.1.1 Mesh and element properties

An 8 node-linear heat transfer brick element was used to mesh the I-beam cross-section three-dimensionally. The cross-sectional view of the model is shown in Figure 3-3. The 3D thermal model mesh consists of 13668 nodes and 9576 elements (DC3D8 – 8 nodes linear heat transfer brick) with an approximate global mesh size of 30 mm. Uniform meshes across the geometry were created. The model used four layers of finite elements through the thickness of the web and two layers of finite elements through the flange.

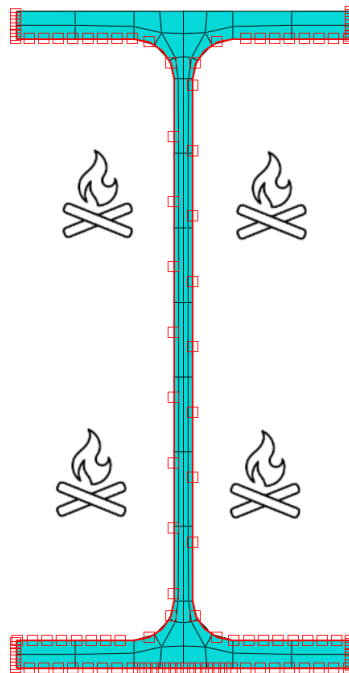


Figure 3-3: Cross-section of FE model with heating boundary conditions for IPE200 FE model with heating sides

3.2.1.2 Interactions

Boundary convective and radiative heat transfer were defined with elevating gas temperature using the interactive module of FILM and RADIATE procedures in Abaqus/CAE [32]. The convection coefficient factor for gas temperature on the fire exposed side was taken as $25 \text{ W/m}^2\text{K}$ and as $9 \text{ W/m}^2\text{K}$ on the unexposed side, according to EN 1991-1-2 [2002]. The emissivity factor was defined as 0.7 for radiation, according to EN 1992-1-2 [2005]. The reference temperature for the unexposed surface was defined as 20°C .

3.2.1.3 Predefined fields

The initial temperature of 20°C was defined using a predefined temperature field.

3.2.1.4 Model setup and analyses

A transient heat transfer analysis was performed using Abaqus/Standard procedure HEAT TRANSFER with an automatic time step size of 1800 sec (30min). Absolute zero temperature was defined as -273.16°C and the Stefan-Boltzmann constant as $5.67\text{e-}8 \text{ W}\cdot\text{m}^{-2}\cdot\text{K}^{-4}$. International System of Units (SI) was used for all models.

3.2.2 Thermal material properties of steel

The density, temperature-dependent thermal conductivity, and specific heat of steel material were defined according to EN 1993-1-2 [2005]

3.2.2.1 Steel thermal conductivity λ

Thermal conductivity is a measure of how quickly a particular material conducts heat. The thermal conductivity of steel is a function of both the temperature and the composition of the steel. The Eurocode EN 1993-1-2 [2005] proposes the following linear approximation for the thermal conductivity of structural steel, as shown in Figure 3-4 based on Equation 2 - 3.

$$\lambda = 54 - 3.33 \cdot 10^{-2} \cdot \theta \quad 20^{\circ}\text{C} \leq \theta < 800^{\circ}\text{C}$$

Equation 2

$$\lambda = 27.3 \quad 800^{\circ}\text{C} \leq \theta < 1200^{\circ}\text{C}$$

Equation 3

Where λ is thermal conductivity (W/mK),
 θ is the steel temperature.

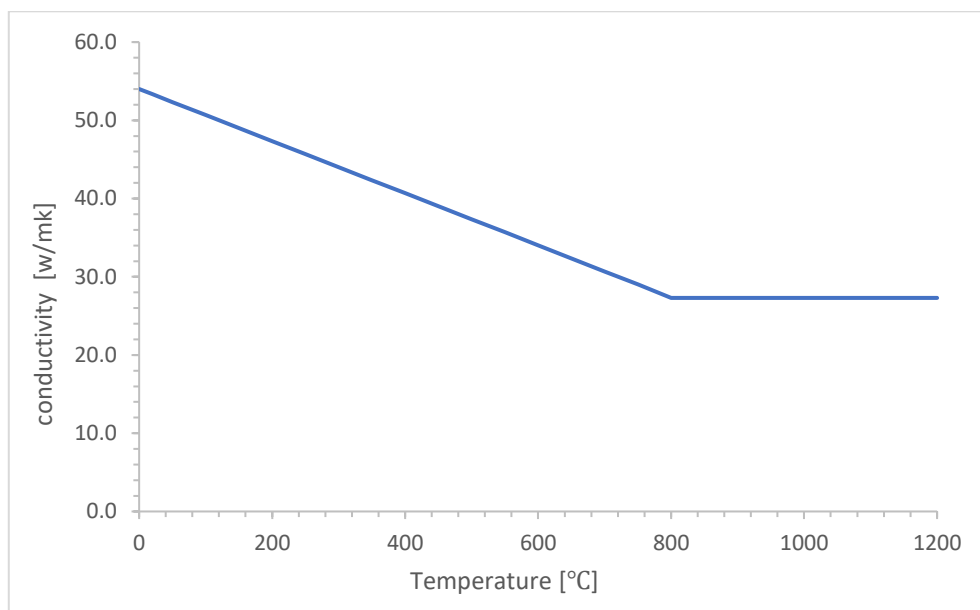


Figure 3-4: Thermal conductivity of steel as a function of temperature [33]

3.2.2.2 Steel specific heat C_a

Specific heat is a measure of a substance's ability to absorb heat. For steel, specific heat is a function of temperature and is independent of the composition of the steel. The Eurocode EN 1993-1-2 [2005] suggests the following approximation for the specific heat of structural steel, as shown in Figure 3-5 based on Equation 4 - 7.

$$C_a = 425 + 7.73 \cdot 10^{-1} \cdot \theta - 1.69 \cdot 10^{-3} \cdot \theta^2 + 2.22 \cdot 10^{-6} \cdot \theta^3 \quad 20^\circ\text{C} \leq \theta < 600^\circ\text{C} \quad \text{Equation 4}$$

$$C_a = 666 + \frac{13002}{738 - \theta} \quad 600^\circ\text{C} \leq \theta < 735^\circ\text{C} \quad \text{Equation 5}$$

$$C_a = 545 + \frac{17820}{\theta - 731} \quad 735^\circ\text{C} \leq \theta < 900^\circ\text{C} \quad \text{Equation 6}$$

$$C_a = 650 \quad 900^\circ\text{C} \leq \theta < 1200^\circ\text{C} \quad \text{Equation 7}$$

Where C_a is the specific heat, (J/kgK)
 θ is the steel temperature.

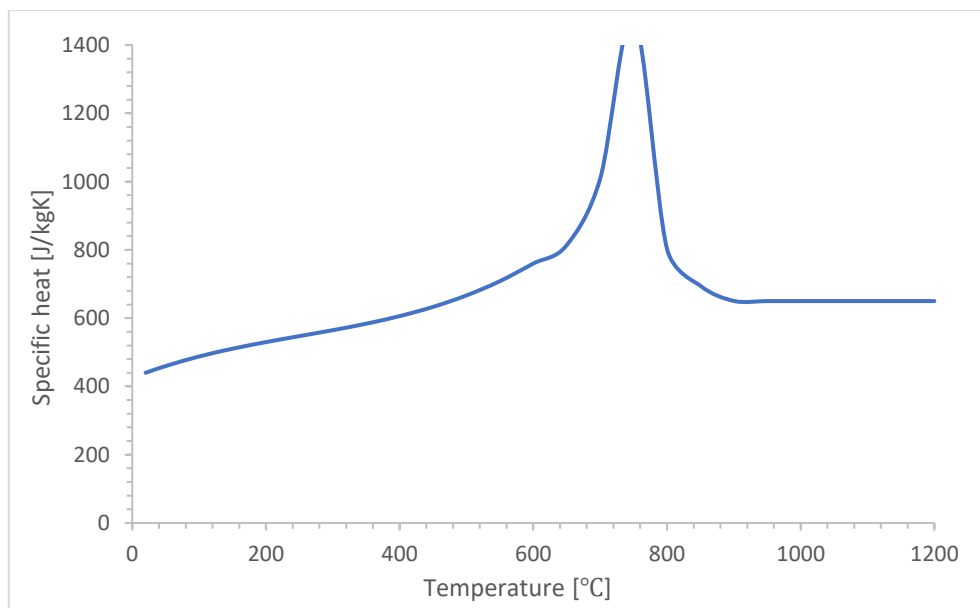


Figure 3-5: Specific heat of steel as a function of the temperature [33]

The sharp peak can be seen at 730°C in Figure 3-5 according to specific heat equations of steel suggested in EN1993-1-2 [2005]. The sharp peak is due to a metallurgical change in the steel crystal structure.

3.3 Structural analysis model

The FE models using a 3D solid element for structural analyses were created to simulate the steel beam with different load ratios. The modelling details are explained below.

3.3.1 FE meshes and boundary conditions

3.3.1.1 Geometry

The studied I-beam was modelled as a solid element as shown in Figure 3-6. The dimensions of the cross-section were defined in Figure 3-1.

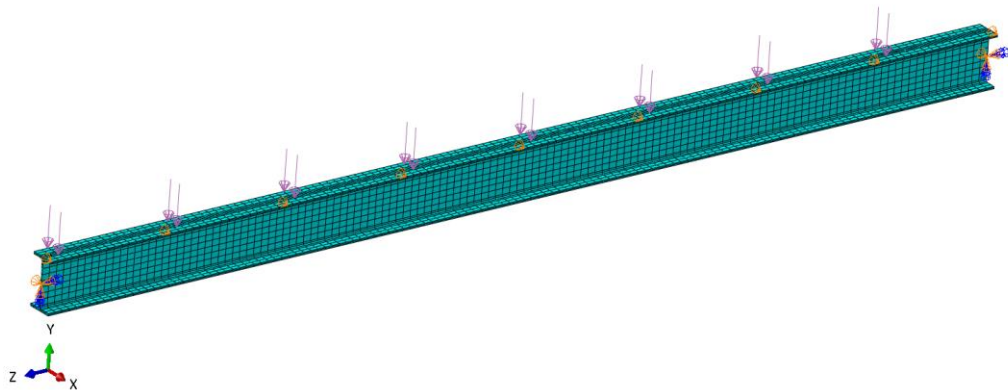


Figure 3-6: FE model of I-beam

3.3.1.2 Mesh and element properties

The beam was modelled using C3D8R (An 8-node linear brick, reduced integration, hourglass control) beam element from an explicit Abaqus element library [32]. The mesh consists of 13668 nodes and 9576 elements with an approximate global mesh size of 30 mm. Uniform mesh across the geometry was defined as similar to thermal model mesh.

3.3.1.3 Interaction, loads, and boundary conditions

The beam was loaded with pressure in the Y-direction as shown in Figure 3-6. The value of forces were 0.1 and 0.2 MPa which represented 0.25 and 0.5 of the load ratios of the beam respectively. Simply supported boundary conditions were defined for the end nodes of the beam. For a more realistic simulation, the top flange was restrained from moving out of the plan to simulate the restrained from a concrete slab. The mechanical loading was applied in two phases: the mechanical loading phase (phase 1) and the heating phase (phase 2). The load was increased linearly from zero to the maximum during 30 sec in the mechanical loading phase and kept constant through the fire heating phase for 1800 sec (30min). Figure 3-7 shows the loading curve for both phases.

3.3.1.4 Predefined fields

Room temperature and temperature histories due to fire from the thermal model were applied as predefined nodal temperatures to the beam cross-section.

As shown in Figure 3-8, the room temperature was used during the mechanical loading phase 1. After that, the fire node temperature phase was applied during fire phase 2.

3.3.1.5 Model setup and analyses

The structural analysis was performed using Abaqus/Explicit dynamics procedure. The total simulation mass was scaled to decrease the actual simulation time. Mass scaling is often used in ABAQUS/Explicit for computational efficiency in quasi-static analyses and in dynamic analyses that contain a few very small elements that control the stable time increment during loading and heating phases [32]. Mass scaling was defined to be 5000 using a scale factor. The explicit solution was performed using two phases and as shown in Figure 3-7. In the first phase about 30 sec as problem time, the mechanical load was applied, and in the second phase for about 1800 sec (30min), the heating due to fire was applied. The total time for simulation is 1830 sec (30.5min).

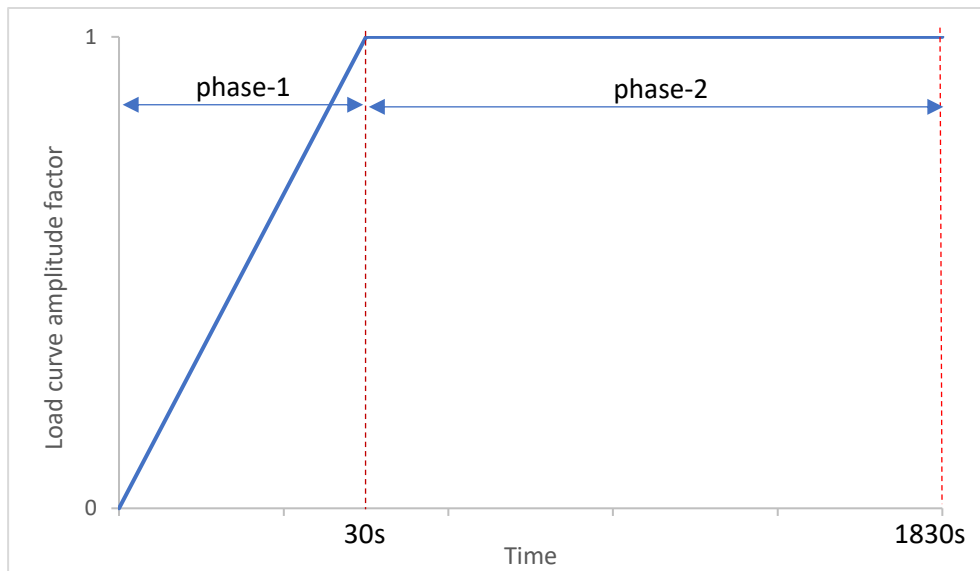


Figure 3-7: Load curve for applying mechanical loading

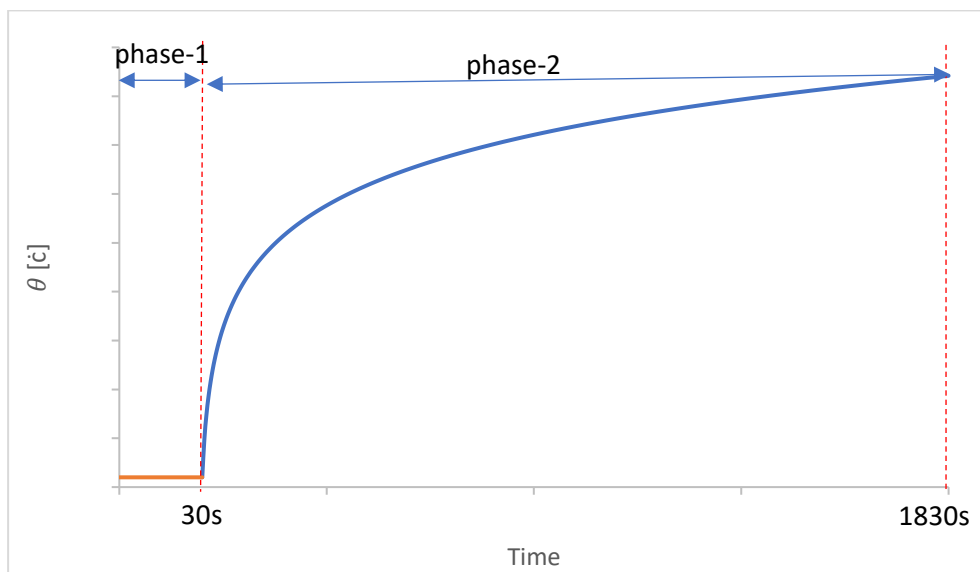


Figure 3-8: Curve for applying temperature loading due to fire

3.3.2 Mechanical material properties of steel S355

Mechanical material properties density, temperature-dependent isotropic elasticity, temperature-dependent coefficient of thermal expansion and temperature-dependent plasticity were defined according to EN1993-1-2 [2005].

3.3.2.1 Steel S355 material properties at 20°C

The following ambient material properties have been used for steel S355.

Table 3-1: Properties of steel S355 at the ambient temperature of 20°C

Property	Notation	Value
Yield strength [MPa]	f_y	355
Poisson's ratio	n	0.3
Elastic modulus [GPa]	E	210
Density [kg/m ³]	ρ	7850

3.3.2.2 Steel S355 material properties at elevated temperatures

The strength and stiffness of steel decrease with increasing temperature. The dependence of these properties on temperature was defined using the reduction factors taken from the EN1993-1-2 [2005]. The reduction factors as shown in Figure 3-9 were used to define the elastic modulus and yield strength. These two properties are shown in Figure 3-10 and Figure 3-11 respectively.

The symbols used in Figure 3-10 are defined as follows:

- $k_{E,\theta}$ is the ratio of the elastic modulus at elevated temperature to the elastic modulus at 20°C.
- $k_{y,\theta}$ is the ratio of the yield strength at elevated temperature to the yield strength at 20°C.
- $k_{p,\theta}$ is the ratio of the proportional limit at elevated temperature to the proportional limit at 20°C.

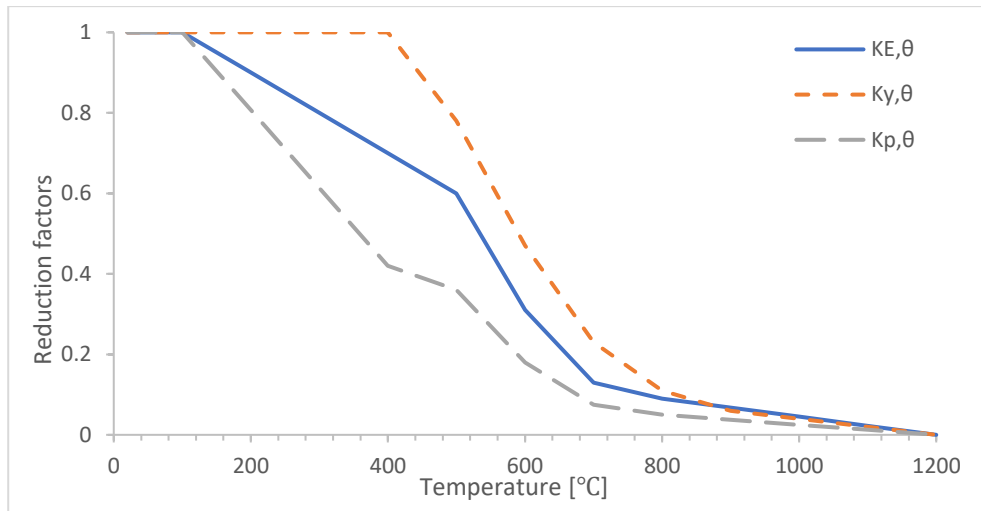


Figure 3-9: Reduction factors of the steel S355 stress-strain relationship at elevated temperatures [33]

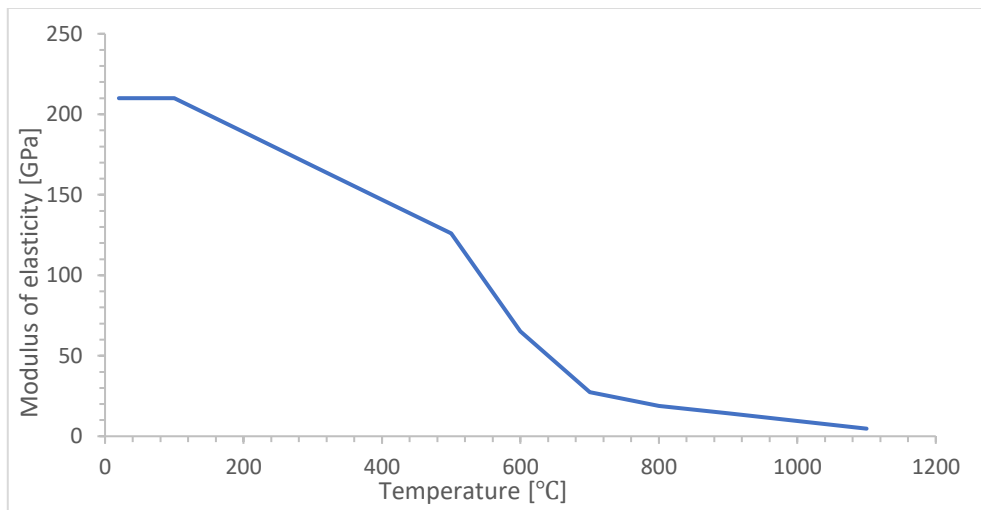


Figure 3-10: Modulus of elasticity for steel S355 as a function of temperature [33]

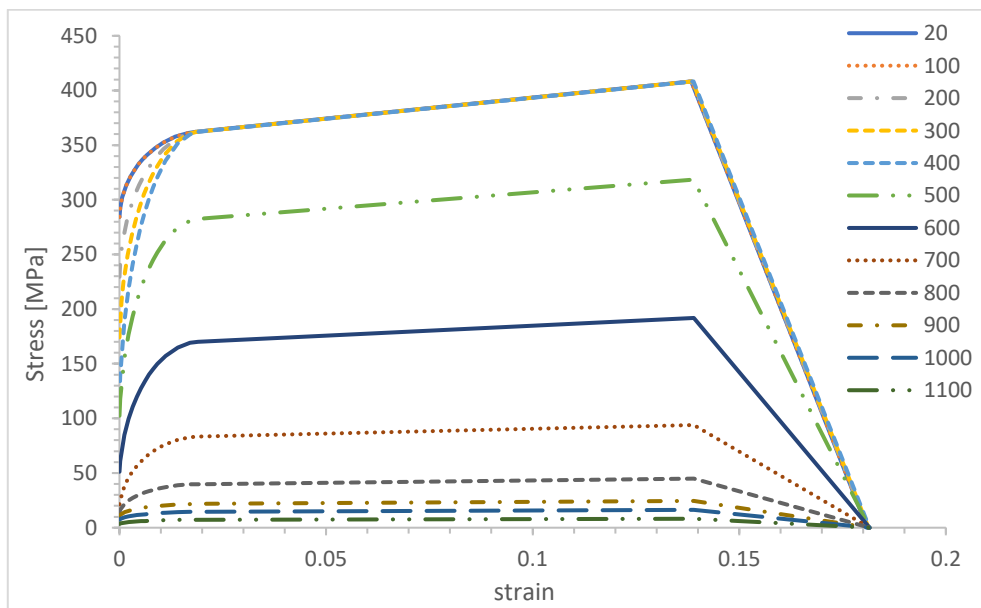


Figure 3-11: stress-strain curves for S355 at different temperatures [33]

3.3.2.3 Steel thermal elongation

The thermal elongation of steel was defined as the increase in the length of the member divided by its initial length, $\Delta L/L$. EN1993.1.2 [2005] proposes the following stepwise approximation for the thermal elongation of most structural steels based on Equation 8 – 10.

$$\Delta l/l = 1.2 \cdot 10^{-5} \cdot \theta + 0.4 \cdot 10^{-8} \cdot \theta^2 - 2.416 \cdot 10^{-4} \rightarrow 20^\circ\text{C} \leq \theta < 750^\circ\text{C}$$

Equation 8

$$\Delta l/l = 1.1 \cdot 10^{-2} \rightarrow 750^\circ\text{C} \leq \theta < 860^\circ\text{C}$$

Equation 9

$$\Delta l/l = -6.2 \cdot 10^{-3} + 2 \cdot 10^{-5} \cdot \theta \rightarrow 850^\circ\text{C} \leq \theta < 1200^\circ\text{C}$$

Equation 10

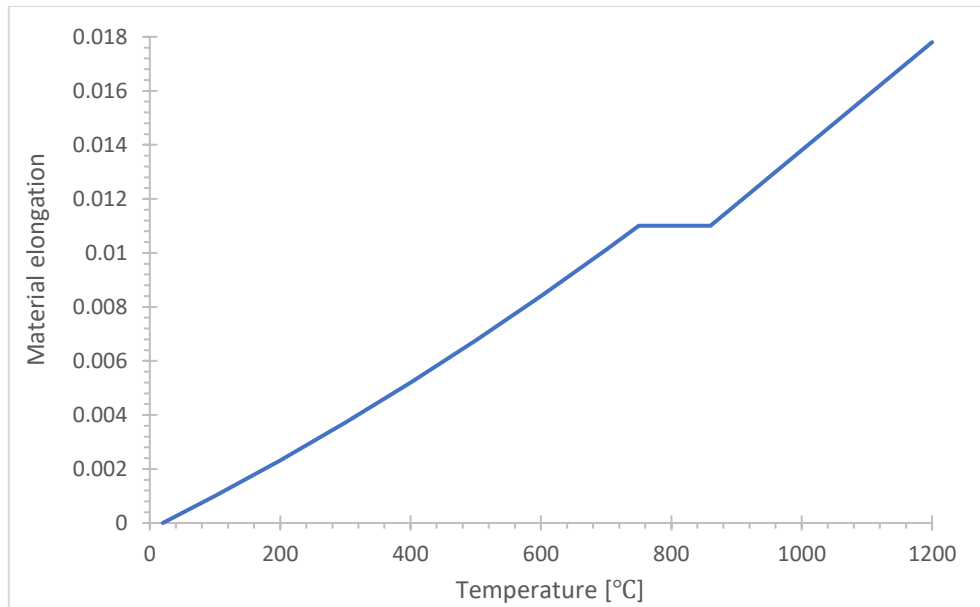


Figure 3-12: Relative thermal elongation of steel as a function of the temperature [33]

As required by ABAQUS, the thermal elongation factor is transferred to thermal expansion coefficients, α , which define the total thermal expansion from a reference temperature. The thermal expansion coefficient is defined as

$$\alpha = ((\Delta l/l)/(\theta - 20))$$

Equation 11

Where $\Delta l/l$ is the thermal elongation,
 θ is the steel temperature,
 α is the thermal expansion coefficient used in ABAQUS.

3.4 Verification of FE models

3.4.1 verification of thermal analysis model

The developed finite element model was verified by comparing the thermal responses from the model with those calculated by the EN1993-1-2 [2005]. The verification process included nodal temperature histories. Figure 3-13 to Figure 3-15 show a comparison between FE temperatures and calculated temperatures in the steel beam as a function of fire exposure time.

The FE temperatures tend to differ slightly from the values received manually; such variation can be attributed to differences in definition and solvers used in ABAQUS. The average temperature of the bottom flange and web were extracted from ABAQUS and compared with the fully exposed beam as shown in Figure 3-13 and Figure 3-14. The maximum temperature at the end was at the web 834°C and the bottom flange was 830°C while the top flange was 785°C. The values of the manual calculation for the beam with the three sides exposed were close to the top flange temperature as the values give the average temperature for the whole cross-section. The manually calculated values for the beam fully exposed matched the temperature curves of the bottom flange and the web as they are the most critical sections since the fire affected both of their sides. The results from FE thermal model show good agreement with calculated results, which confirm that a similar approach can be used for simulating thermal response in fire engineering. The results obtained from the beam FE thermal analysis were shown in Figure 3-16 in which the sectional distribution at different times demonstrates the temperature development during the fire.

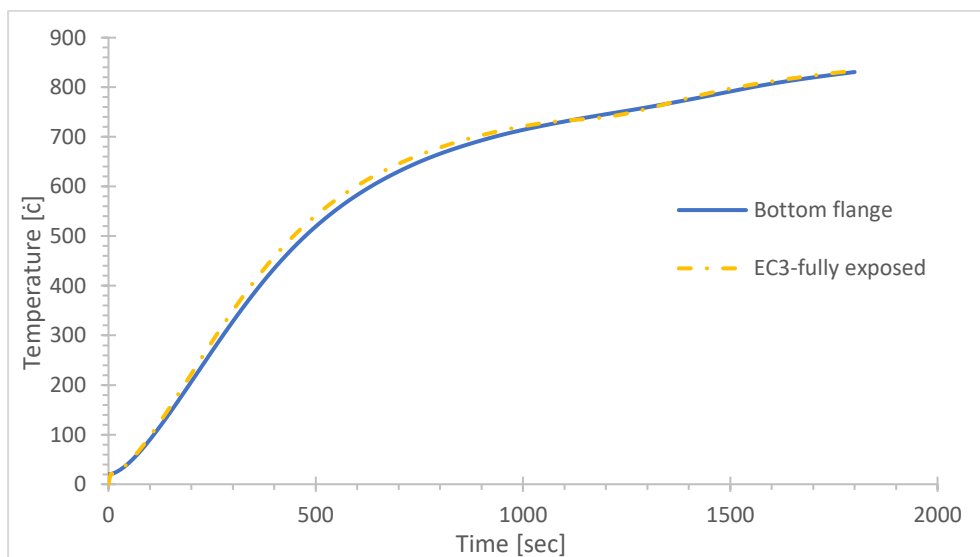


Figure 3-13: Comparison of temperature history for bottom flange

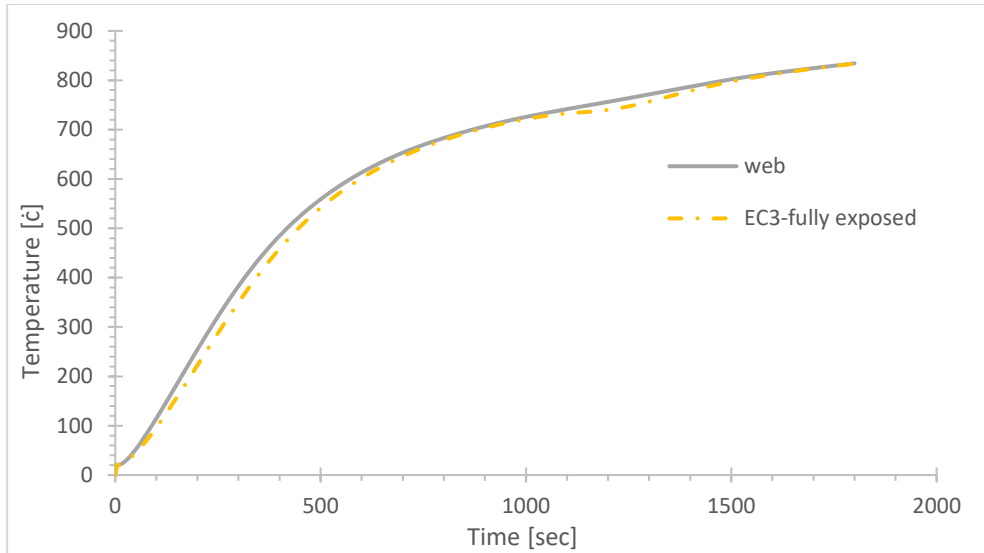


Figure 3-14: Comparison of temperature history for web

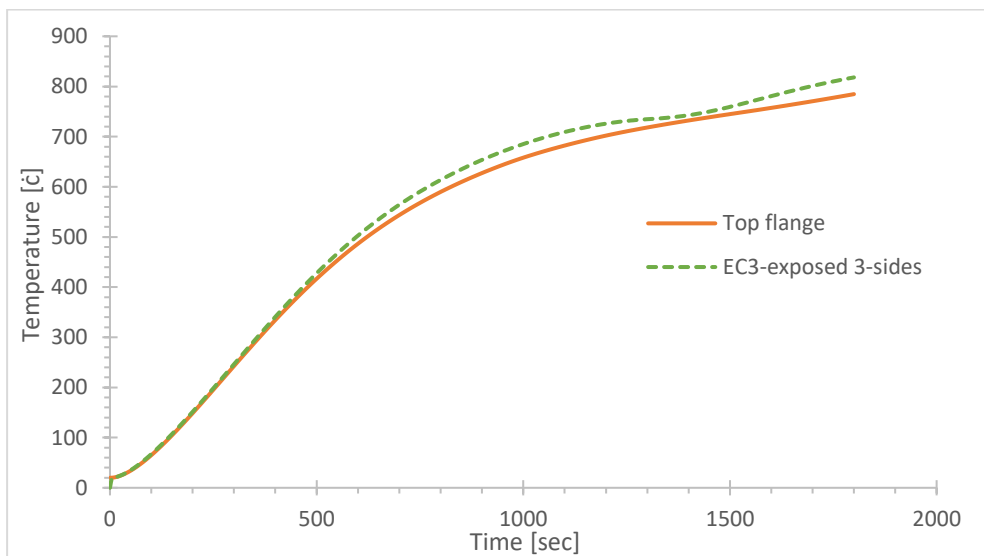


Figure 3-15: Comparison of temperature history for top flange

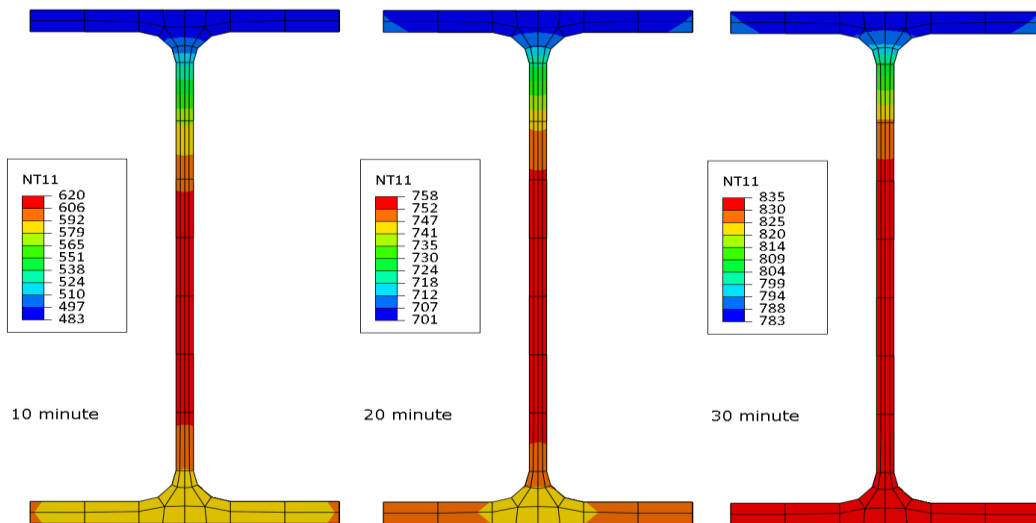


Figure 3-16: Temperature distribution of the beam cross-section

3.4.2 Verification of the model for mechanical analysis

The mid-span of the steel beam received by the FEM was compared to the values calculated manually according to EN1993-1-2 [2005]. The FE model gave displacements of 8 and 16 mm for the mechanical load phases with ratios of 0.25 and 0.5 respectively. These results were the same as received by the hand calculations as shown in Figure 3-17 and Figure 3-18.

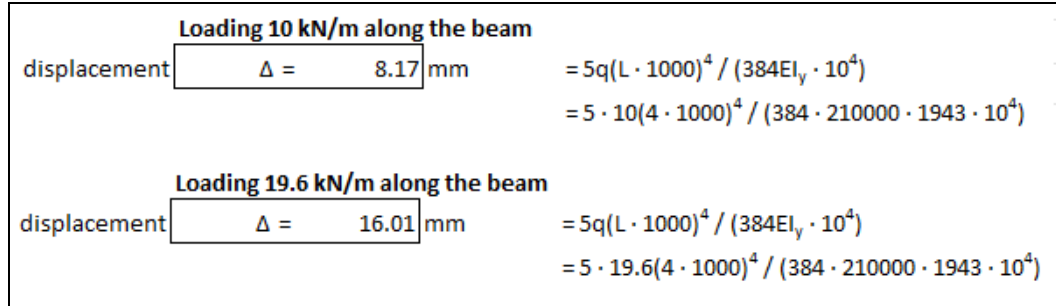


Figure 3-17: Deflection manually calculation

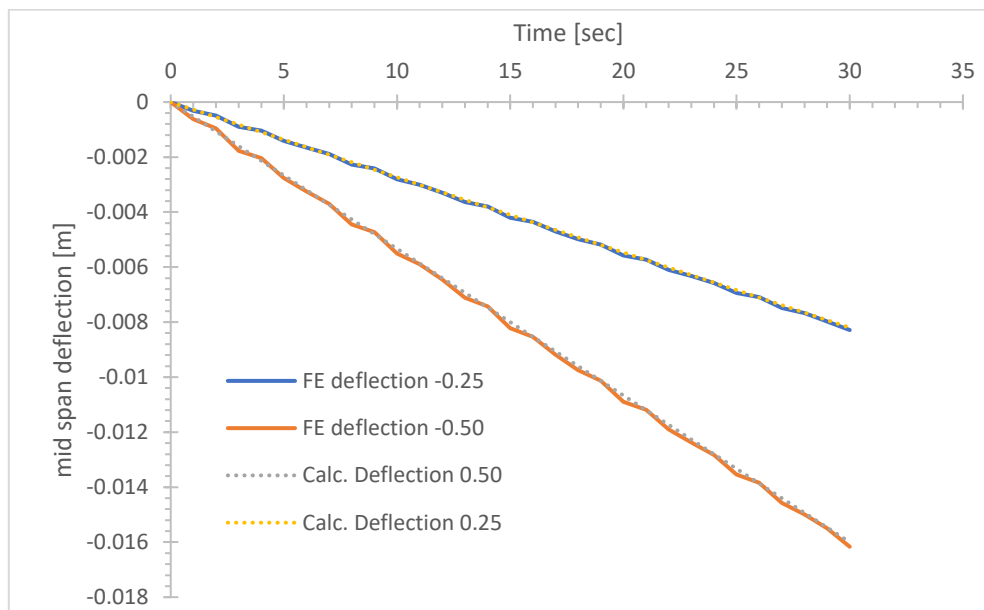


Figure 3-18: Displacement calculated by the FEM and manually

The manually calculated critical temperature based on EN1993-1-2 [2005] was compared to the critical temperature received from the FE analysis. The critical temperature from the FE analyses is based on the amount of deflection measured during the test and the rate of deflection calculated from these measurements which are given in CEN [2012] EN1363-1. The limited deflection amount is expressed by Equation 12 [34].

$$D = \frac{L^2}{400 \cdot d}$$

Equation 12

Where D is the limiting deflection [mm],

L is the clear span [mm],

d is the distance between the compression zone and tension zone [mm].

Figure 3-19 shows the manual calculation for critical temperature which was 526°C. From Equation 12, the limited deflection was 200 mm. FE results showed that the deflection of 200 mm occurred at 11 minutes for the 0.25 ratio case and 8 minutes for the 0.5 ratio case. The temperature at the beam cross-section for both load cases when the deflection reached the limited deflection is shown in Table 3-2. The average temperatures were fairly close to the manual calculation of critical temperature $\pm 50^\circ\text{C}$. The ratio was 83-93% for the max temperature on the beam surface and 90-105% for the average temperature of the cross-section. Based on comparisons of deflections at room temperatures and the critical temperatures at elevated temperatures, the FE model for mechanical analysis is verified and will be used further for studying the behaviour of composite beams.

Section factor		
$A_m/V =$	234.5 m ⁻¹	$= (3b + 2[h - t_w - 4r] + 2\pi r) \cdot 10 / A$ $= (3 \cdot 100 + 2[200 - 5.6 - 4 \cdot 12] + 2\pi \cdot 12) \cdot 10 / 28.5$
$\eta_{fi} =$	1	No load reduction
$k_1 =$	0.7	adaptation factor for unprotected beam
$k_2 =$	1	adaptation factor for simply supported beam
$\mu_0 =$	0.7	
Critical temperature		
$\theta_{a,cr} =$	526 °C	$= 39.19 \ln([1 / \{0.9674 \mu_0^{3.833}\}] - 1) + 482$ $= 39.19 \ln([1 / \{0.9674 \cdot 0.7^{3.833}\}] - 1) + 482$
T =	8.5 min	from Nomogram curves for the simplified prediction of the fire resistance
Limited deflection		
D =	200 mm	$= L^2 / (400d)$ $= 4000^2 / (400 \cdot 200)$

Figure 3-19: Critical temperature manually calculation based on Normogram curves

Table 3-2: Temperature at 200 mm deflection

	Critical temperature at limited deflection criterion from FE model [°C]				Critical temperature by manually calculation	Temperature ratio	
	Bottom flange	Web	Top flange	Average		Max	Average
Load 0.25 ratio	600	630	506	579	526	83.5%	90.9%
Load 0.50 ratio	520	562	417	500	526	93.6%	105.2%

3.5 Load-bearing mechanism of steel beam

3.5.1 Four-stage mechanism

Figure 3-20 shows the stress development at the mid-span of the top and bottom flange of the beam firstly during mechanical loading for 30 sec followed by the period when the beam was exposed to fire for 30 minutes. During the temperature rise, the top flange stays cooler than the rest of the section causing a downward thermal bowing. The tension in the bottom flange and compression in the top flange increase linearly during the loading phase. As the temperature starts to rise through the cross-section, the compression stresses increase, and the tension reduces due to the restrained thermal expansion. Therefore, the compression stresses increase under axial compression forces along the beam. After that, the stresses at the flanges start to act normally as the deflection increase and allow the beam expansion. The mid-span moment decreases until the material yield which happens when the bottom flange temperature is around 450-600°C.

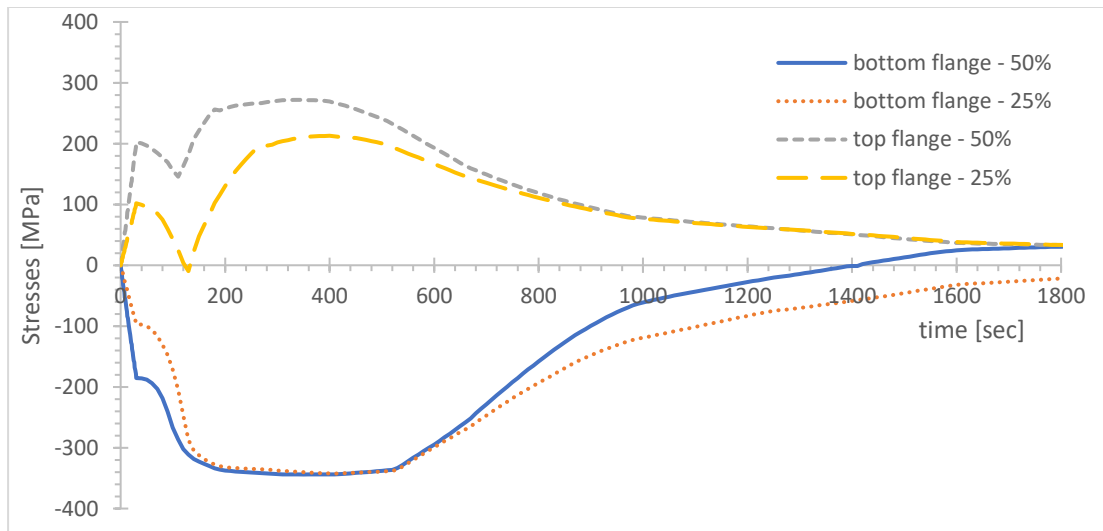


Figure 3-20: Max principal stresses at the mid-span of the beam as a function of time

Figure 3-21 represents the axial force at the support. The positive values present compressive axial forces and negative values represent tensile axial force. Figure 3-22 presents the variation in the deflection against time. The beam did not have a runaway failure at the heating; however, the deflection was large.

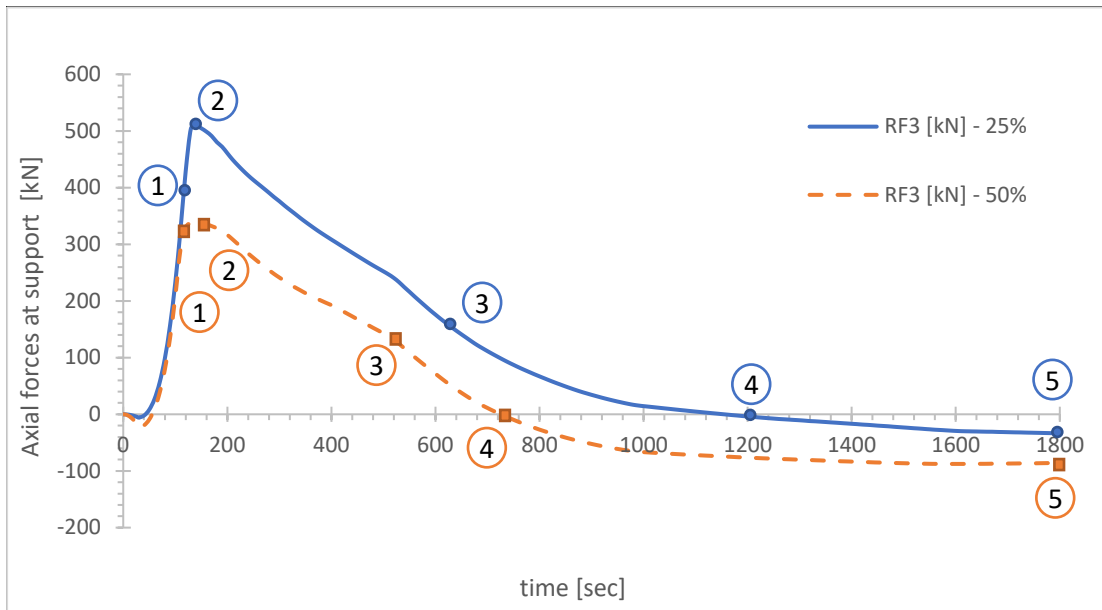


Figure 3-21: Axial reactions at the supports as a function of time

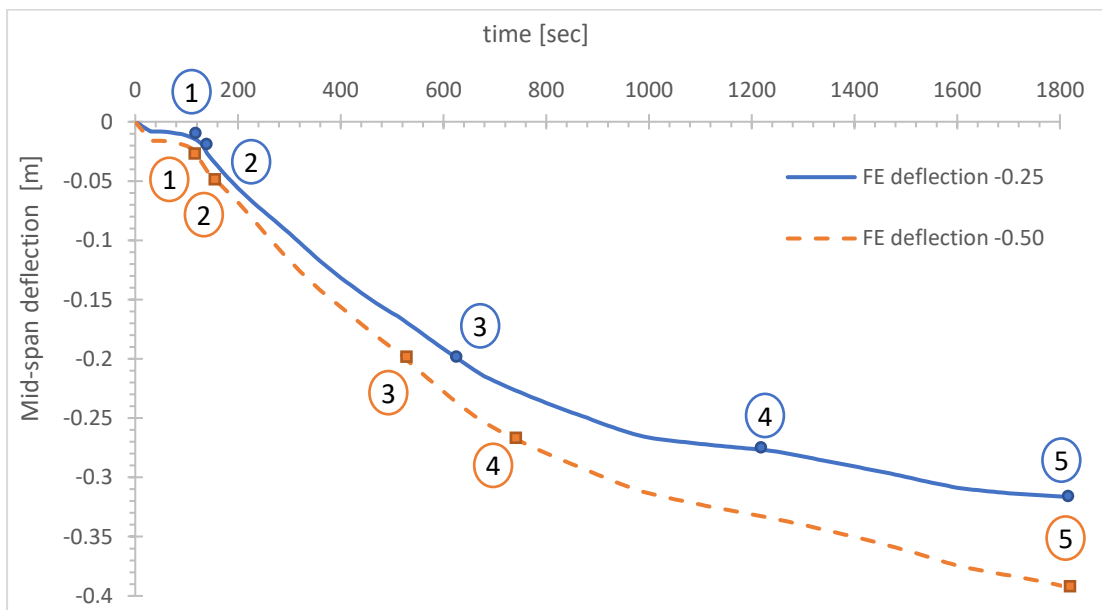


Figure 3-22: Mid-span deflection as a time function

Based on the axial force developed, the load-bearing mechanism of the composite beam is divided into 4 stages:

- Stage I (0-1): the beam deflected gradually while applying the loads till it reached the point (0) where the heating started. The stresses at point (0) are shown in Figure 3-23 and Figure 3-28. The maximum tension was 6 kN and 23 kN for the 0.25 and 0.5 load cases respectively. When the heating phase started, the vertical deflection increased slowly at the beginning when the beam tried to expand and was restrained due to boundary conditions. There was no significant change in the deflection that happened around 110 sec when the bottom flange temperature was about 100°C at point (1). The stresses at point (1) are shown in Figure 3-24 and Figure 3-29.

- Stage II (1-3): during this stage, the deflection increment increased due to material degradation. Point (2) was the maximum compressive axial force produced in the restrained beam due to thermal expansion. The axial compression forces reached 510 kN and 335 kN for the 2 cases. The degradation continue till the bottom flange temperature was about 500°C-600°C at point (3), where the yield strength of the steel started to decrease at around 500-700 sec.
- Stage III (3-4): While the beam continued losing its strength, the vertical deflection increases dramatically. During this stage, the axial force was in transition from compression to tension due to a large deflection. The beam was partially in tension. Point (4) presents the transition to tension completely which was at 730-1200 sec and the temperature was 650-740°C. The stresses at point (4) are shown in Figure 3-26 and Figure 3-31.
- Stage IV (4-5): the beam was completely in tension due to catenary action. The catenary action usually occurs at a large deflection and can effectively prevent beam deflections from further run-away. At the end of the fire step, the displacements were 317 and 394 mm. The stresses at point (5) are shown in Figure 3-27 and Figure 3-32.

Figure 3-23 to Figure 3-27 show the absolute max principle stresses with deflection along with the FE model with a 0.25 load ratio at different stages. Principal stress represents the normal stress acting onto the principal plane that has zero shear stress. Figure 3-28 to Figure 3-32 show the absolute max principle stresses with deflection along with the FE model with a 0.5 load ratio at different stages.

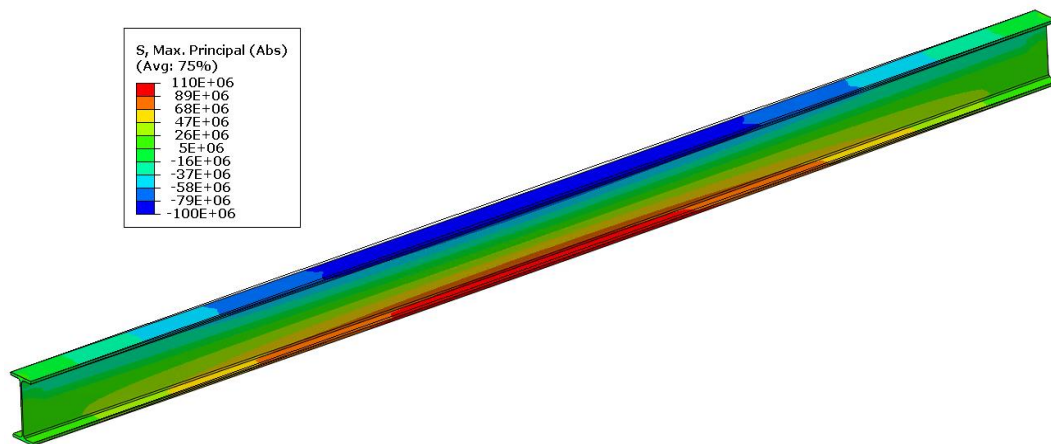


Figure 3-23: Beam stresses after loading step - 0.25 ratio

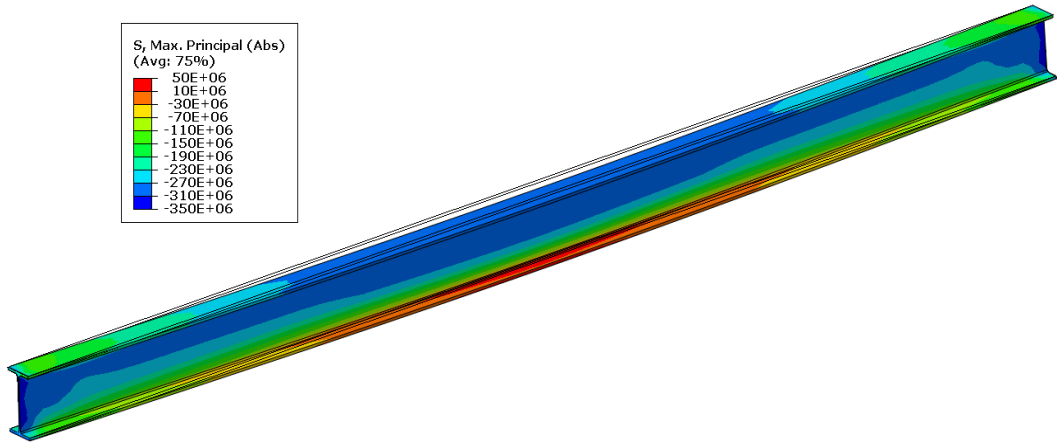


Figure 3-24: Beam stresses at 110 sec- 0.25 ratio

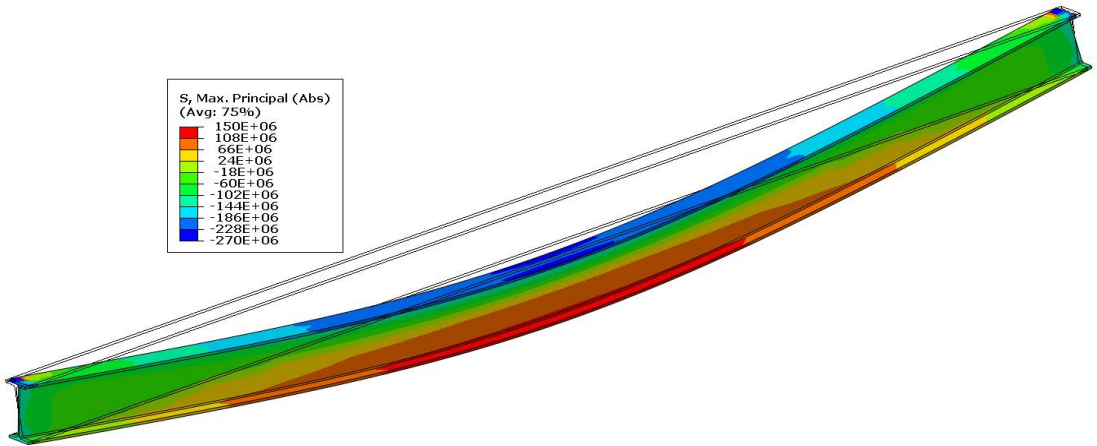


Figure 3-25: Beam stresses at 700 sec- 0.25 ratio

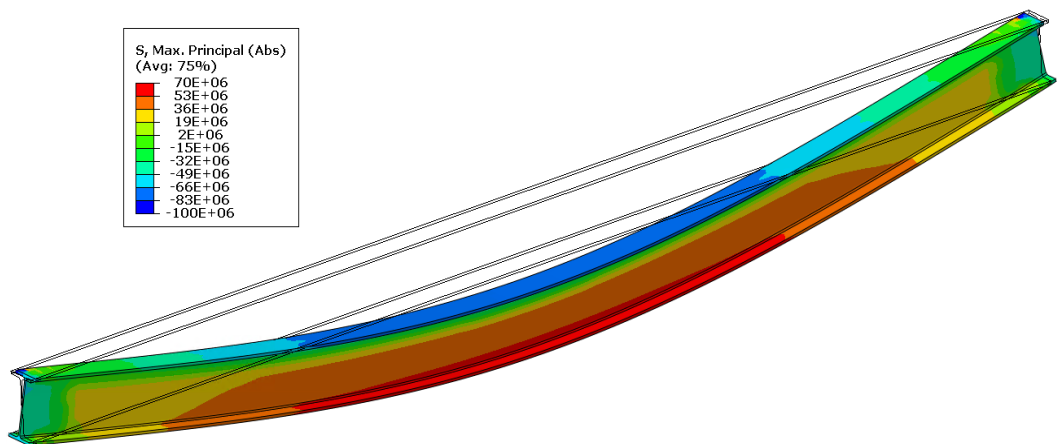


Figure 3-26: Beam stresses at 1200 sec- 0.25 ratio

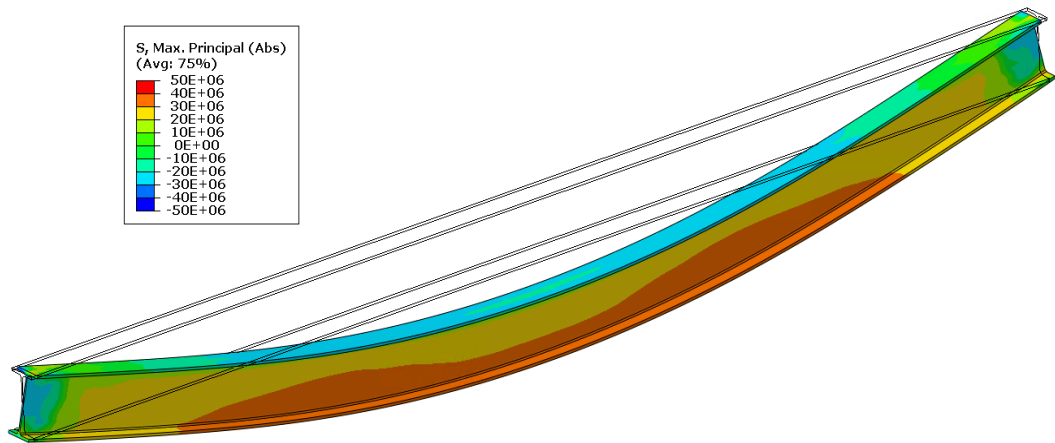


Figure 3-27: Beam stresses after fire step catenary action stage - 0.25 ratio

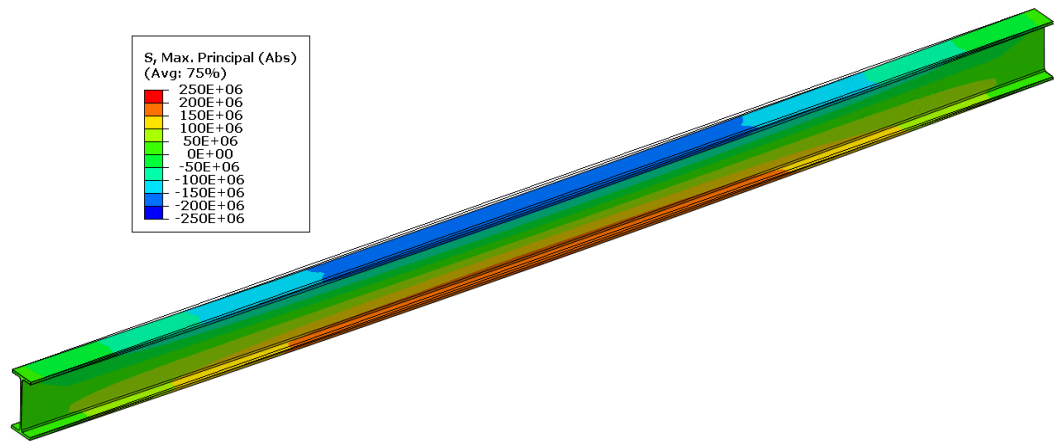


Figure 3-28: Beam stresses after loading step - 0.5 ratio

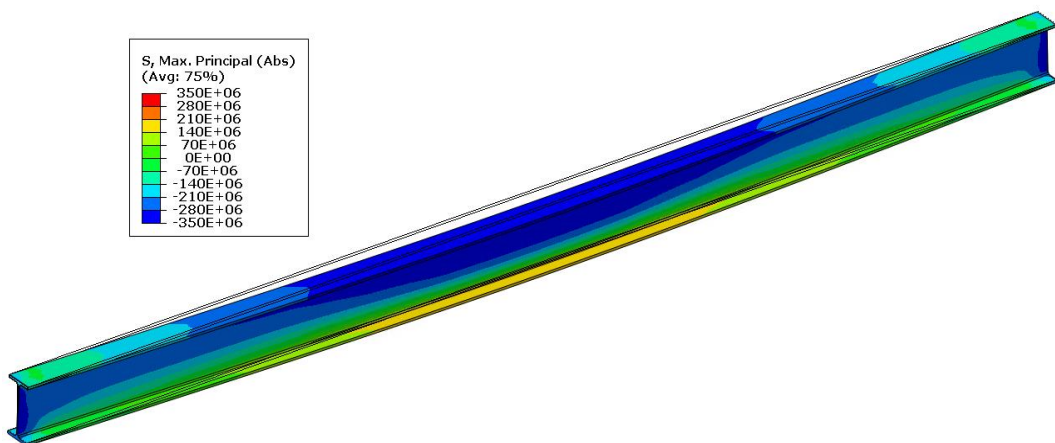


Figure 3-29: Beam stresses at 110 sec - 0.5 ratio

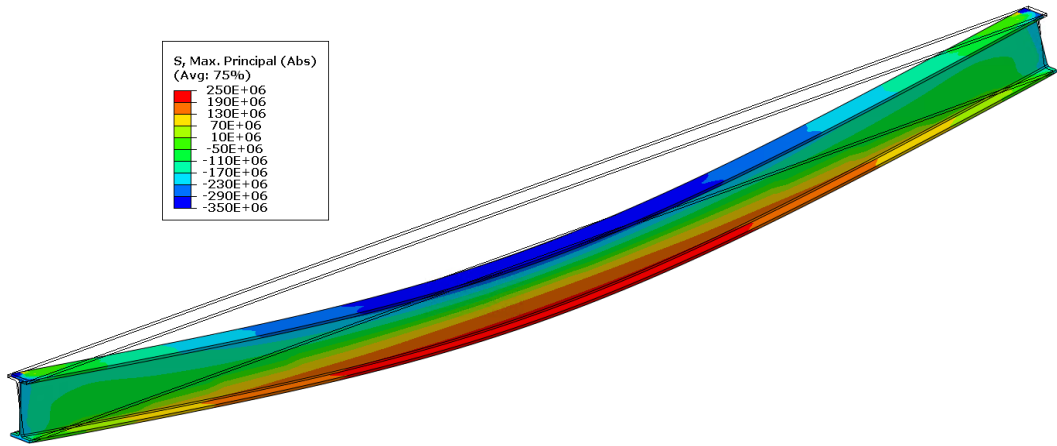


Figure 3-30: Beam stresses at 500 sec– 0.5 ratio

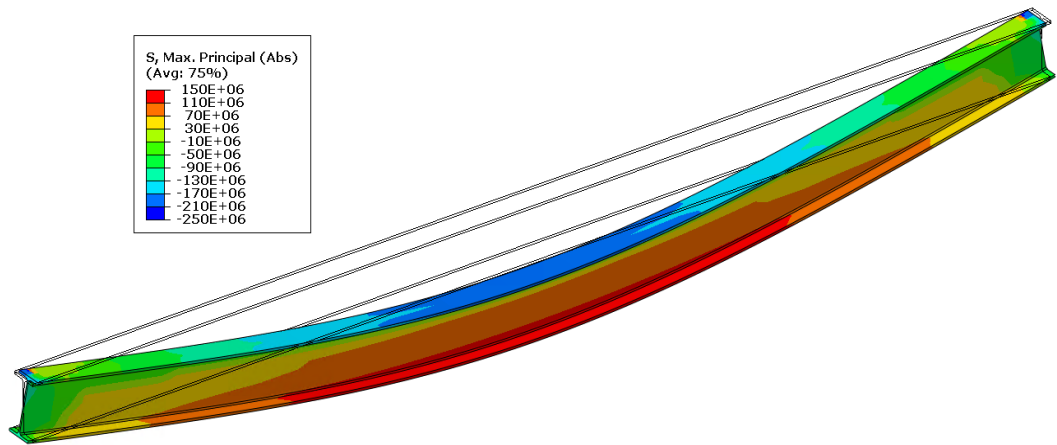


Figure 3-31: Beam stresses at 730 sec – 0.5 ratio

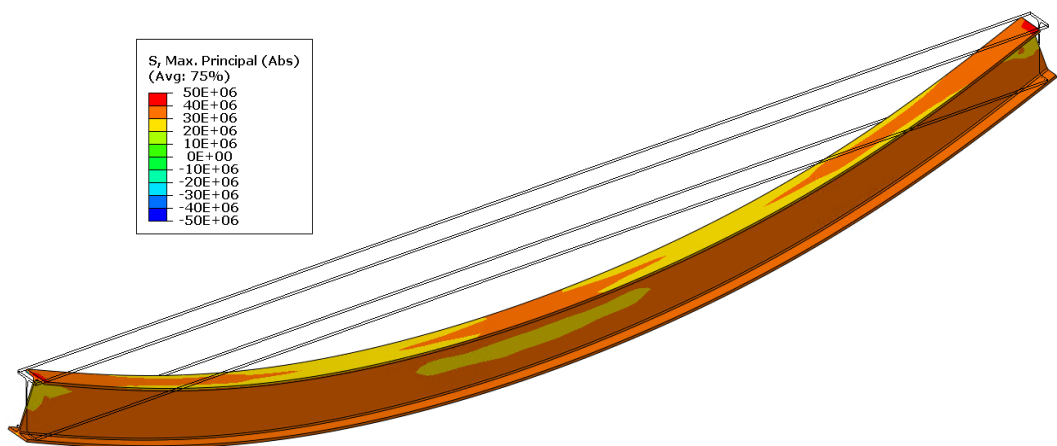


Figure 3-32: Beam stresses after fire step catenary action stage - 0.5 ratio

4. BEHAVIOUR OF COMPOSITE BEAM EXPOSED TO FIRE

To study the behaviour of composite beams exposed to fire, the coupling of thermal and mechanical analysis method verified by steel beams is applied further. The method is first validated by two benchmark tests and is used further for studying the load transferring mechanism inside composite beams exposed to the tested fire curves and under different load ratios.

The following contents are presented in this chapter: the finite element model of the composite beam and connections exposed to test-fire scenarios. Thermal and mechanical material properties at an ambient and elevated temperature for concrete slab, bolts, and reinforcing steel, that have been used in thermal and mechanical models. Different methods to validate the thermal and mechanical models with the test results. Defining beam load-carrying mechanism during different stages of the fire. The beam behaviour under different loading and test fire scenarios. Connection and shear stud behaviour during different load and fire cases.

4.1 Benchmark tests on composite beams at elevated temperatures

4.1.1 Fire test description

Purdue University conducted a series of fire tests for a fully loaded composite frame. Experimental investigations focused on individual composite beams with lightweight flat concrete slabs and simple beam-to-column connections. The purpose of the tests was to examine the behaviour of simple connections during heating and cooling stages with a static gravity loading applied over the mid-span of the beam. The composite beam and the connection were designed in accordance with US design practice and standards [30].

Figure 4-1 shows the portal frame prepared for the composite beam tests. The sample frame consists of a composite beam connected to a W14 x 109 column using a simple connection. The columns were protected with Fire Resistant Cement Spraying Material (SFRM) with a two-hour fire rating and the connections were deployed using sacrifice plates to protect the columns and they were able to be reused for other tests. For the shear tab connection, the plate was bolted to the beam and welded to the sacrificial plate. The sacrificial plate was then bolted to the W14 column flange [30].

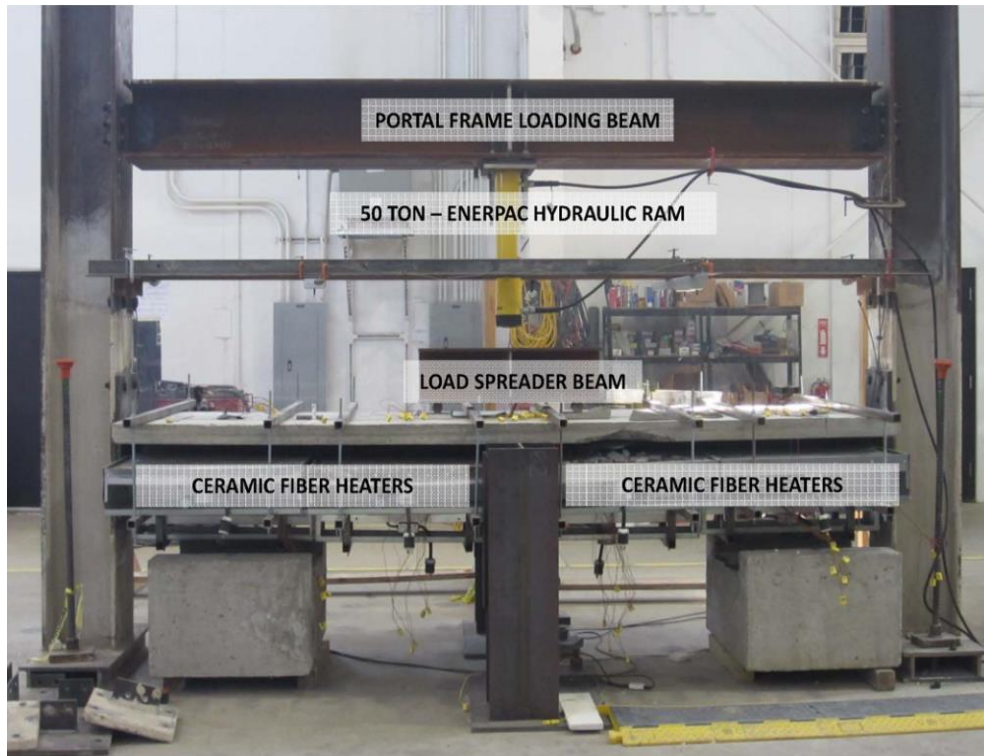


Figure 4-1: Test setup for composite beam exposed to fire [29]

The gravity loading was applied using a long-stroke actuator. The applied loading was distributed to two load points each located 305 mm from the beam midspan using a load spreader beam shown in Figure 4-2 [30].

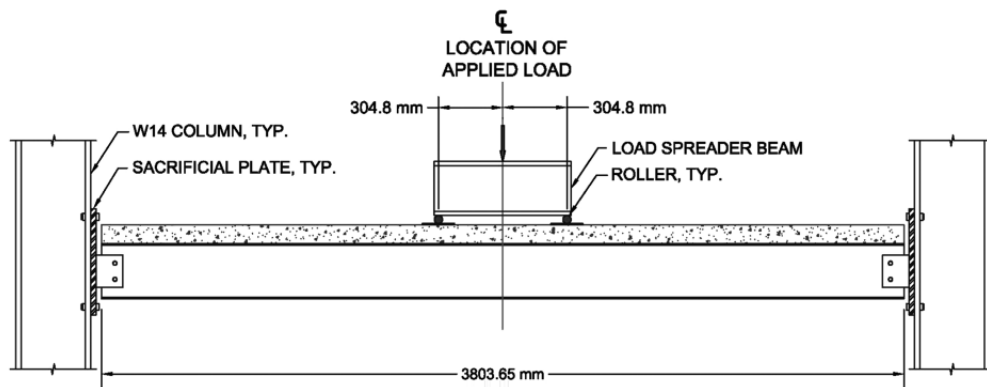


Figure 4-2: Elevation of loading for composite beam specimens [30].

The composite beam was a W10 × 22 steel beam topped by an 88.9 mm thick flat lightweight concrete slab that was 914 mm wide. The composite action between the slab and the beam using was created by 13 mm diameter shear studs spaced at 152 mm on the centre of the top flange along the length of the beam. A 6 × 6 W2.0 × 2.0 wire mesh reinforcement was used in the slab with a cover of 19 mm to provide a 2h fire-resistance rating. Four different connection types were used in the testing series as shown in Table 4-1. The focus of this thesis was on the shear tab connection type which was used with specimens CB-3 and CB-4 [29].

Table 4-1: Test Matrix for Simple (Shear) Connections of Composite Beams [28]

Specimen	Connection type	Beam size	Diameter of bolts [mm (in.)]	Size of weld [mm (in.)]	Thickness of simple (shear) connection [mm (in.)]	Ambient design strength of connection [kN (kip)]
CB-A	Shear-tab	W10 × 17	19 (0.75)	7.9 (0.31)	6.35 (0.25)	135 (30.4)
CB-1	All-bolted double-angle	W10 × 22	19 (0.75)	N/A	9.5 (0.375)	261 (58.7)
CB-2	All-bolted double-angle	W10 × 22	19 (0.75)	N/A	9.5 (0.375)	261 (58.7)
CB-3	Shear-tab	W10 × 22	19 (0.75)	7.9 (0.31)	6.35 (0.25)	135 (30.4)
CB-4	Shear-tab	W10 × 22	19 (0.75)	7.9 (0.31)	6.35 (0.25)	135 (30.4)
CB-5	All-bolted single-angle	W10 × 22	19 (0.75)	N/A	9.5 (0.375)	216 (48.6)
CB-6	All-welded single-angle	W12 × 22	N/A	6.35 (0.25)	9.5 (0.375)	150 (33.8)

Specimen CB-3 and CB-4 correspond to the third and the fourth heated composite beam tests and included the composite beams of W10 × 22 were connected to columns using a 6.35 mm thick shear-tab connection. The shear tab was attached to the web of the composite beam with 19 mm diameter bolts and was welded to the sacrificial plate using a 7.9 mm weld. The shear strength at ambient temperature was 135 kN. All the bolts used in the test specimens were ASTM A325. The joint details are shown in Figure 4-3 [30].

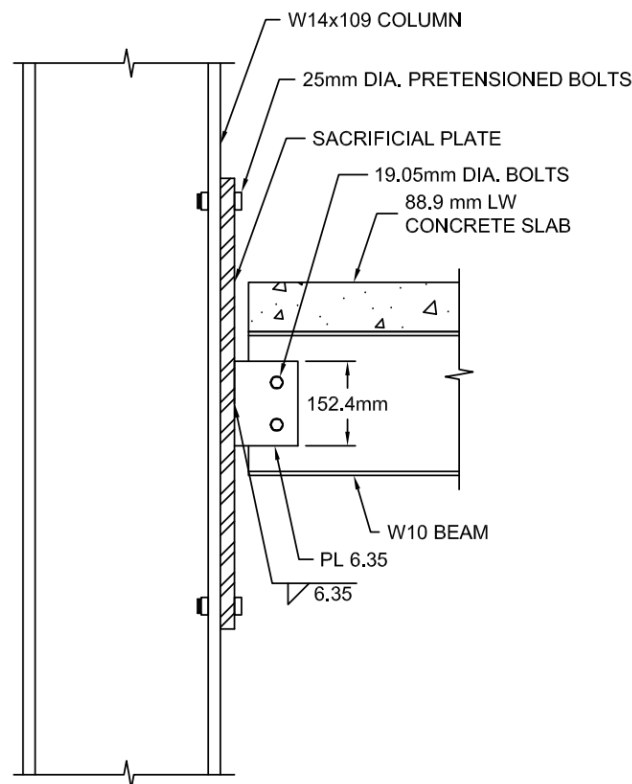


Figure 4-3: Shear-tab connection geometry [30]

4.1.2 Test CB-3

The objective of Test CB-3 was to evaluate the fire performance of shear-tab connections for a composite beam loaded to 60% of its load capacity at 20°C. The test setup for loading, heating and cooling the specimen is shown in Figure 4-4. A 156 kN load was applied at the midspan of the composite beam specimen before heating started and sustained while heating [29].

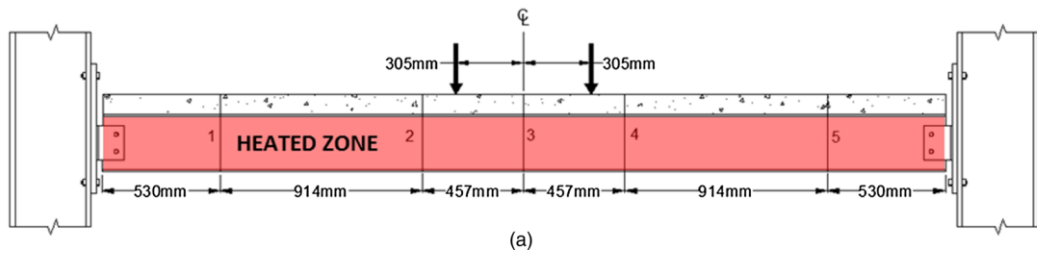


Figure 4-4: Loading and heating configuration [29]

High-temperature ceramic fibre heaters were used to heat the specimen of the composite beam as shown in Figure 4-5. The heater consists of a flat ceramic heater enclosed in a metal housing dedicated to photometry, the surface of the heater can reach a maximum temperature of 1250°C. Unlike a standard fire test, heaters work by controlling the temperature of the sample surface rather than the temperature of the gas in the furnace. The heaters used can be individually controlled, allowing different heating rates to be determined for the concrete and steel surfaces of the composite beam sample. Each heater operates with a single control feedback loop indicating the presence of a thermocouple on the surface of the test specimen. The heating power was controlled by comparing the current surface temperature with the heating profile selected by the user [30].

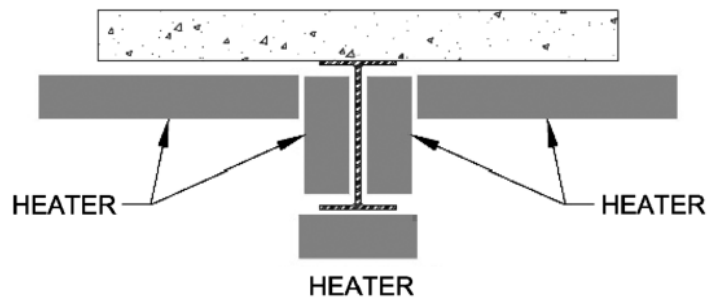


Figure 4-5: Heating layout of the composite beam cross-section [30]

The steel beam of the specimen was heated at a rate of 7°C/min and to the underside of the concrete slab at a rate of 4°C/min. the heating was stopped when the surface temperature of the bottom flange of the steel beam was 600°C. after that, both the steel beam and concrete slab were cooled at a rate of 12°C/min. the curves for heating and cooling of the composite beam are shown in Figure 4-6 [29].

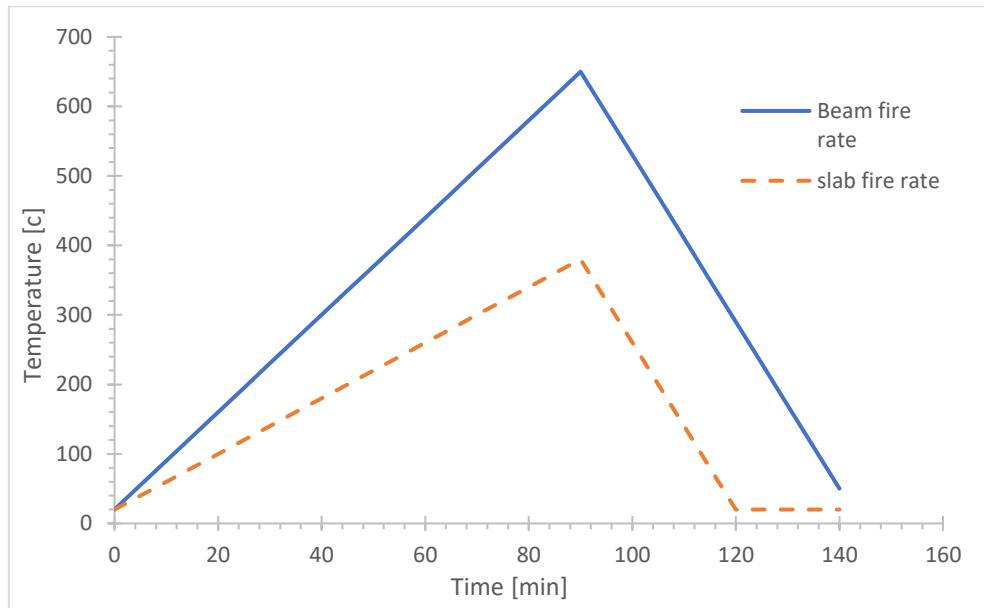


Figure 4-6: Heating and cooling curves for the steel beam and concrete slab in test

Table 4-2 shows a summary of the cases that will be studied in thermal and mechanical analyses models

Table 4-2: Summary of the studied cases

Cases	Based on	Thermal model method	Max-temp [°C]	Load [kN]
Case 1	CB-3	Heat flux	600	156
Case 2	CB-3	Surface temperature without heat exchange	600	156
Case 3	CB-3	Surface temperature with heat exchange	600	-
Case 4	CB-4	Heat flux	700	111

4.2 Model for thermal analysis

The target of thermal analysis was to predict the temperature distribution in the beam and connection section of the steel framework. A FE model was created to simulate a 3D cross-section of the column, beam with shear studs, slab with reinforcing mesh, connection plates and bolts section. The underside of the bottom flange, the web of the steel beam, and the underside of the slab were exposed to fire.

4.2.1 FE geometry and meshes

4.2.1.1 Geometry

A full 3D model was created for the frame with connections for thermal analysis following the dimension of the frame as shown in Figure 4-3 and Figure 4-4. Two columns had a W cross-section based on a wide flange profile of W14x109. The beam between the columns had a W cross-section based on a wide flange profile of W10x22 and a length of 3810 mm. One sacrificial plate was tied to each column with a thickness of 22 mm. One shear plate was tied to each sacrificial plate and bolted to the web of the beam with 2xD19 bolts on each end of the beam. Two holes were created in each shear plate for the bolts. Similarly aligned holes were created on both ends of the beam so the bolt could go through with a diameter of 19 mm. The bolt threads were excluded from the 3D FEM models as well. The bolt head and nut were included in the detailed model. Shear plate geometry was 152x84x6.4 mm. A concrete slab thickness of 88.9 mm was modelled above the beam with a geometry of 914x3810 mm with a zero-gap from the beam top flange. A shear stud with a 19 mm diameter was connected to the top side of the beam and modelled inside the concrete slab using embedded interaction. The reinforcing mesh was modelled inside the slab and connected to the slab using embedded interaction. The mesh bars had a diameter of 6 mm with a spacing of 51 mm and a concrete cover of 19 mm from the slab bottom face as shown in Figure 4-7.

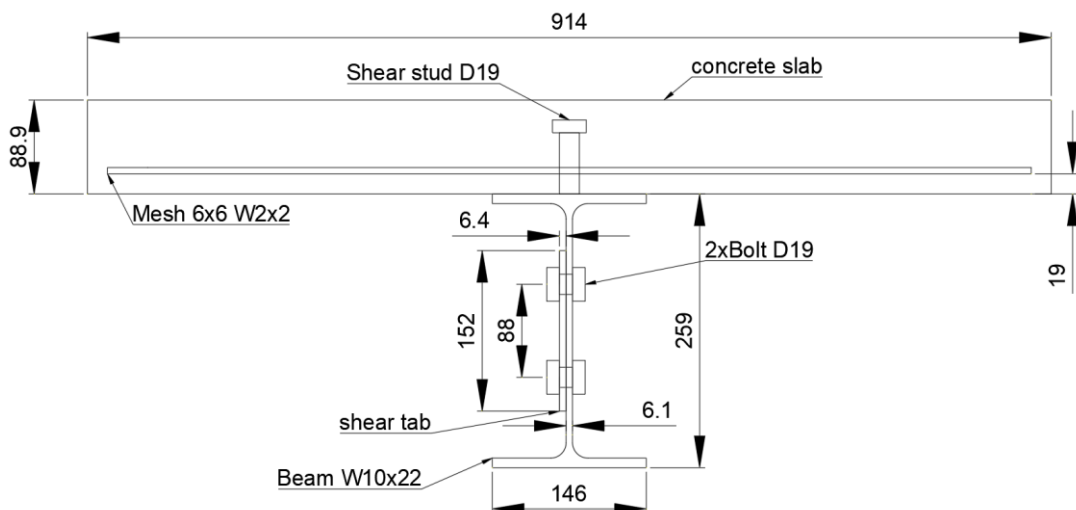


Figure 4-7: Frame cross-section geometry

4.2.1.2 Mesh and element properties:

All elements were modelled as solid elements except for the shear studs and reinforcing mesh was modelled as 2D truss elements. Therefore, an 8 node-linear heat transfer brick element was used to model all solid element cross-sections which required 20220 hexahedral elements of type DC3D8. A 2-node heat transfer link was used to model the truss elements which required 1025 linear line elements of type DC1D2. The 3D thermal model mesh consists of 33446 nodes and 21245 elements with a mesh size range between 5-50 mm. The mesh was finer at the connection region. The model used two layers of finite elements through the thickness of the beam web and the flange of the steel beam, and two layers of finite elements through the thickness of the slab and the shear tab as shown in Figure 4-8 and Figure 4-9. Heat transfer mesh was used for all elements. The universal beam section and the surface contact with the concrete slab area were assigned with the same mesh size so the nodes were aligned with each other for better contact.

The embedded element technique was used to specify that a group of elements (shear studs and reinforcing mesh) were embedded in the host element (concrete slab). Abaqus searched for the geometric relationships between nodes of the embedded elements and the host elements. If a node of an embedded element is located inside a host element, the translational degrees of freedom and pore pressure degree of freedom at the node were eliminated and the node became an embedded node. The translational degrees of freedom and pore pressure degree of freedom of the embedded node were constrained to the interpolated values of the corresponding degrees of freedom of the host element. Embedded elements were allowed to have rotational degrees of freedom, but these rotations were not constrained by the embedding [32].

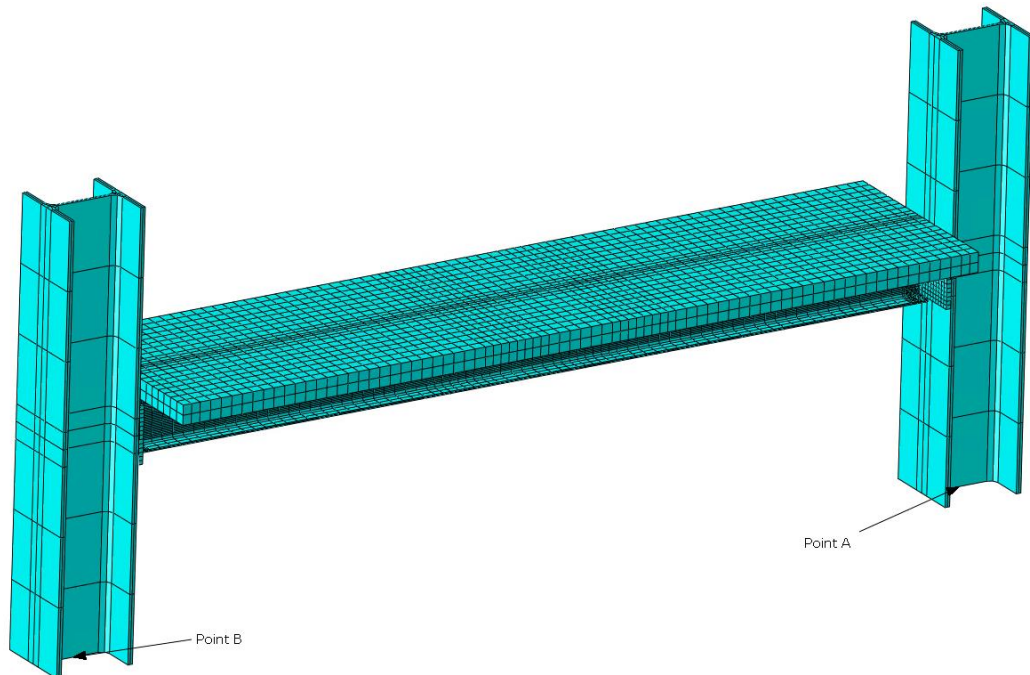


Figure 4-8: Overall 3D FEM model

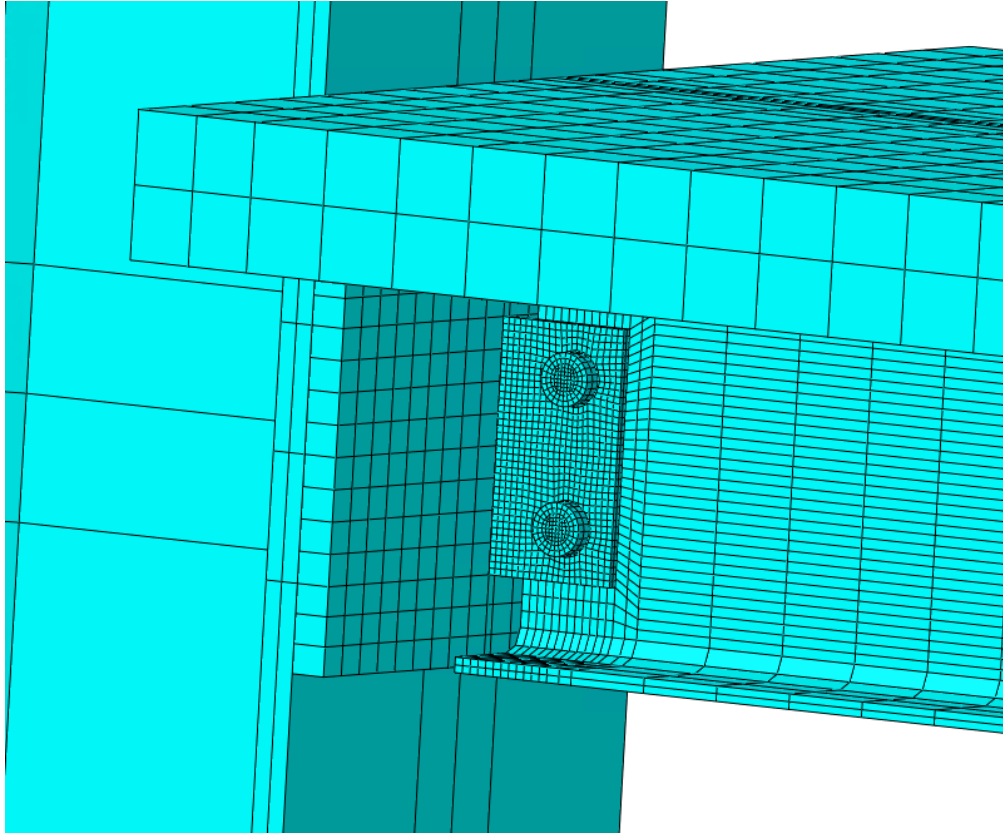


Figure 4-9: Zoom-in view of the connection

4.2.1.3 Predefined fields

The initial temperature of 20°C was defined using a predefined temperature field for the whole model.

4.2.1.4 Model setup and analyses

A transient heat transfer analysis was performed for the frame using the Abaqus/Standard heat transfer procedure with an automatic time step size for a total period of 7800 sec (130min). Absolute zero temperature was defined as -273.16°C and the Stefan-Boltzmann constant as $5.67e-8 \text{ W}\cdot\text{m}^{-2}\cdot\text{K}^{-4}$. International System of Units (SI) was used for all models.

4.2.2 Thermal boundary conditions

Three different boundary conditions were used to validate the FE model. The details are explained in this section.

4.2.2.1 Case 1: Heat flux

Heat flux was defined as boundary conditions for exposed and unexposed surfaces. The convection coefficient for gas temperature on the exposed side was $25 \text{ W/m}^2\text{K}$ and it was $9 \text{ W/m}^2\text{K}$ on the unexposed side according to EN 1991-1-2 [2002] as shown in Figure 4-10 and Figure 4-11. The emissivity coefficient was 0.7 for radiation, according to EN 1992-1-2 [2005]. The columns were considered to be exposed to the room ambient temperature of 20°C during the heating and cooling phases. Between the connection parts [bolts, plates, and beam] and between the beam topside and the concrete slab thermal contact was defined using an option of high conductivity to allow the heat transfer between the contacted parts. The reference temperature for the unexposed surface was defined as 20°C .

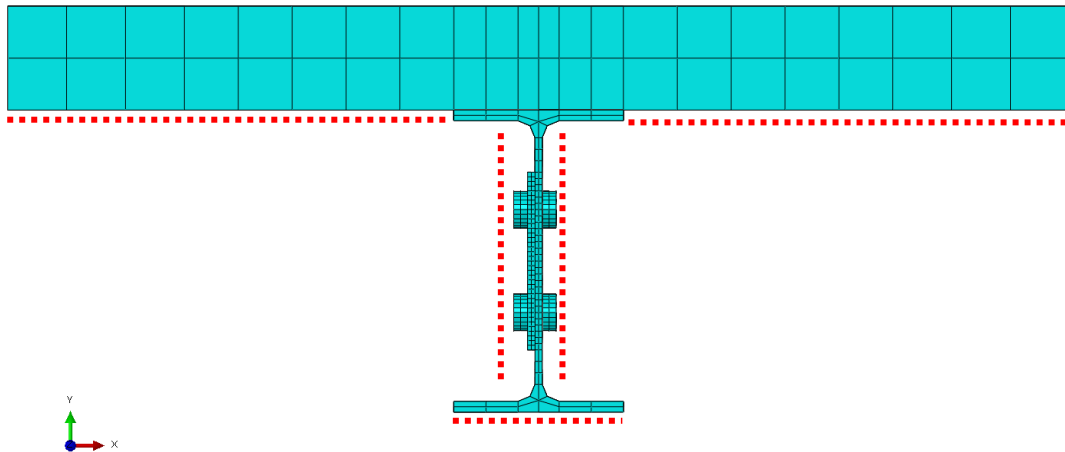


Figure 4-10: Exposed surface to fire

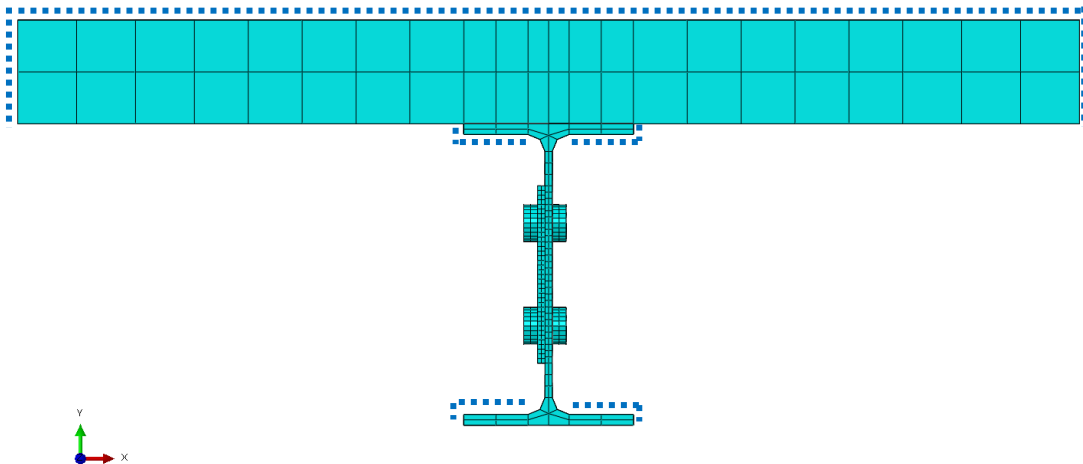


Figure 4-11: Unexposed surface to fire

The heating method used in the test was different from the furnace test or compartment fire, where gas temperatures are known. Therefore, a different approach was used to adjust the heating and cooling rates for the beam and slab to achieve the maximum temperature at the same time as the test. Time-temperature curves were defined as amplitude. Heating AMPLITUDE was defined for 4620 sec (77 min) with a heating rate of 9°C/min for the air underside of the steel beam, 7°C/min for the air around the web of the steel beam, and 6.5°C/min for the air underside of the concrete slab. Cooling AMPLITUDE was defined for both web and slab with rates of 11°C/min and 12°C/min for the air around the bottom flange for 3180 sec (53 min) as shown in Figure 4-12.

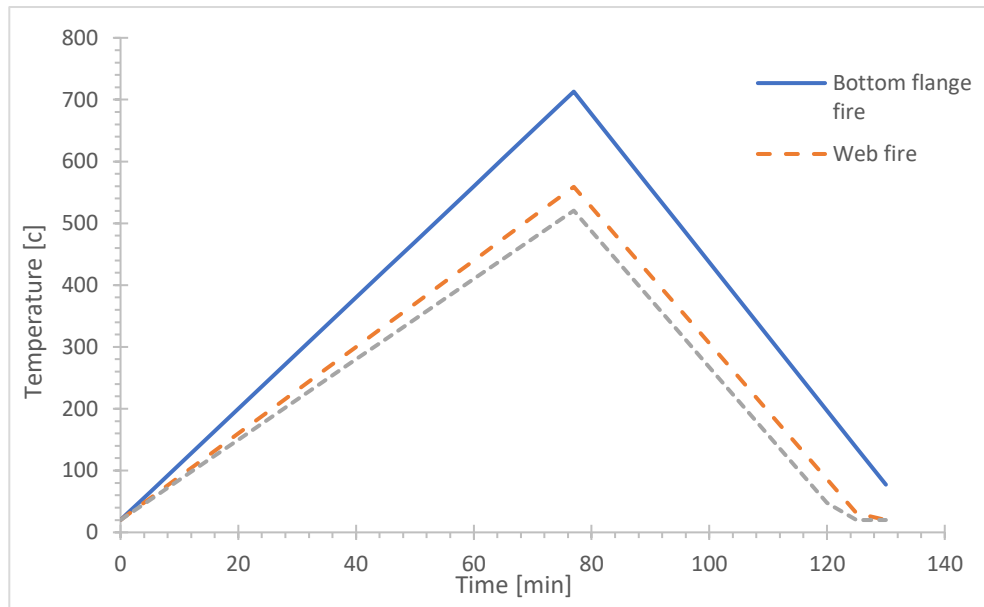


Figure 4-12: Beam and slab heating and cooling rate

4.2.2.2 Case 2: Surface temperature without heat exchange

A surface temperature was defined for exposed surfaces. The temperature histories that were measured during the test for the undersurface of the bottom flange, the web, the undersurface and the top surface of the concrete slab were used as surface temperature boundary conditions instead of applying the gas furnace method where the time-temperature was defined as amplitude, and convection and radiation coefficient were defined. Figure 4-13 shows the temperature histories that were used as surface temperature boundary conditions.

Thermal contact was defined with high conductivity to allow the heat transfer between connection parts [bolts, plates, and beam] and between the upper surface of the top flange of the steel beam and the concrete slab.

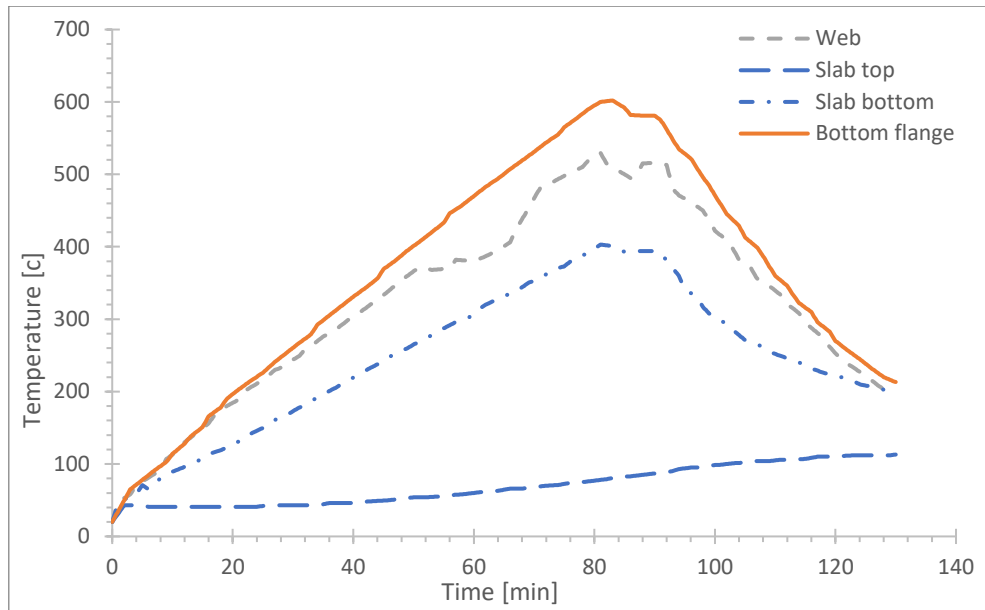


Figure 4-13: heated surface temperature histories

4.2.2.3 Case 3: Surface temperature with heat exchange

A surface temperature was defined similarly to Case 2. The difference between Case 3 and Case 2 was that the convective heat flux was allowed for the top flange of the steel beam because the top flange was not heated during the test.

4.2.3 Thermal material properties of concrete

The density, temperature-dependent thermal conductivity, and specific heat of steel elements [column, beam, bolts, shear stud, reinforcing bars] were defined according to EN 1993-1-2 [2005] as described in section 3.2.2. The temperature-dependent density, thermal conductivity, and specific heat of concrete slab were defined in this section according to EN 1992-1-2 [2004].

4.2.3.1 Concrete C30 thermal conductivity λ

Thermal conductivity depends on the type of aggregate and the temperature of the concrete. EN 1992-1-2 [2004] recommends the following equation for the thermal conductivity of siliceous aggregate.

For the upper limit of thermal conductivity of normal concrete

$$\lambda = 2 - 0.2451 \cdot (\theta/100) + 0.0107 \cdot (\theta/100)^2 \rightarrow 20^\circ\text{C} \leq \theta < 1200^\circ\text{C}$$

Equation 13

For the lower limit of thermal conductivity of normal concrete

$$\lambda = 1.36 - 0.136 \cdot (\theta/100) + 0.0057 \cdot (\theta/100)^2 \rightarrow 20^\circ\text{C} \leq \theta < 1200^\circ\text{C}$$

Equation 14

Where λ is thermal conductivity (W/mK)
 θ is the steel temperature.

The thermal conductivity for different types of concrete derived according to these equations is shown in Figure 4-14.

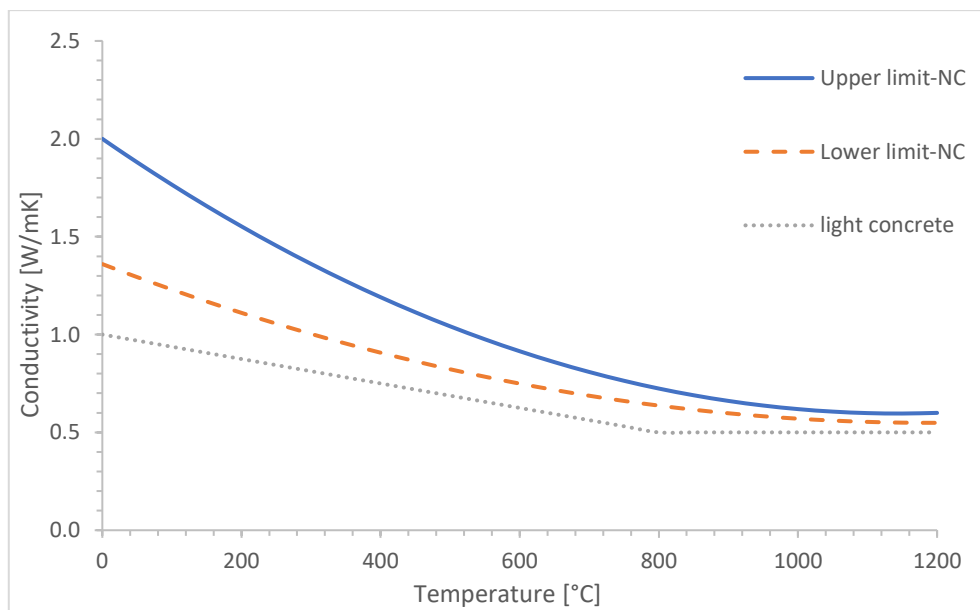


Figure 4-14: thermal conductivity of normal weight concrete as a function of temperature [35]

4.2.3.2 Concrete C30 specific heat C_p

The specific heat of concrete varies mainly with the different moisture content. The humidity inside the concrete causes a peak between 100°C and 200°C due to the evaporation of free water from the concrete. Eurocode EN 1992-1-2 [2004] recommends the following relationship for calculating the specific heat of concrete.

$$C_p = 900 \rightarrow 20^\circ\text{C} \leq \theta < 100^\circ\text{C}$$

Equation 15

$$C_p = 900 + (\theta - 100) \rightarrow 100^\circ\text{C} \leq \theta < 200^\circ\text{C}$$

Equation 16

$$C_p = 1000 + \frac{\theta - 100}{2} \rightarrow 200^\circ\text{C} \leq \theta < 400^\circ\text{C}$$

Equation 17

$$C_p = 1100 \rightarrow 400^\circ\text{C} \leq \theta < 1200^\circ\text{C}$$

Equation 18

$$C_p = 2020 \rightarrow \text{for } 3\% \text{ moisture content of concrete weight}$$

Equation 19

Where C_p is the specific heat [J/kgK],
 θ is the steel temperature.

The specific heat of concrete derived according to these equations is shown in Figure 4-15. The peak between 100°C and 200°C due to water expulsion should be included with the above equation in the temperature range from 100°C to 200°C

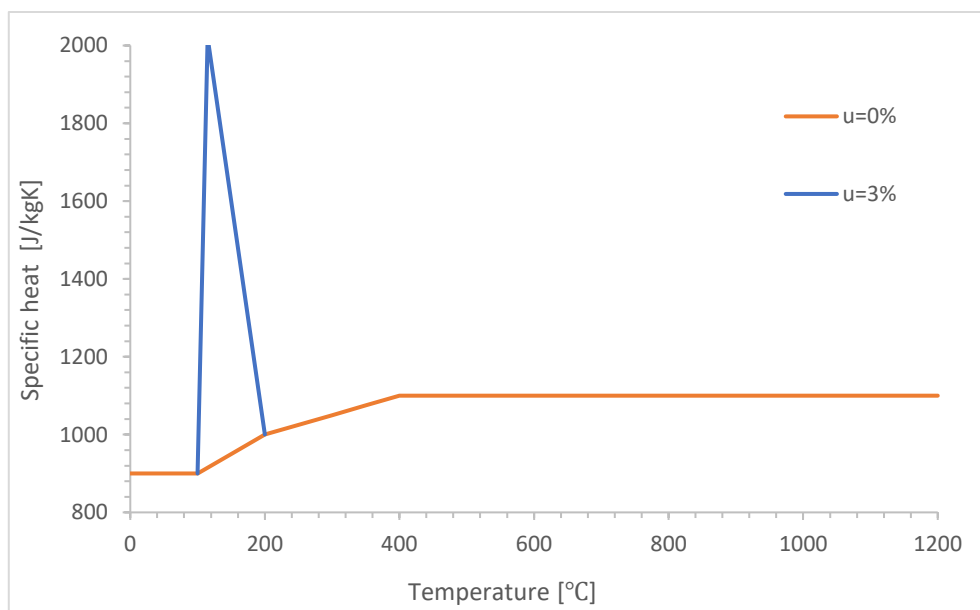


Figure 4-15: Specific heat as a function of temperature [35]

4.3 Model for structural analyses

One FE model using 3D solid elements was created to simulate the benchmark test. The analysis was performed using explicit methods. Figure 4-8 illustrated the FE model using solid elements for all parts except for the shear studs and the reinforcing mesh. In structural analysis, temperature histories for predefined temperature fields due to fire heating and cooling phase were obtained from thermal analysis and described in section 4.2. The slab was loaded by a vertical load of 156 kN, 2 points along the span of the beam with a distance of 305 mm from the midpoint of the slab as shown in Figure 4-4.

4.3.1 FE geometry and meshes

4.3.1.1 Geometry

The same geometry as in the thermal model described in section 4.2.1 was used for the mechanical model. Shear stud connection with the top flange of the steel beam was defined as a zero-length connector element. The force-displacement response of the connector element in the beam longitudinal direction was specified using the force-slip temperature dependant behaviour developed by Zhao and Kruppa [31], As shown in Figure 4-16. The maximum slip was defined as the peak load of the connector being reached. For the flat slab, this was equal to 5.2 mm.

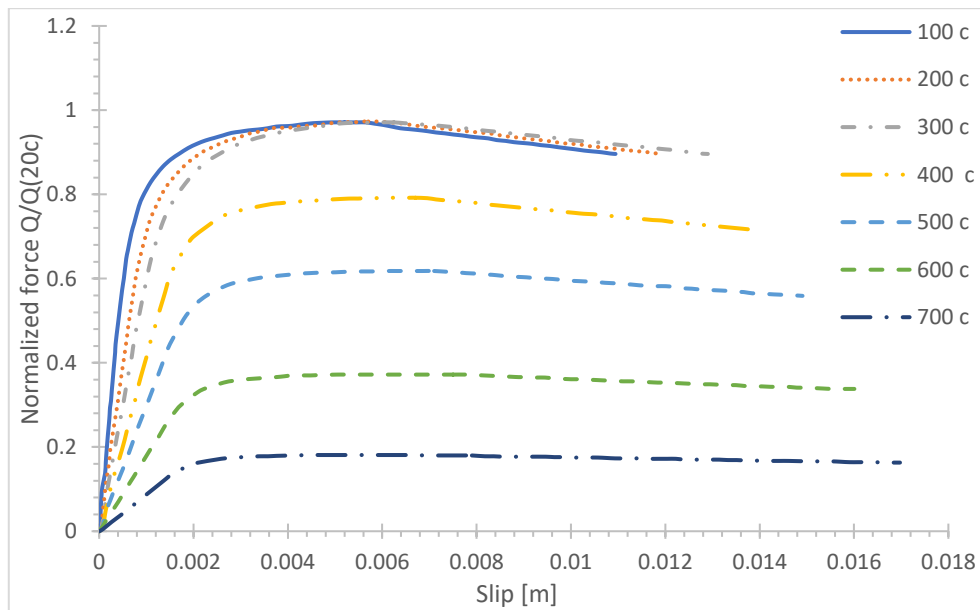


Figure 4-16: Temperature-dependent force-slip behaviour for shear connectors with flat concrete slab [31]

4.3.1.2 Mesh and element properties

All elements were modelled as solid elements except the shear studs were modelled as a 2D beam element and the reinforcing mesh was modelled as a 2D truss element. Therefore, the steel parts [column, beam, plates, bolts] and concrete slab were modelled as solid elements cross-section which create 20220 hexahedral elements of type C3D8R (An 8-node linear brick, reduced integration, hourglass control). A 2-node linear 3D truss was used to model the reinforcing mesh

elements which create 900 linear line elements of type T3D2. A 2-node linear beam was used to model the shear stud elements which create 125 linear line elements of type B31. 3D mechanical model mesh statistic consists of 33446 nodes and 21245 elements with a mesh size range between 5-50 mm. The mesh was finer at the connection region. The model used two layers of finite elements through the thickness of the beam web and the flange. Two layers of finite elements through the thickness of the slab and the shear tab as shown in Figure 4-8 and Figure 4-9. An explicit mesh type was used for all elements. The universal beam section and the surface contact with the concrete slab area were assigned with the same mesh size so the nodes were aligned with each other for better contact. Typical meshes were used in thermal and mechanical models for compatibility.

4.3.1.3 Interaction

General contact was defined for all contact surfaces of connection parts [bolts, plates, and beam] and between the beam topside and the concrete slab with a 0.35 penalty friction coefficient for tangential behaviour and hard contact allowing the contact separation. General contact was used in the initial step and propagated during the loading, heating, and cooling steps. Tie constraint was used between the welded elements, between the shear plate and the sacrificial plate, and between the sacrificial plate and the column. Inside the concrete slab, the embedded constraint was used to simulate the relation between reinforcing mesh and shear studs with the concrete slab. Similar embedded element techniques were used in the structural model as described in section 4.2.1 [32].

The coupling constraint was used at the bottom end of the columns to couple all the nodes at the end surface to the reference points (points A and B) as shown in Figure 4-8 where the boundary conditions were applied later. Zero-length connector elements were used to tie the shear studs to the top surface of the steel beam. The properties of the connector element were defined as temperature dependant force-slip functions as shown in Figure 4-16 [31].

4.3.1.4 Loads and boundary conditions

Fixed boundary conditions were defined for the lower end of the frame columns (points A and B) as shown in Figure 4-8. Lateral bracing was used during the test to prevent the frame rotation about the longitudinal axis of the beam due to the eccentricity of the beam joints to the columns. The bracing was installed in the mid of the beam on both sides. A similar constrain was used in ABAQUS to prevent the frame from turnover. The out-of-plane deflection of the top flange was prevented at the mid-span as shown in Figure 4-17. An axial compressive load of 156 kN was modelled as 3.5 MPa pressure at two surfaces (152x146 mm) with equally spaced positions from the midpoint along the span of the beam as shown in Figure 4-18. Gravity load was defined to include the frame self-weight during the simulation. Gravity acceleration of 9.81 m/s^2 in the vertical direction was used to simulate the self-weight. In ABAQUS/Explicit, the mechanical loading was applied by increasing its value linearly from zero to the maximum in the mechanical loading phase and was kept constant throughout the heating and cooling phase. Figure 3-7 shows the loading curve for both phases. The pressure force was defined with a reference amplitude load curve.

4.3.1.5 Predefined fields

Room temperature and temperature histories due to the fire were applied as predefined fields at the nodes of the cross-section. The thermal analysis was performed first as described in section 4.2. The output file from the thermal analyses was transferred to the nodes of the model after the mechanical loading step was finished. For mechanical loading steps, the uniform temperature of 20°C was defined.

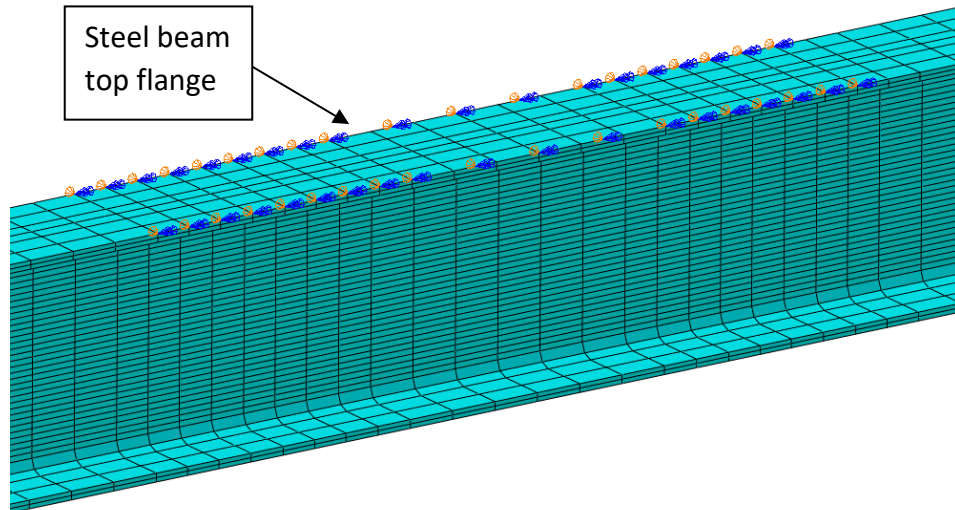


Figure 4-17: Close view of the lateral bracing boundary condition

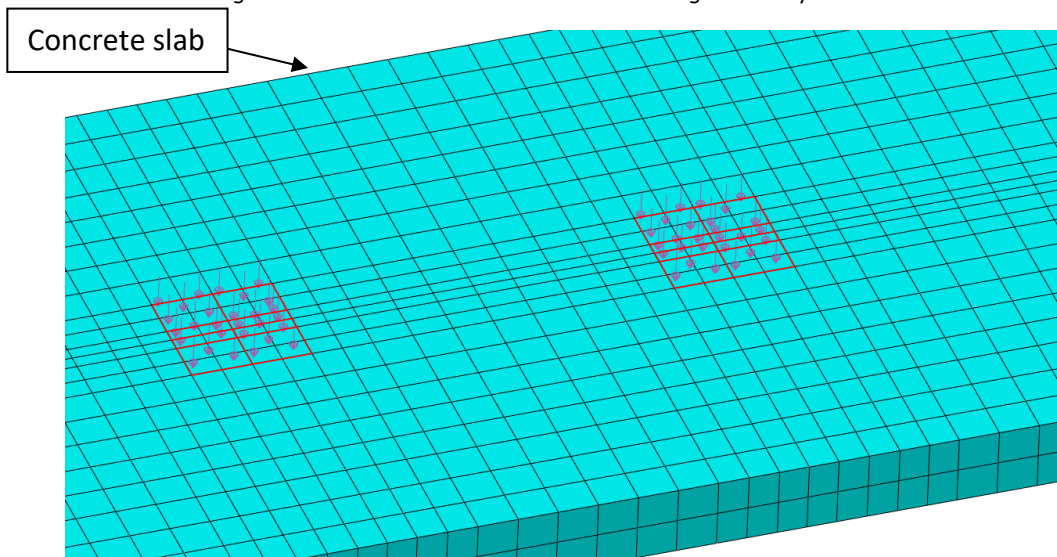


Figure 4-18: Close view of FE model loading step

4.3.1.6 Model setup and analyses

The structural analysis was performed using Abaqus/Explicit dynamics procedure. The total simulation time was scaled with mass scaling as the model was quite large and required a long time to run the simulation. In ABAQUS, The analysis was performed in two steps: the mechanical loading was added in the first step for 30 sec as problem time and the fire simulation including heating and cooling phases for 7800 sec (130min). Mass scaling, as described before in section 3.3.1, was set to $2e+04$ for the loading phase and $1.6e+06$ for the fire heating and cooling phase.

4.3.2 Mechanical properties of the material

Mechanical steel material properties density, temperature-dependent isotropic elasticity, temperature-dependent coefficient of thermal expansion and temperature-dependent plasticity were defined according to EN1993-1-2 [2005] as defined in section 3.3.2 for steel elements [column, beam, plates]. Steel beams and plates were modelled with a yield strength of 355 MPa. Bolts and shear studs were modelled as grade 8.8 with a yield strength of 640 MPa. Reinforcement mesh was modelled as A500 with a yield strength of 500 MPa.

For concrete, its temperature-dependent density, temperature-dependent isotropic elasticity, temperature-dependent coefficient of thermal expansion and temperature-dependent plasticity were defined according to EN1992-1-2 [2004]. The details are explained in this section.

4.3.2.1 Steel grade 8.8 ambient properties

At room temperature, the following ambient material properties have been used for bolts considered within this report.

Table 4-3: Properties of steel grade 8.8 at ambient temperature

Property	Notation	Value
Yield strength [MPa]	f_y	640
Poisson's ratio	n	0.3
Elastic modulus [GPa]	E	210
Density [kg/m ³]	r	7850

4.3.2.2 Mechanical properties of steel grade 8.8 at elevated temperatures

The reduction factors based on EN1993-1-2 [2005] are shown in Figure 4-19. The stress-strain curves at elevated temperature for the bolt based on the reduction factors are shown in Figure 4-20.

The symbols used in Figure 4-19 are defined as follows:

- $k_{y,\theta}$ is the ratio of the yield strength at elevated temperature to the yield strength at 20°C.
- The reduction factors of elasticity and proportional limit were taken as explained in section 3.3.2.2.

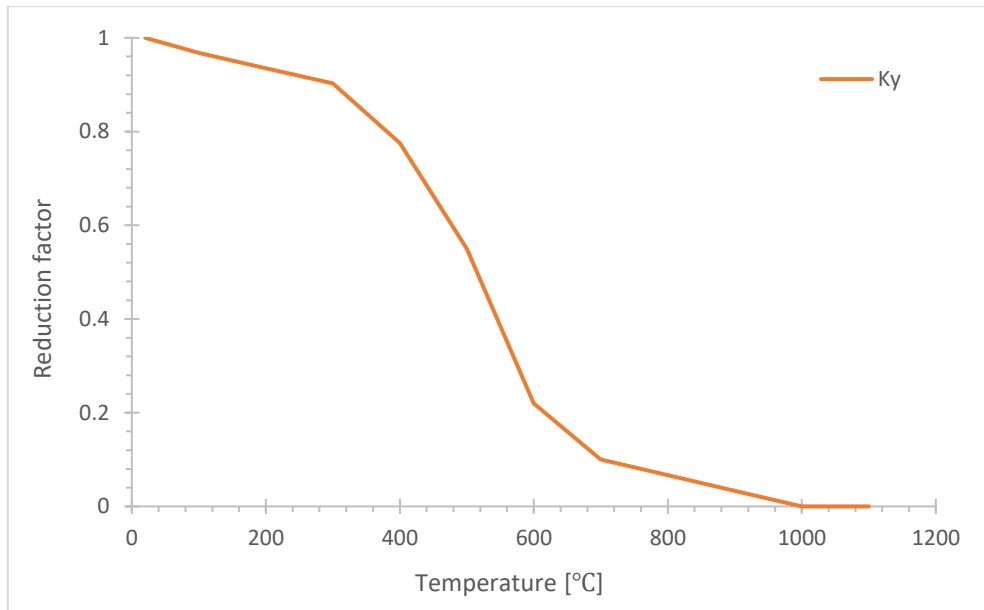


Figure 4-19: Reduction factors for the stress-strain relationship of bolts at elevated temperatures [33]

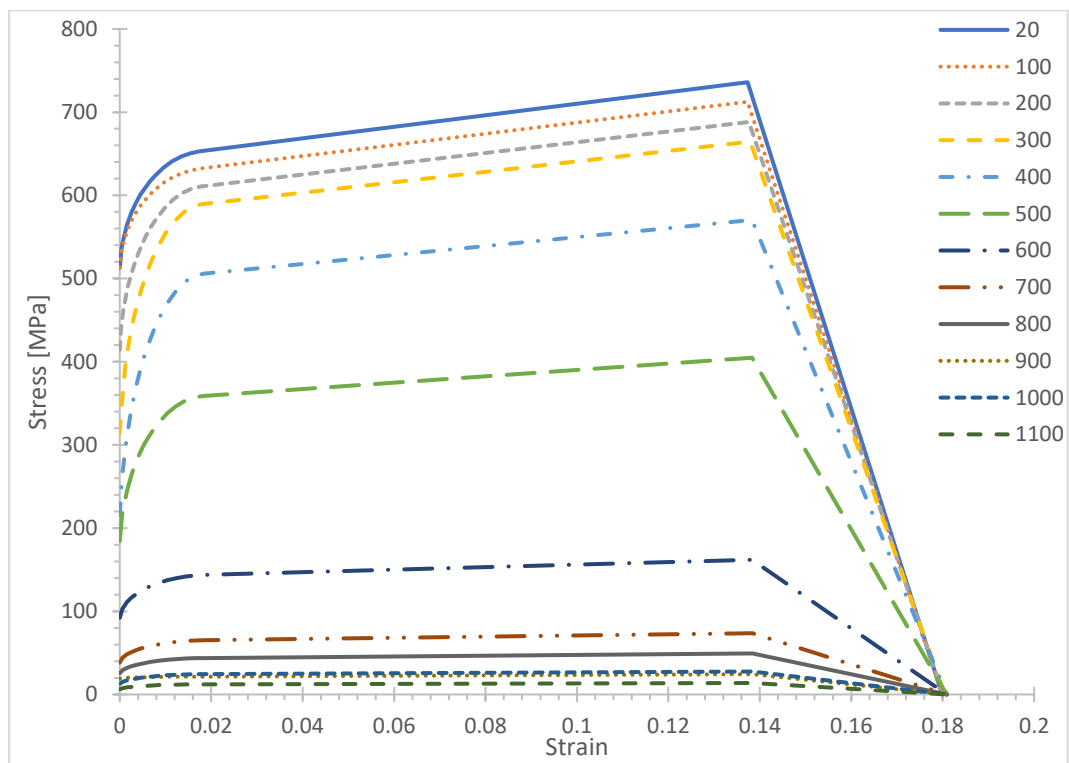


Figure 4-20: stress-strain curves for bolt 8.8 at different temperatures [33]

4.3.2.3 Properties of A500 steel at ambient temperature

At room temperature, the material properties for reinforcing steel A500 are defined in Table 4-4.

Table 4-4: Properties of steel A500 at ambient temperature

Property	Notation	Value
Yield strength [MPa]	f_y	500
Poisson's ratio	ν	0.3
Elastic modulus [GPa]	E	210
Density [kg/m ³]	ρ	7850

4.3.2.4 Properties of A500 steel at elevated temperatures

The temperature-dependent mechanical properties of A500 steel were taken from the EN1992-1-2 [2004]. The reducing factors for elastic modulus, yield strength, and proportional limit are shown in Figure 4-21.

The symbols used in Figure 4-21 are defined as follows:

- $k_{E,\theta}$ is the ratio of the elastic modulus at elevated temperature to the elastic modulus at 20°C.
- $k_{y,\theta}$ is the ratio of the yield strength at elevated temperature to the yield strength at 20°C.
- $k_{p,\theta}$ is the ratio of the proportional limit at elevated temperature to the proportional limit at 20°C

The elastic modulus determined using the reduction factors is shown in Figure 4-22. Stress-strain curves at elevated temperatures for A500 steel are shown in Figure 4-23.

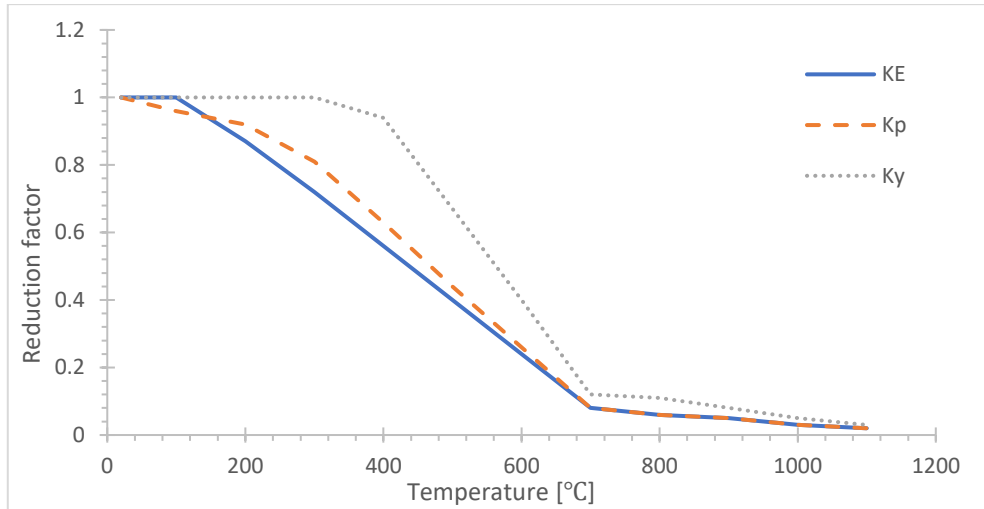


Figure 4-21: Reduction factors of the steel A500 stress-strain relationship at elevated temperatures [35]

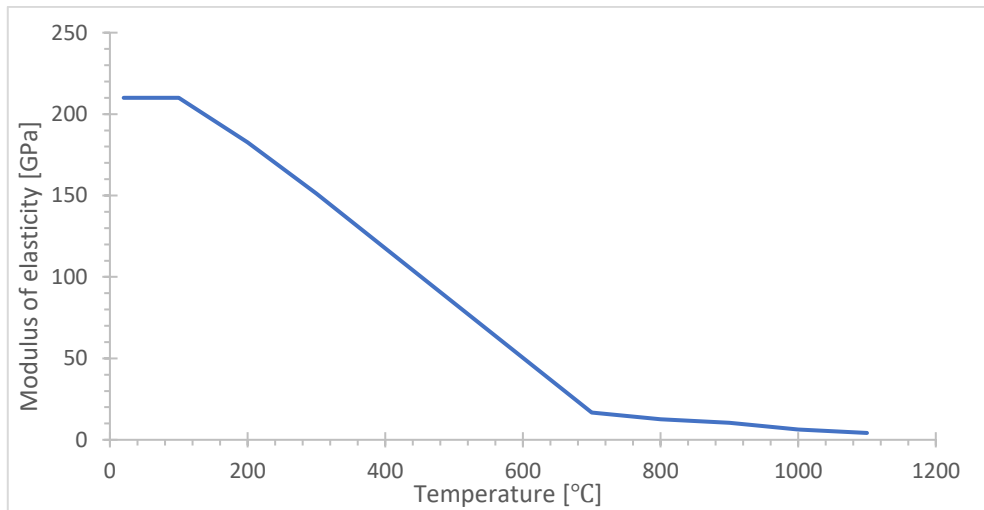


Figure 4-22: Modulus of elasticity for steel A500 as a function of temperature [35]

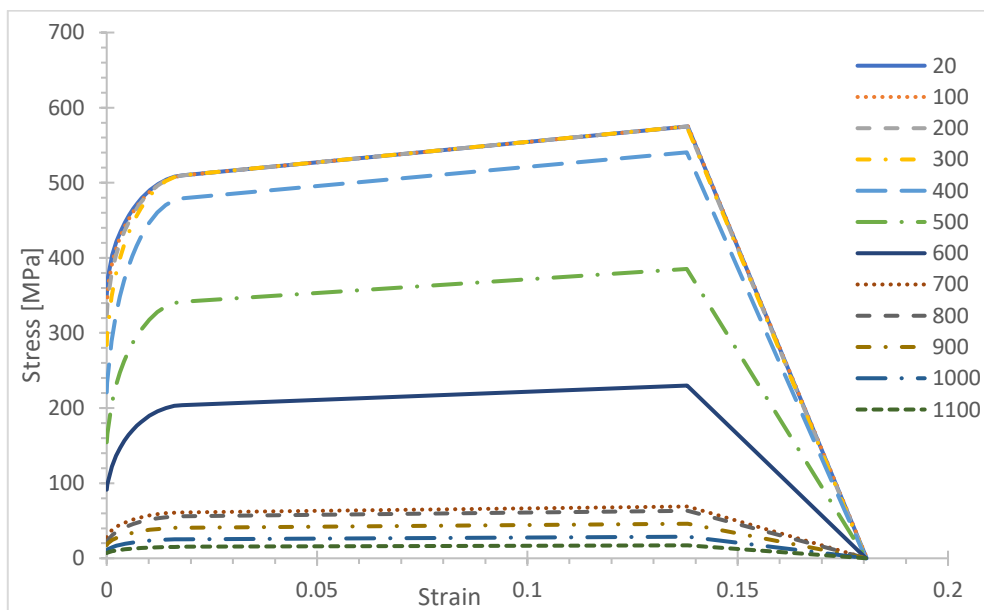


Figure 4-23: Stress-strain curves for A500 at different temperatures [33]

4.3.2.5 Properties of C30 concrete at ambient temperature

At room temperature, the material properties in Table 4-5 were used for all concrete within this report.

Table 4-5: Properties of siliceous concrete at ambient temperature

Property	Notation	Value
Compressive strength [MPa]	f_c	30
Tensile strength [MPa]	f_t	2.9
Poisson's ratio	ν	0.2
Elastic modulus [GPa]	E	33
Density [kg/m ³]	ρ	2300

The concrete section is supposed to crack at zero stress under tension to avoid arithmetic errors during simulation. In fact, concrete has some tensile strength which is not great. This assumption can be used although not expect much difference between the simulation results and the real situation.

4.3.2.6 Properties of C30 concrete at elevated temperatures

The temperature-dependent mechanical properties of concrete were taken from EN1992-1-2 [2004]. The reduction factors at the elevated temperature shown in Figure 4-24 were used to define the elastic modulus of the concrete, the stress-strain curves in compression, and stress-strain curves in tension. The corresponding curves are shown in Figure 4-25, Figure 4-26, and Figure 4-27 respectively.

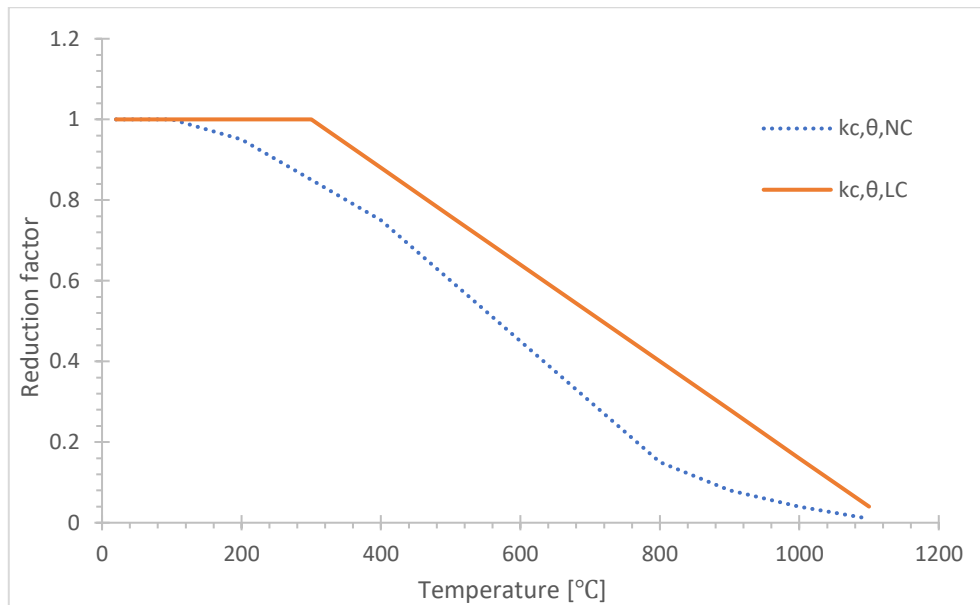


Figure 4-24: Values of two main parameters of the stress-strain relationships of normal weight concrete (NC) and lightweight concrete (LC) at elevated temperatures [35]

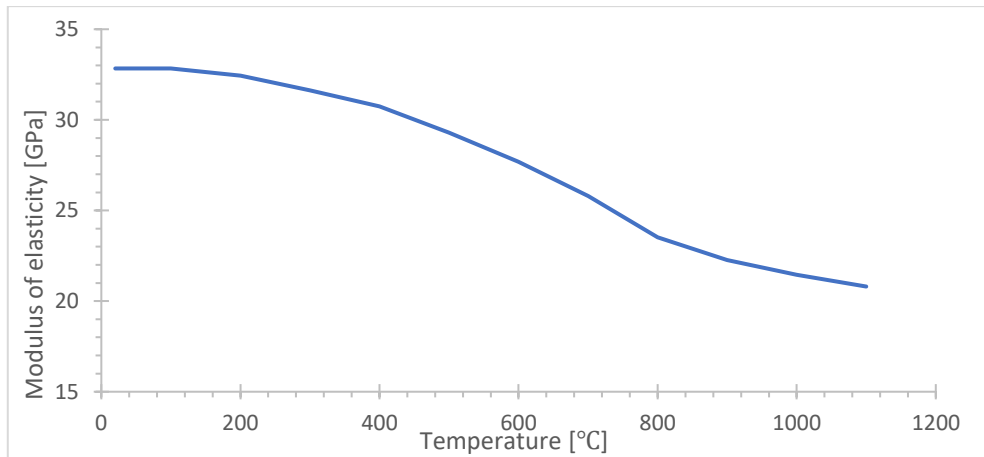


Figure 4-25: Modulus of elasticity as a function of temperature [35]

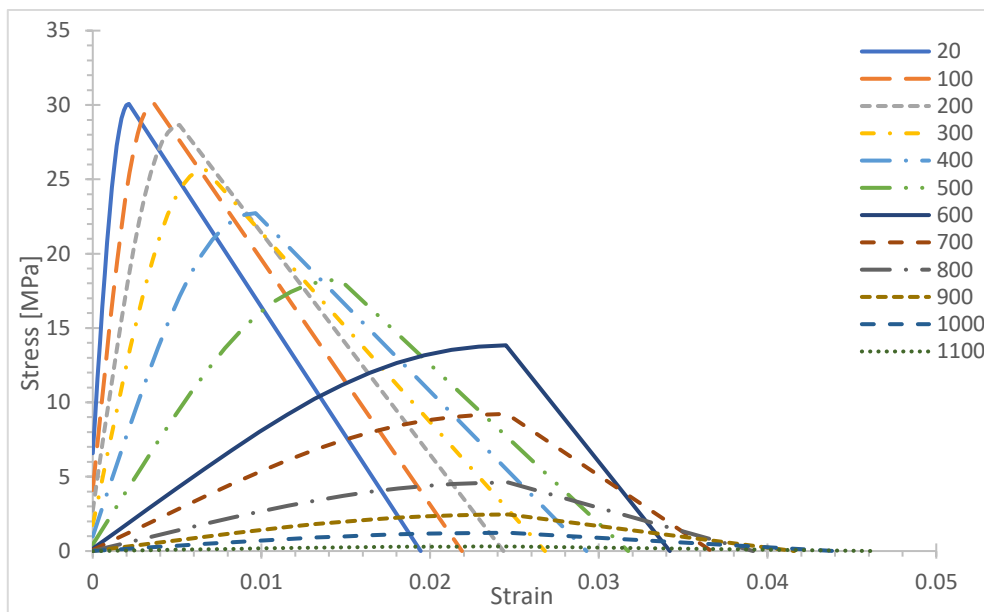


Figure 4-26: Stress-strain curves for compression in concrete at different temperatures [35]

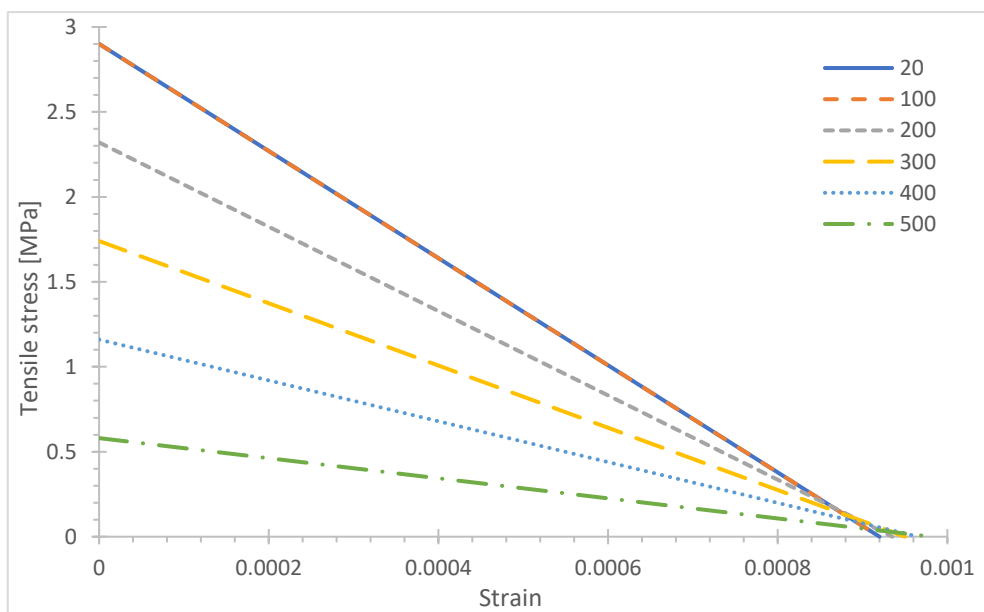


Figure 4-27: Stress-strain curves for tension in C30 at elevated temperatures [33]

4.3.2.7 Thermal elongation C30 concrete

EN1992-1-2 [2004] recommends the following formula for siliceous concrete. This relationship between thermal elongation and temperature is nonlinear up to 700°C, where it becomes constant. The thermal elongation based on equations is shown graphically in Figure 4-28.

$$\Delta l/l = -1.8 \cdot 10^{-4} + 9 \cdot 10^{-6} \cdot \theta + 2.3 \cdot 10^{-11} \cdot \theta^3 \rightarrow 20^\circ\text{C} \leq \theta < 700^\circ\text{C}$$

Equation 20

$$\Delta l/l = 14 \cdot 10^{-3} \rightarrow 700^\circ\text{C} \leq \theta < 1200^\circ\text{C}$$

Equation 21

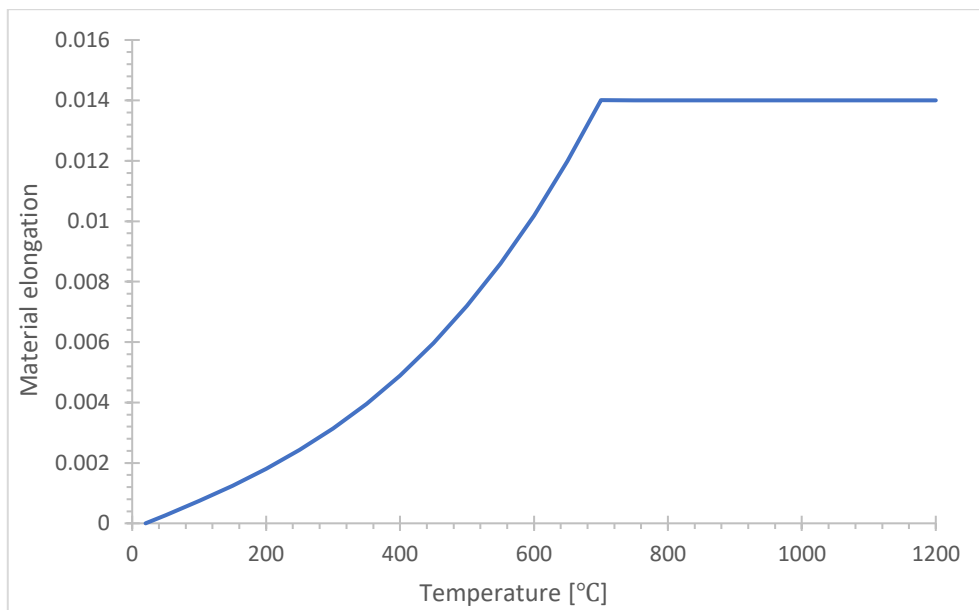


Figure 4-28: thermal elongation of concrete as a function of the temperature according to EN1992-1-2 [2004]

4.4 Validation of FE models

4.4.1 Validation of thermal analysis models

The developed finite element model is validated by comparing predicted temperatures at selected nodes from the analysis with the results measured at the same locations in the fire test. Figure 4-29 shows the thermocouples that were installed on the specimen to capture the temperature histories during the test by red dots. Dashed red lines represent the path that was used to extract the temperature output from the FE model.

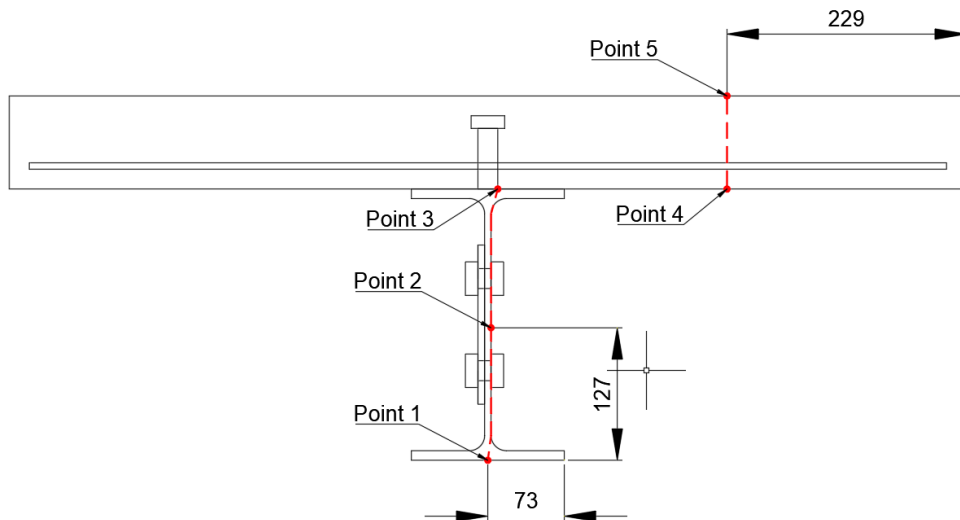


Figure 4-29: Thermocouple instrumentation layout

4.4.1.1 Validation of thermal model Case 1

The temperature profile for the cross-section when the underside of the beam bottom flange reached 600°C is shown in Figure 4-30. The trend was quite similar to the measured values during the test except for the web since the web was exposed to fire from both sides and has a thinner thickness. The values captured from the ABAQUS FE model were quite high compared with the test results. The temperature at points 1...4 was quite the same. The FE trend between these points shows a smoother transition between the temperature than the test results.

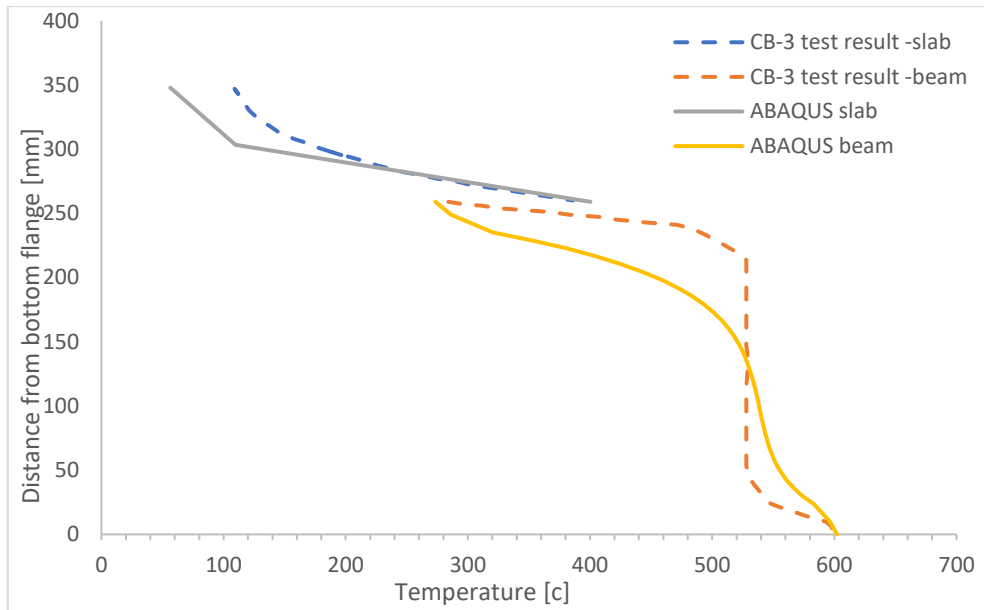


Figure 4-30: Temperature verification for composite beam Test CB-3 with Case 1 results

Temperature histories between measured results and Abaqus results of the cross-section were also compared. The developed temperature in the undersurface of the bottom flange, web surface, and undersurface of concrete were quite similar to the test results as shown in Figure 4-31, Figure 4-32, and Figure 4-33 respectively. It can be noticed that the temperature from the FE model is lower than the measured results during the heating phase. The deviations between the two results during the heating stage were because of the different heating methods used. In the test, the beam was heated with the fibre ceramic heater with radiative heat flux. In the FE analysis, the beam was heated with convective and radiative heat flux. The heating conditions during the tests were not fully simulated.

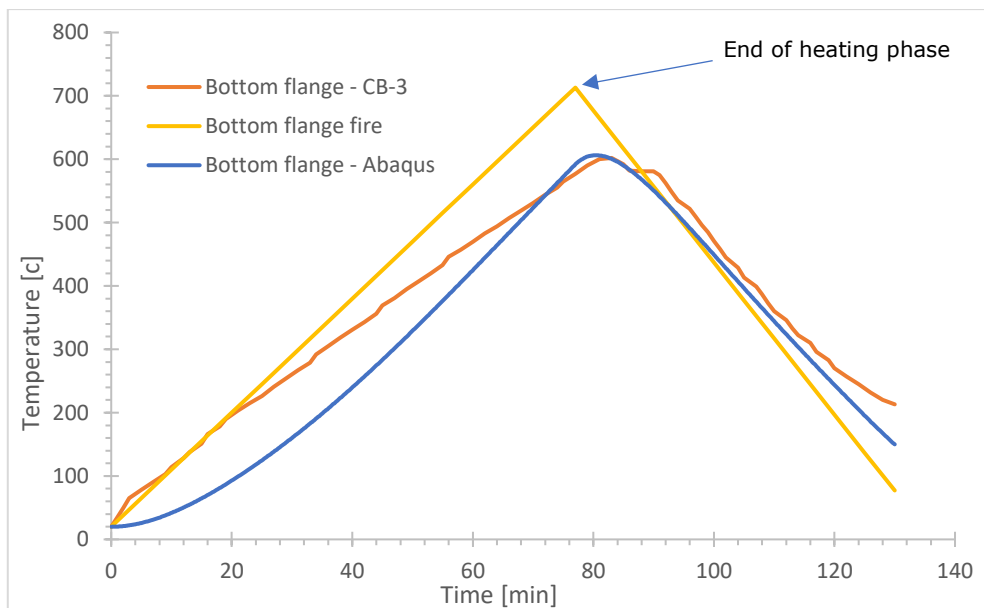


Figure 4-31: Bottom flange temperature history Case 1

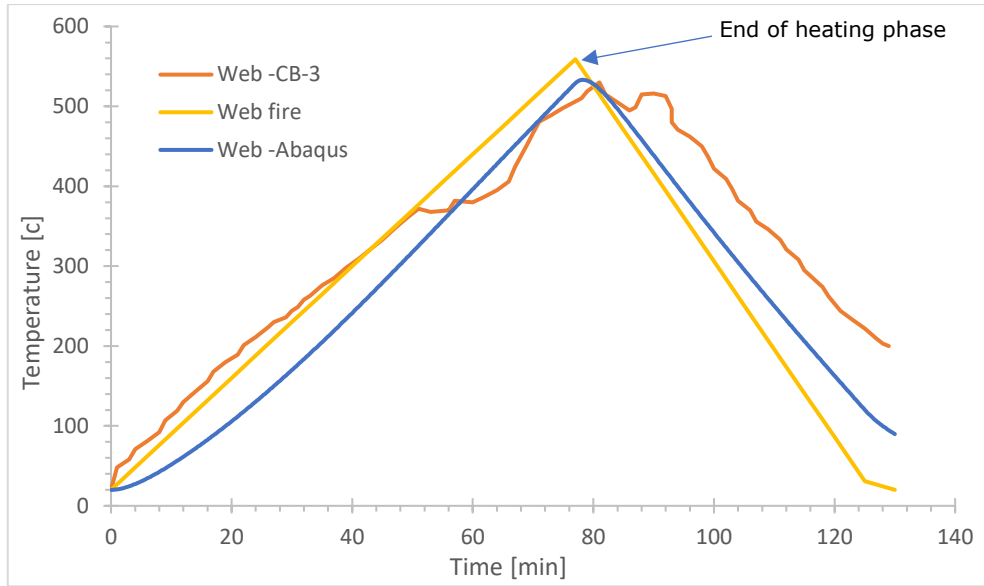


Figure 4-32: Web temperature history Case 1

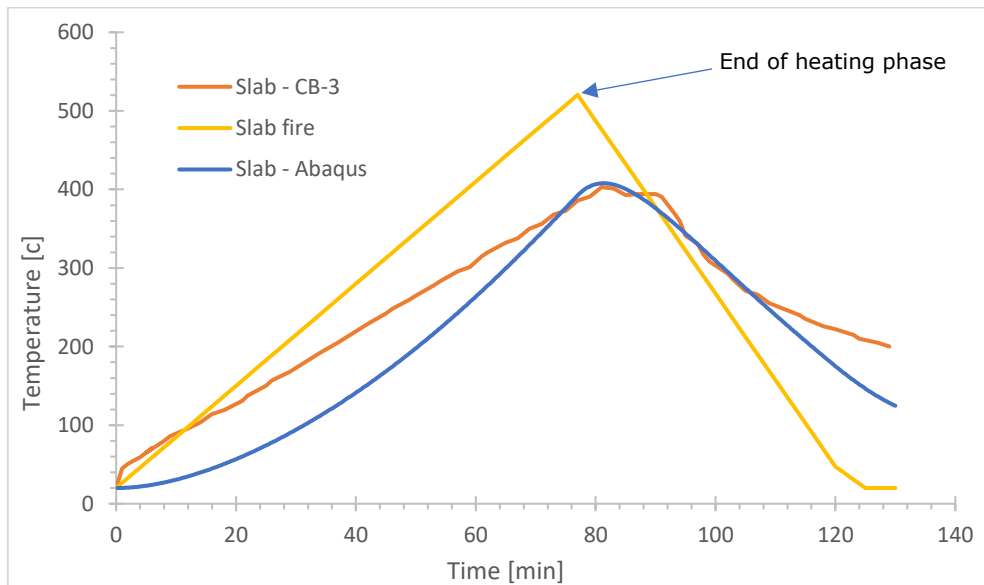


Figure 4-33: Bottom slab temperature history Case 1

Figure 4-34 shows the contour of temperature distribution of the cross-section when the bottom flange reached the maximum temperature after 80 minutes exposed to fire. Figure 4-35 shows the contour of temperature distribution of the cross-section when at the end of the cooling stage after 130 minutes.

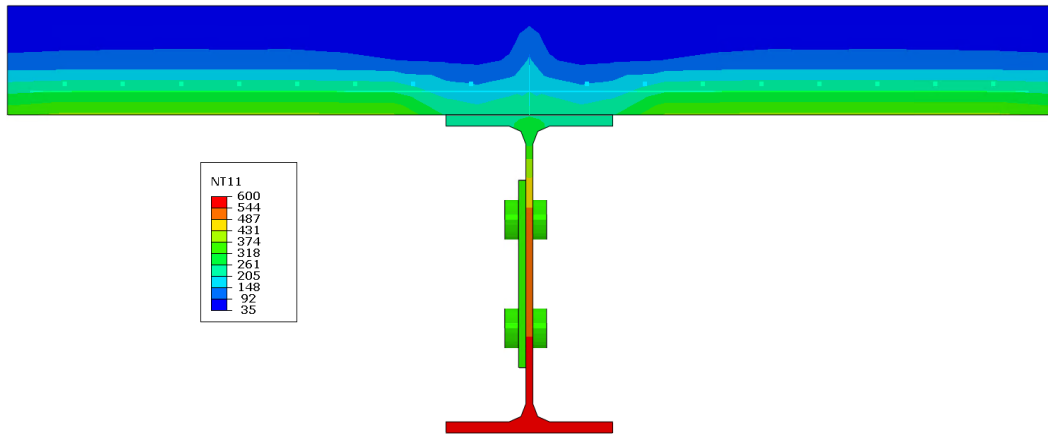


Figure 4-34: Cross-section temperature profile at the end of heating phase Case 1

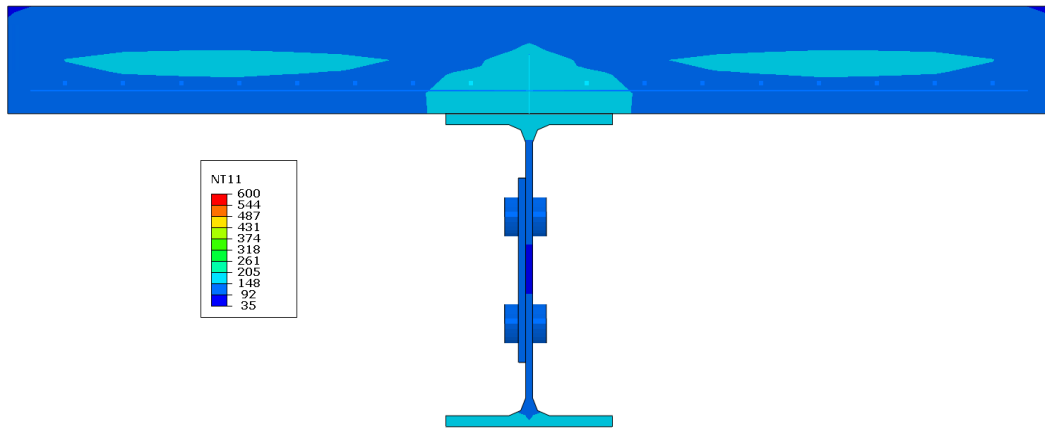


Figure 4-35: Cross-section temperature profile at the end of cooling phase Case 1

4.4.1.2 Validation of thermal model Case 2

The FE model was validated further by using the histories of the surface temperatures measured during the test as input. The surface temperatures presented in Figure 4-32, and Figure 4-33 were defined as the surface temperatures for the bottom flange, the web, and the exposed side of the concrete slab respectively. The unexposed side of the concrete and the top flange was defined with the initial air temperature of 20°C.

Figure 4-36 shows the temperature profile that was measured when the undersurface of the bottom flange reached 600°C. It can be seen that the FE results matched the test results well. The most noticeable difference was the temperature of the top surface of the top flange, the temperature at the test was 285°C while in the FE model was 445°C. That difference might increase the average temperature for the beam which might decrease the beam strength. Figure 4-37 and Figure 4-38 show temperature distribution along the cross-section when the heating phase ended and the cooling phase ended respectively.

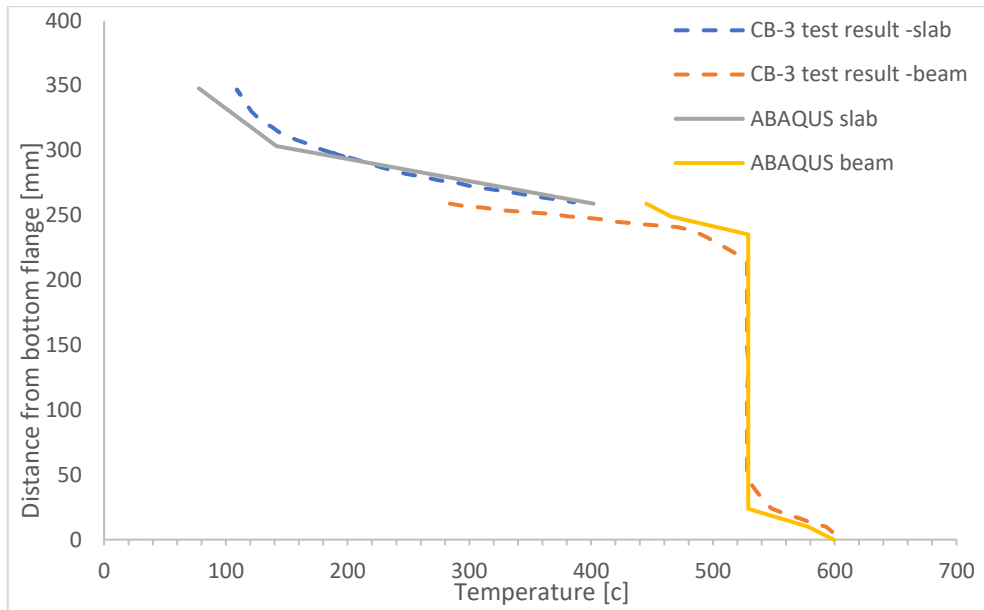


Figure 4-36: Temperature verification for composite beam Test CB-3 with Case 2 results

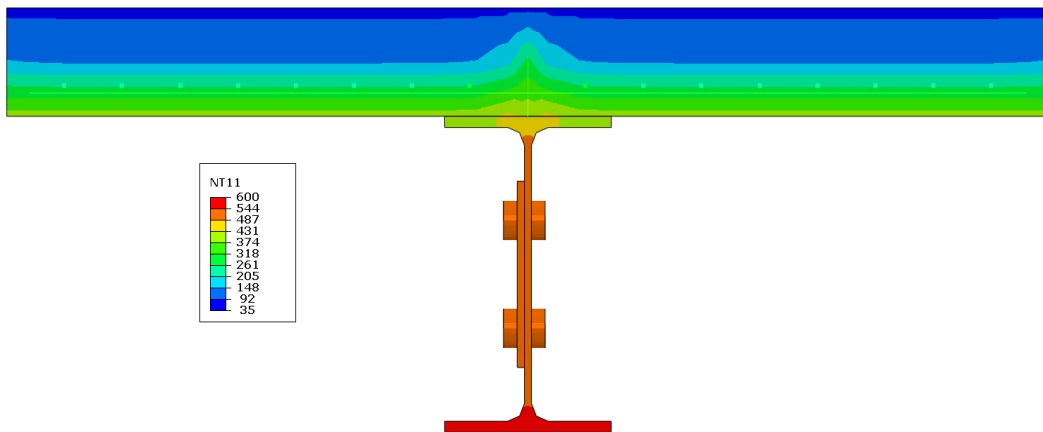


Figure 4-37: Temperature profile at the end of heating phase Case 2

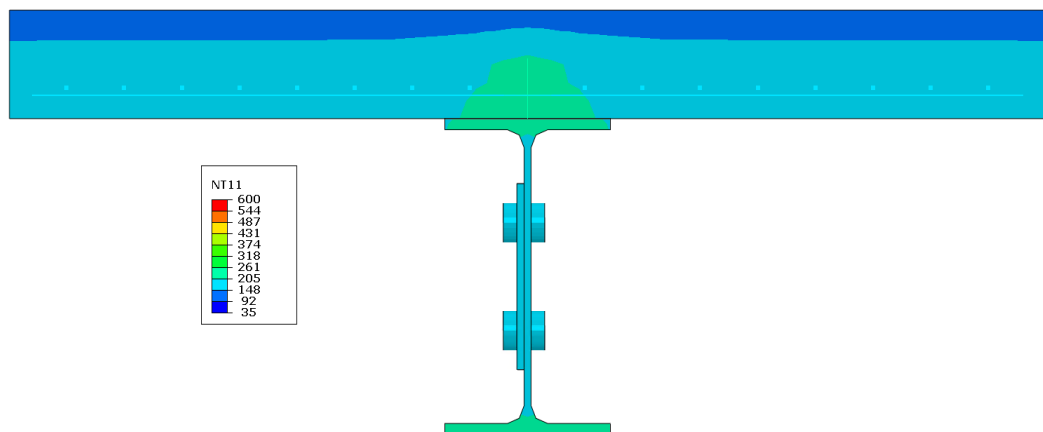


Figure 4-38: Temperature profile at the end of cooling phase Case 2

4.4.1.3 Validation of thermal model Case 3

The FE models were improved especially for reducing the top flange temperature. The measured temperature profile when the undersurface of the bottom flange reached 600°C is shown in Figure 4-39. The FE results matched with test results very well. Figure 4-40 and Figure 4-41 show temperature distribution along the cross-section when the heating phase ended and the cooling phase ended respectively. With these results, the thermal models were validated by the test results and will be used further for validating the mechanical analyses model.

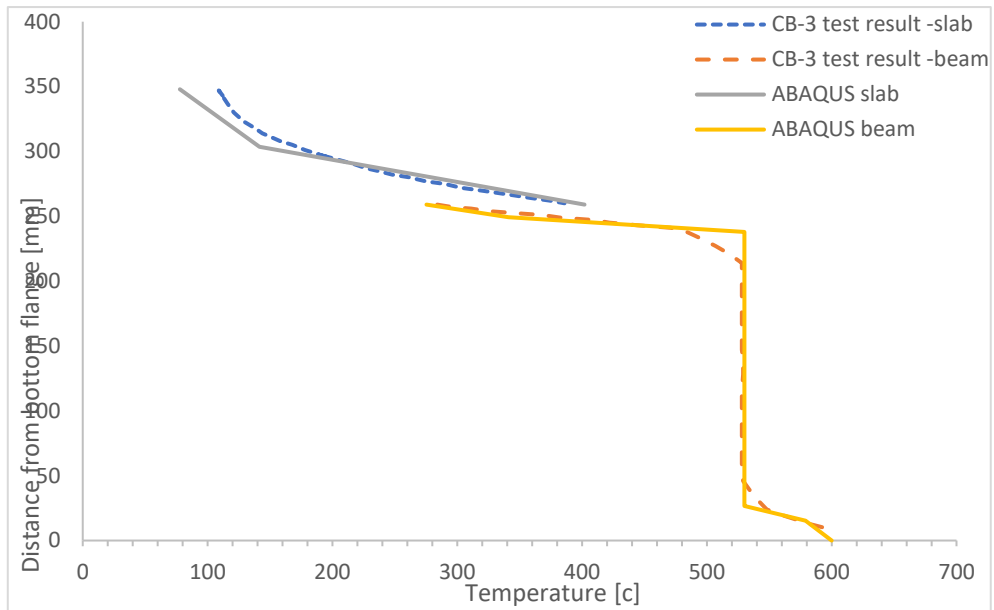


Figure 4-39: Temperature verification for composite beam Test CB-3 with Case 3 results

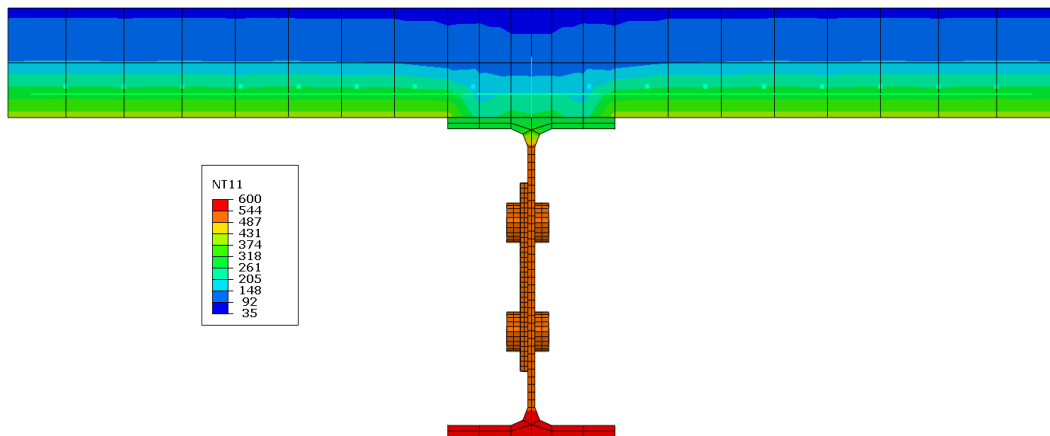


Figure 4-40: Temperature profile at the end of heating phase Case 3

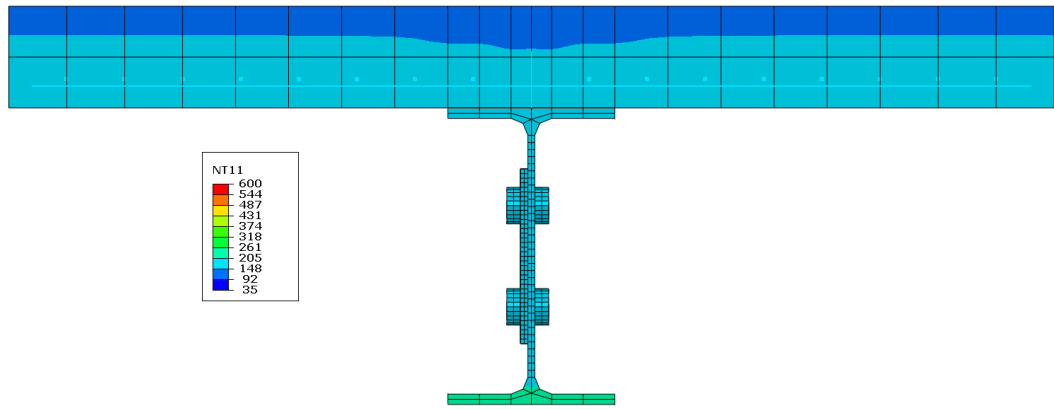


Figure 4-41: Temperature profile at the end of cooling phase Case 3

4.4.2 Validation of mechanical analysis models

The developed finite element model is validated by comparing predicted response parameters from the analysis with the results measured in the fire test. The validation process covered mechanical response parameters, i.e., the vertical displacement at mid-span and quarter points. The temperature histories for Case 1 and 2 results were used in mechanical analyses. Case 1 presents the more realistic heating conditions as the beam is exposed to fire. Case 2 was selected because of the close temperature history to the test results.

4.4.2.1 Validation of mechanical model Case 1

Figure 4-42 shows a comparison between the midspan displacement of the test and the FE model. The trend of the two results was similar. The displacement after the loading phase at room temperature of 20°C were 9.1 mm and 8.4 mm for the test and FE model, respectively. When the bottom surface of the bottom flange was 600°C the midspan displacement exceeded 74 mm for the test specimen and 79.6 mm for the FE model. The deflections received from the cooling stage matched well with the test results in the same stage. However, the derivations of the deflections between the two results during the heating stage were observed. The derivations were due to the different temperature fields developed in the heating stage as shown in Figure 4-30.

Figure 4-43 shows a comparison of the quarter-point displacement at 0.95 m away from the beam end between test results and the FE model. The trend was similar, the displacement after the loading phase at room temperature of 20°C were 6.8 mm and 6 mm for the test and FE model respectively. When the bottom surface of the bottom flange was 600°C the quarter-point displacement exceeded 55 mm for the test specimen and 53 mm for the FE model. These results indicate reasonable agreement between the experimental data and the FEM model results. Unlike the deviation of deflection at mid-span at the heating stage, the deviation of the deflection at the quarter-point was spread in both heating and cooling stages. The spreading of deviations indicated the beam in the tests was heated non-uniformly along the span.

4.4.2.2 Validation of mechanical model Case 2

As shown in Figure 4-42, the maximum midspan point deflection was close to the deflection value from the model where the heat flux method was used. Forcing the temperature along the whole web of the beam to be equal resulted that the top flange being heated quicker. As shown in Figure 4-37 and Figure 4-34, the average temperature in the top flange was cooler when the heat flux was used as input in the thermal analysis model. The deflection value, when the bottom flange was 600°C, was 80.7 mm. however, the quarter-point displacement was the same as the value from the heat flux model 53 mm.

Both Cases showed similar results to the test results. With these results, the mechanical models are validated and will be further used to study the load-bearing mechanism in the composite beam.

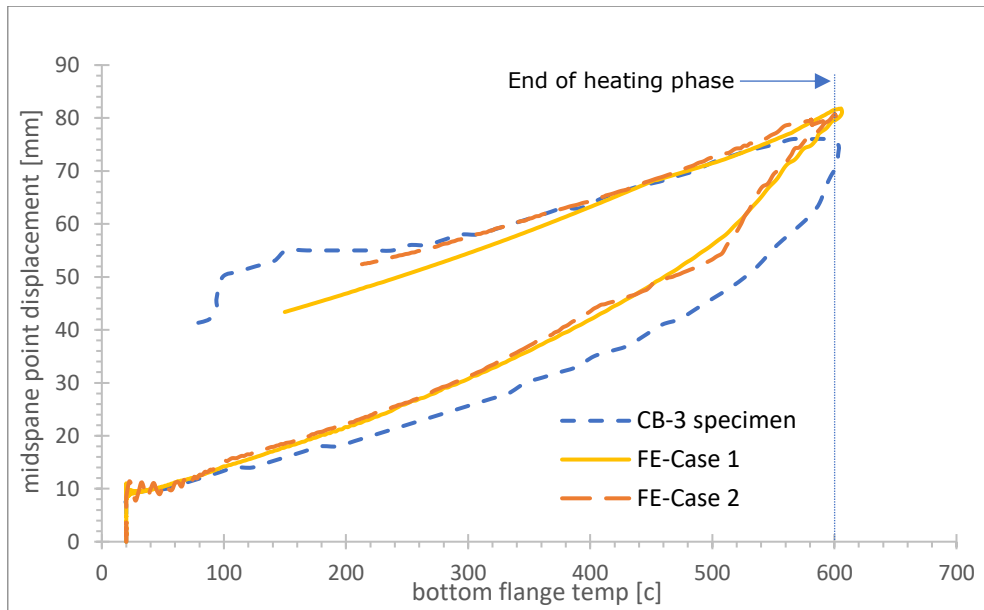


Figure 4-42: Midspan displacement versus average bottom flange temperature

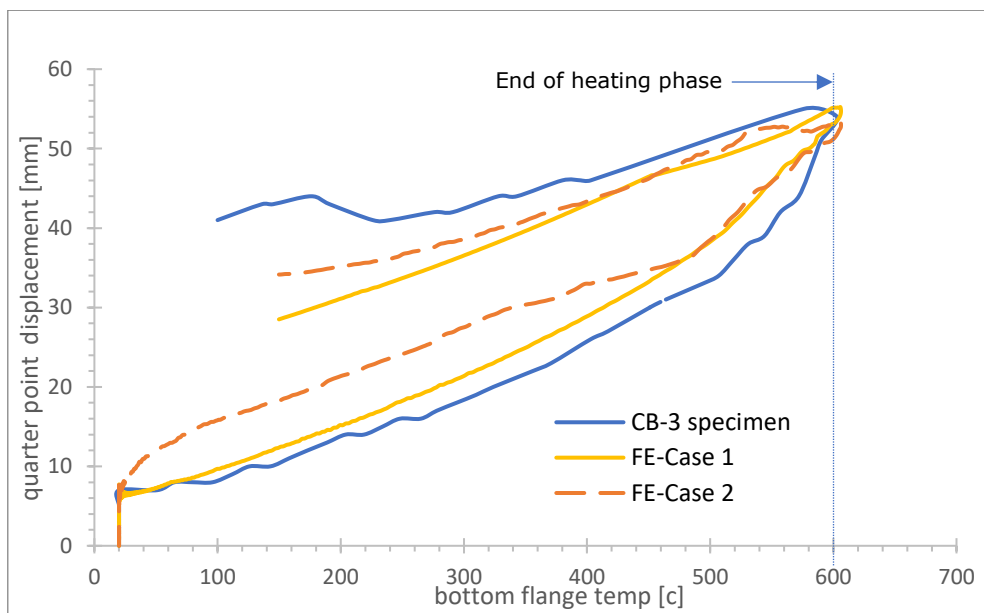


Figure 4-43: Quarter-point displacement versus average bottom flange temperature

4.5 Load-bearing mechanism of composite beam

4.5.1 Four-stage mechanism based on Case 1

Figure 4-44 represents the axial forces output in the connection from FE analyse during the mechanical loading phase for 30 sec followed by heating and cooling phases for 130 minutes compared with the benchmark test results. The positive values present compressive axial forces and negative values represent tensile axial force. Figure 4-45 represents the vertical deflection of the midspan and quarter point. The behaviour of the composite beam was quite similar to the behaviour of the steel beam exposed to fire. The maximum principal stresses after the mechanical loads are applied are shown in Figure 4-49 for both Case 1 and Case 2.

Based on the axial force developed, the load-bearing mechanism of the composite beam during the heating and cooling stages is similarly divided into four stages:

- Stage I (0-1): development of compression forces due to the restrained thermal expansion until the material degradation starts. When the temperature rose, the beam started to expand. Due to the beam end being restrained, the axial compression force increased. There was a small increase in the deflection to 14 mm which happened at 21 minutes when the bottom flange temperature was about 100°C at point (1). The stresses at point (1) are shown in Figure 4-50.
- Stage II (1-3): as the temperature elevated, the material started to degrade and the bending of the beam took control until a hinge behaviour. The vertical deflection increased faster till the average temperature of the bottom flange was around 560°C at almost 74 minutes and the deflection was about 75 mm at point (3). Point (2) represents the max compressive force of 207 kN in the connection at 335°C at 42 minutes. The stresses at point (2) are shown in Figure 4-51. At the connection, the axial force did not exceed the connection strength associated with the shear failure of the bolt. The compression axial force started to decrease slowly just before point 3 is reached. The stresses at point (3) are shown in Figure 4-52.
- Stage III (3-4): sudden decrease of the axial compression forces to zero. At point 3, it was noticeable that the beam was about to run away if the temperature kept increasing. The large deformation activated the axial tension force developed inside the beam, thus accelerating the development of tension forces. However, the cooling phase started and the beam regained some strength. The restrained thermal contraction created axial tension forces. The fast cooling rate of the beam accelerated the decrease of the axial force. The stresses at the heating phase end are shown in Figure 4-53. The beam was partially in tension till it reached the point (4). The stresses at point (4) are shown in Figure 4-54
- Stage IV (4-5): development of axial tension forces inside the beam. At point (4) the axial force became completely in tension due to the restrained thermal contraction at 105 minutes with a temperature of 400°C and the vertical deflection was 63 mm. The controlled cooling forced the beam to convert from compression to tension. The stresses at point (5) are shown in Figure 4-55.

The 5 points on the curve of axial force versus time correlate well with the points marked on the curve of deflection versus time as shown in Figure 4-45. The material degradation and hinge mechanism accelerated the deflection at point 1 and point

3, respectively. During the cooling stage, both the developed tension force and the material retention recover the deflection. However, the residual deflections are large when the cooling stages stopped.

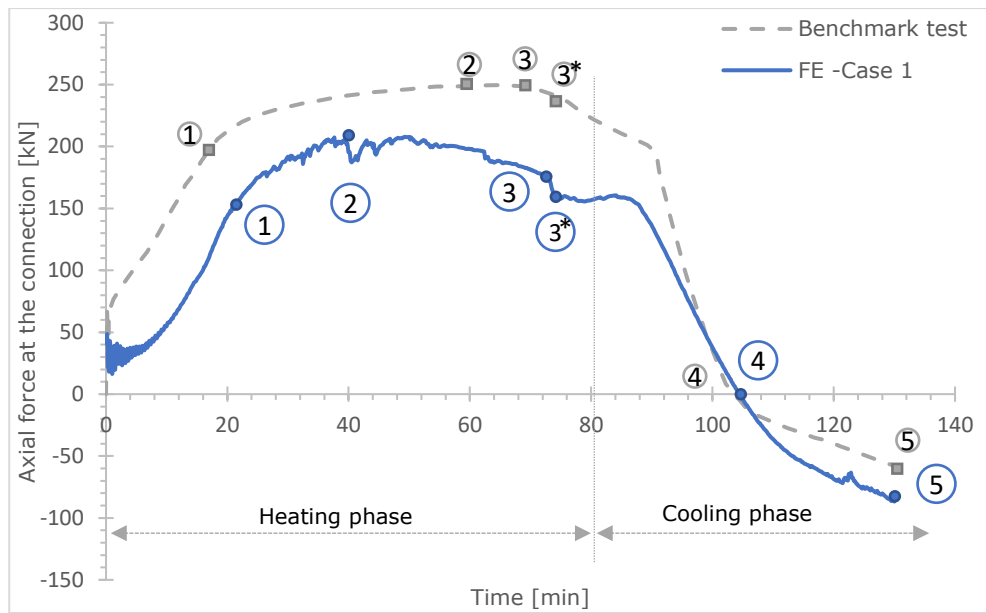


Figure 4-44: Axial force in the connection as a function of time in case 1

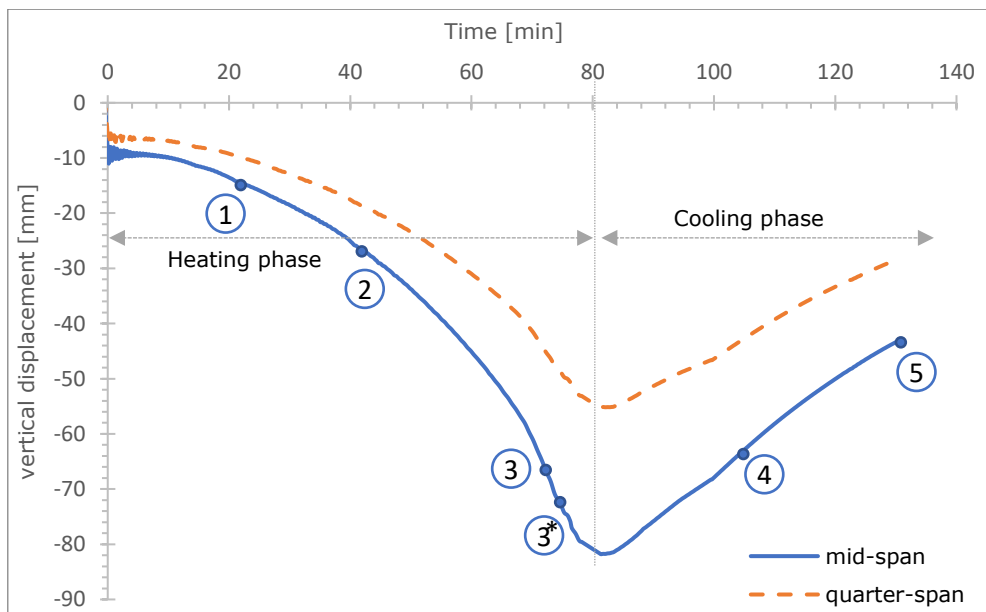


Figure 4-45: Vertical displacement of the beam as a function of time in case 1

4.5.2 Four-stage mechanism: Case 2

Figure 4-46 shows the axial forces developed in the composite beam studies in Case 2. The positive values present compressive axial forces and the negative values present the tension axial force.

Based on the axial force developed, the load-bearing mechanism of the composite beam in Case 2 is compared to that of the composite beam in Case 1 in terms of four stages:

- Stage I (0-1): the axial force developed in Case 2 is more close to the values taken from the literature than the axial force developed in Case 1. The closeness is due to the higher temperatures at the web and the bottom flange of the steel beam predicted by inputting the surface temperature in Case 2. These higher temperatures also increased the axial compression load and early activated the material degradation at point (1). The stresses at point (1) are shown in Figure 4-50.
- Stage II (1-3): As for the trend of the axial force developed in this stage, Case 1 is more close to the literature value than Case 2 is. The axial forces in Case 2 reached the maximum earlier and reduced more than those in Case 1. Figure 4-36 showed that, at this stage, the temperature of the top flange of the steel beam reached around 400°C, which was about 200°C higher than that reported in the test. Similarly, Figure 4-30 showed that the temperatures of the top flange of the steel beam in Case 1 were similar to the test values. The observations indicate the response of the composite beam is mainly controlled by material degradation of the top flange of the steel beam and the interactions between the steel beam and concrete slab. The stresses at point (3) are shown in Figure 4-52.
- Stage III (3-4): In this stage, due to the similar trend of the temperature development, the beam in Case 1 behaved similarly to the tested beam. However, due to the higher temperature developed in the top flange in Case 2, the axial force in the same beam dropped dramatically and took a longer time to reach the local peak value after the cooling stage started. Figure 4-16 and Figure 4-26 showed that the strength of both the shear connector and strength of concrete in compression degraded heavily between 400°C and 500°C, similarly to the strength of structural steel. Therefore, the response of the composite beam is controlled mainly by the interactions between the steel beam and concrete. The stresses at the heating phase end are shown in Figure 4-53.
- Stage IV (4-5): In this stage, the composite beam in Case 1 and Case 2 behaved similarly to the tested beam. The similarity of the behaviour is due to the similar temperature fields developed in the steel beams during the cooling stages. The stresses at point (5) are shown in Figure 4-55.

Figure 4-47 and Figure 4-48 represent the vertical displacement for mid-span and quarter-span respectively for Case 1 and 2. During the heating phase, Case 2 displacement was higher than Case 1 since Case 2 heated faster. At point (3), the temperature matched for both models. Therefore the deflection became similar. The vertical displacement at mid-span when the heating phase end was 81 mm and 80 mm for Case 1 and 2 respectively. The same behaviour occurred at quarter-span displacement. The vertical displacement at quarter-span when the heating phase end was 55 mm and 53 mm for Case 1 and 2 respectively. After the heating phase

ended, the displacement was reduced because the beam contracted and regain some strength.

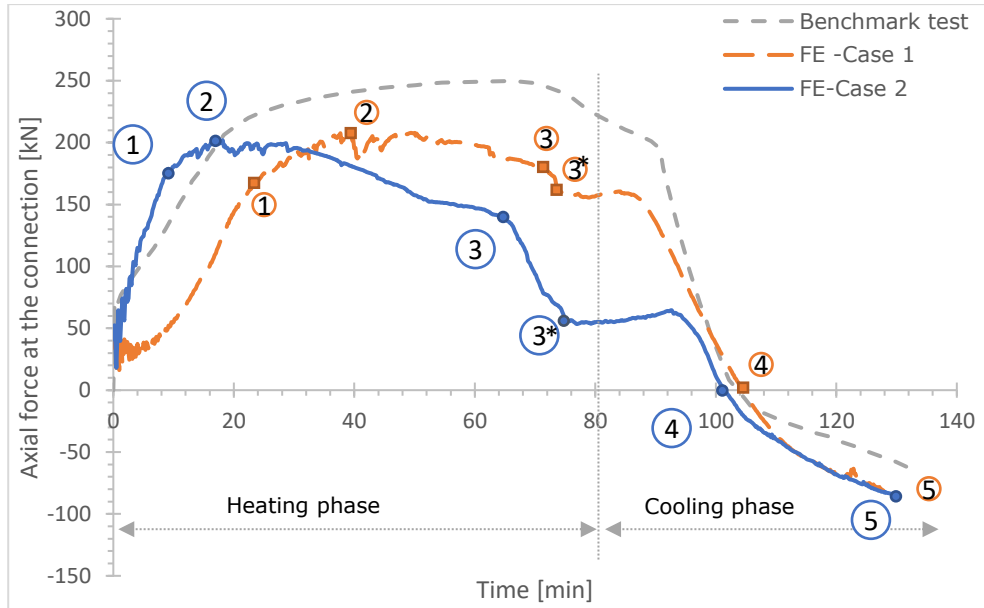


Figure 4-46: Axial force in the connection as a function of time in case 2

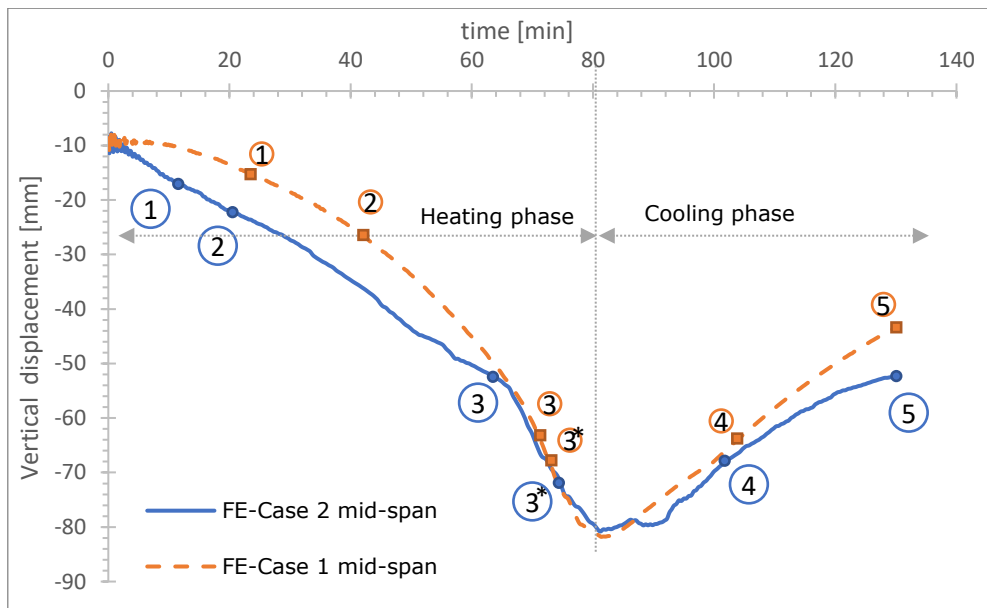


Figure 4-47: Vertical mid-span displacement of the beam as a function of time in case 2

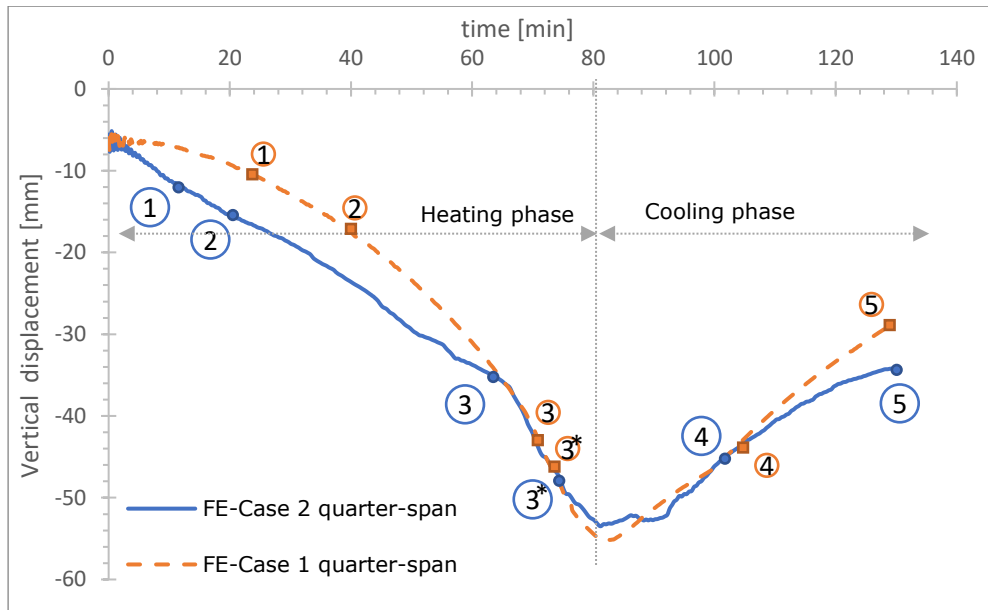


Figure 4-48: Vertical quarter-span displacement of the beam as a function of time in case 2

Figure 4-49 till Figure 4-55 show the absolute max principle stresses with deflection along with the FE model for both the heat flux model (Case 1) and surface temperature model (Case 2) at different stages. Principal stress represents the normal stress acting onto the principal plane that has zero shear stress. Stresses along the beam did not exceed the yielding point except for the connection region.

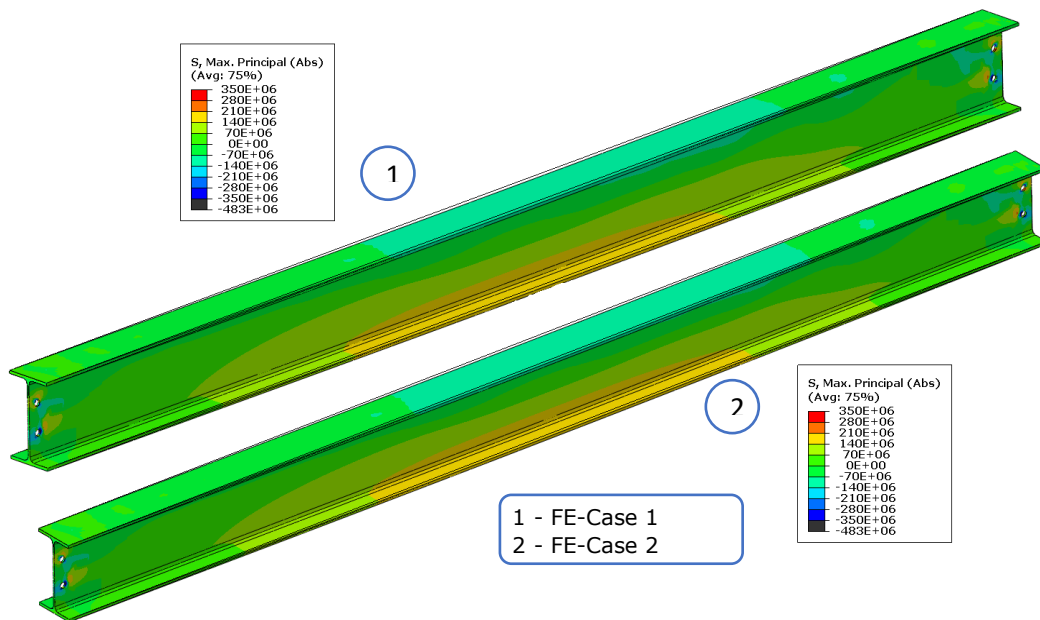


Figure 4-49: Beam stresses after loading step

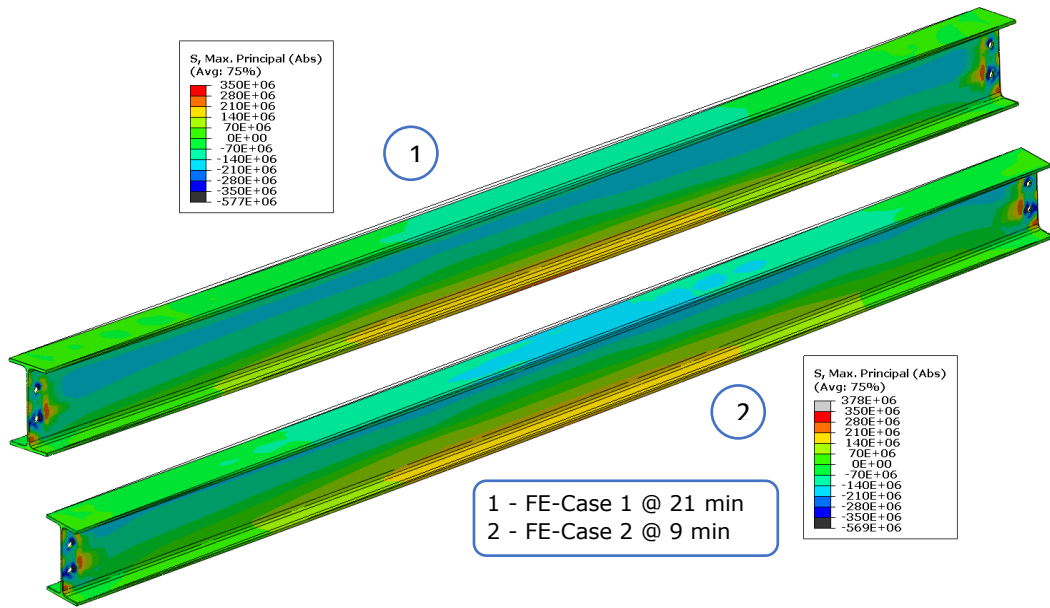


Figure 4-50: Beam stresses before material degradation

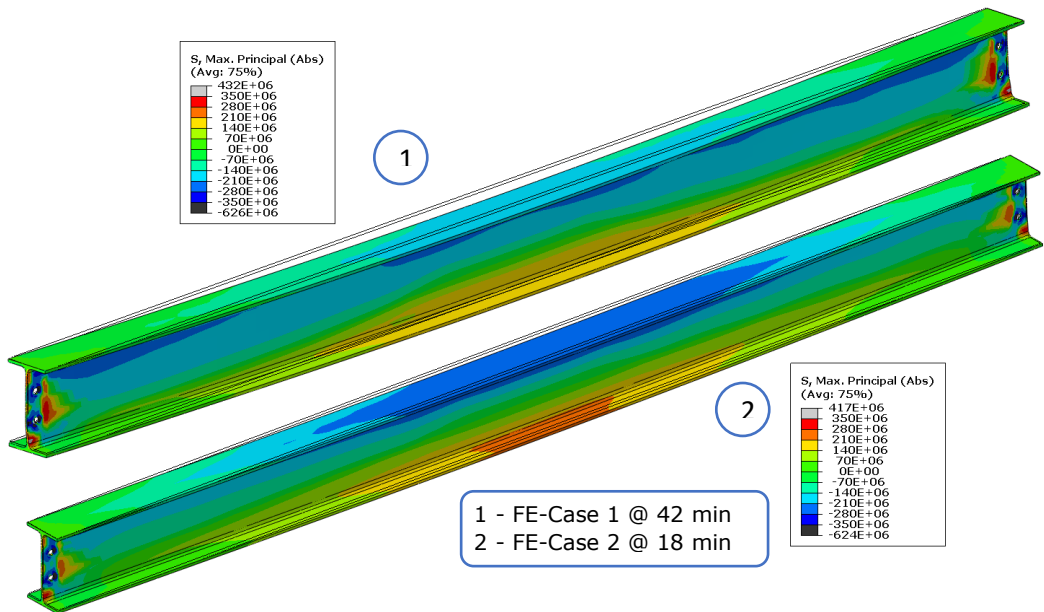


Figure 4-51: Beam stresses maximum compressive force

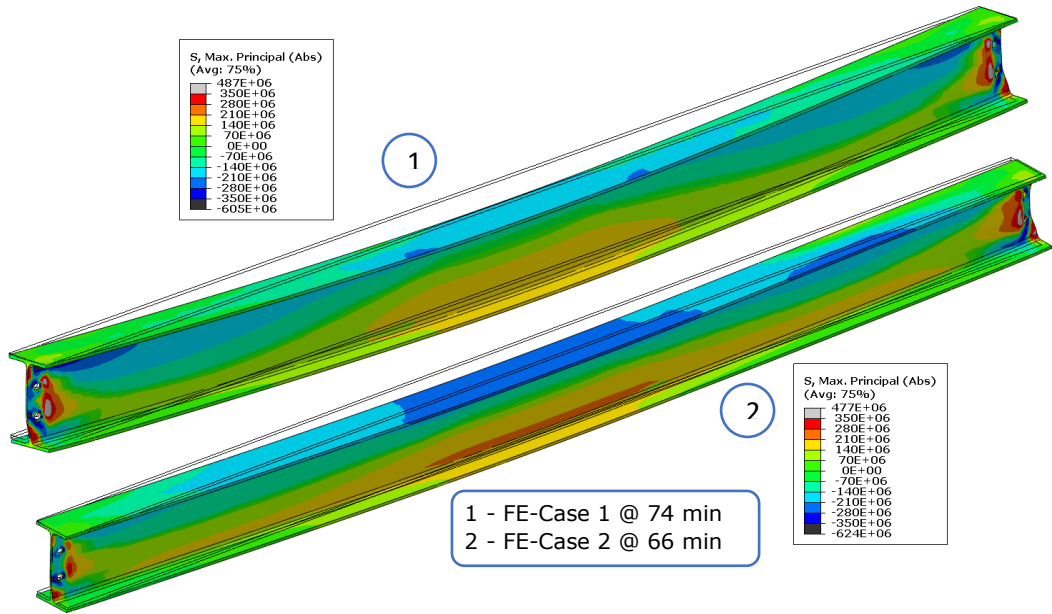


Figure 4-52: Beam stresses before runaway behaviour

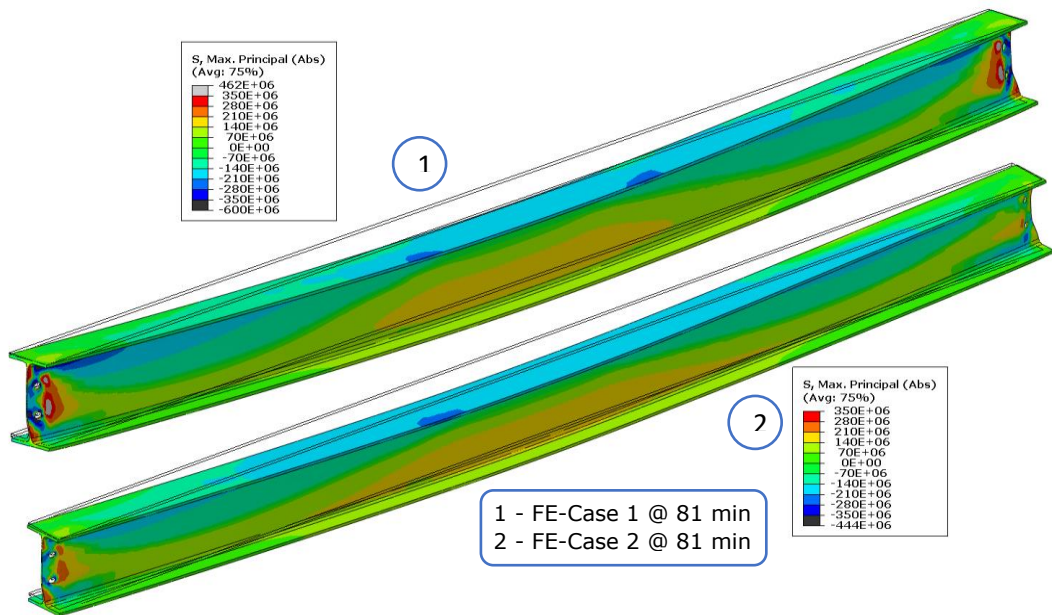


Figure 4-53: Beam stresses after the heating phase

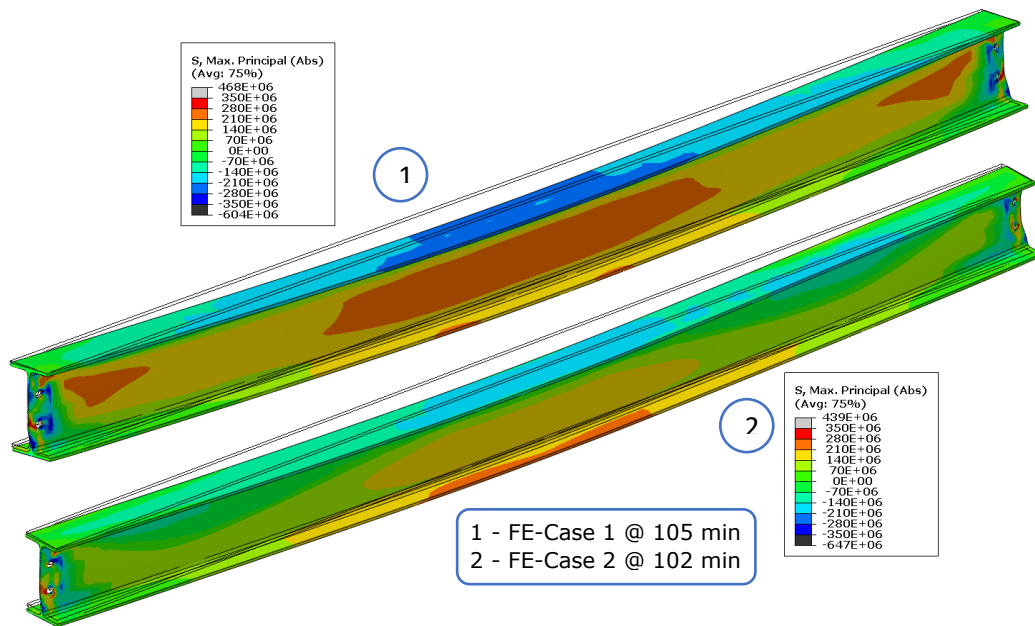


Figure 4-54: Beam stresses at zero axial force

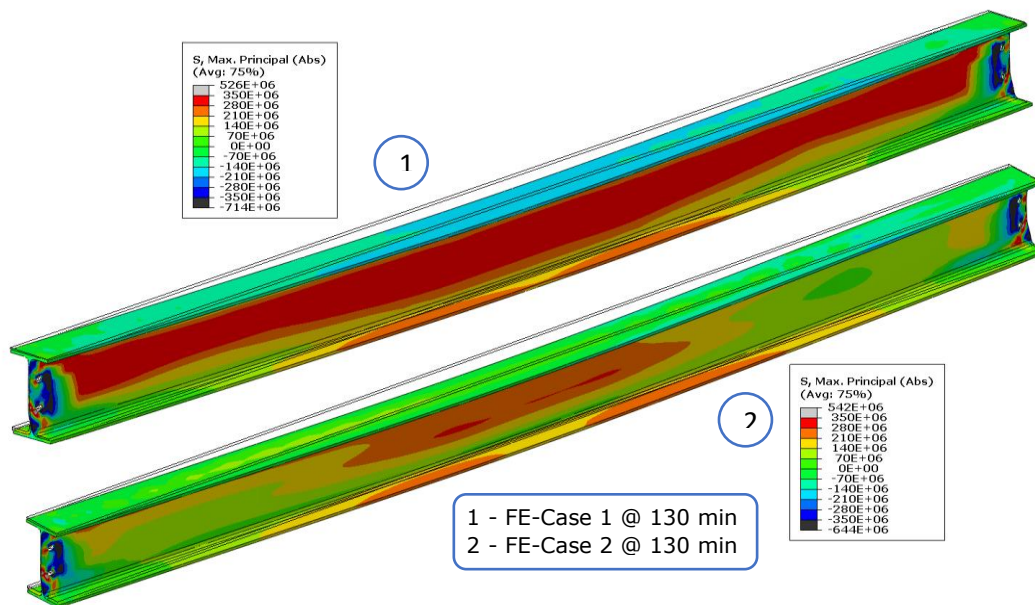


Figure 4-55: Beam stresses after cooling phase

4.6 Effect of load ratio on the behaviour of the composite beam

4.6.1 Response of composite beam with smaller load: Case 4

4.6.1.1 Model description

To study the load ratio on the behaviour of the composite beam, the validated FE model was used to simulate specimen CB-4 exposed to the same heating and cooling conditions as in specimen CB-3 but under the load of 111 kN. In the FE models, the load was applied within a time frame of 30 sec. The same heating and cooling protocol was used at 7°C/min for the underside of the bottom flange and the web, and 4°C/min for the underside of the concrete slab and the cooling rate was 12°C/min. The target temperature was that the undersurface of the bottom flange reached 700°C for a total time of 150 minutes for the heating and cooling phases. The heating phase was 100 minutes and the cooling phase was 50 minutes. These rates were adjusted to simulate the fire condition of the gas furnace test. Different time-temperature curves were defined as amplitude for the bottom flange, web of the beam and underside of the slab as shown in Figure 4-56.

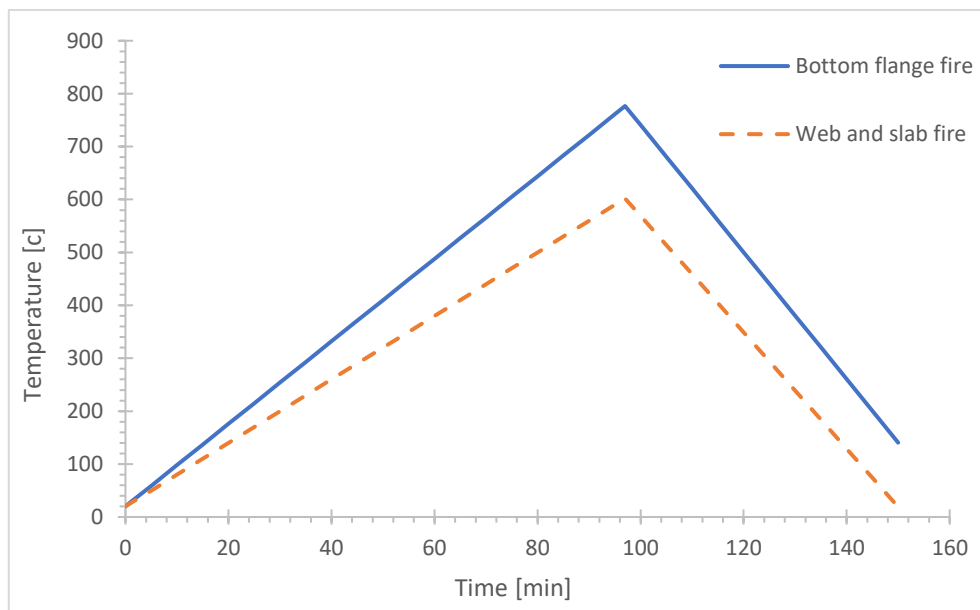


Figure 4-56: Heating and cooling rate for the structure Case 4

4.6.1.2 Thermal analysis results

The temperature histories were presented in Figure 4-57 for the bottom flange, the web of the steel beam and the bottom surface of the concrete slab. The measuring points were presented in Figure 4-29. The temperature developed smoothly along the cross-section. The bottom flange reached 685°C after 100 minutes as shown in Figure 4-58 at the same time the web surface temperature was 579°C and the bottom surface of the concrete slab was 511°C. The temperature distribution at the end of the simulation is shown in Figure 4-59 after 150 minutes.

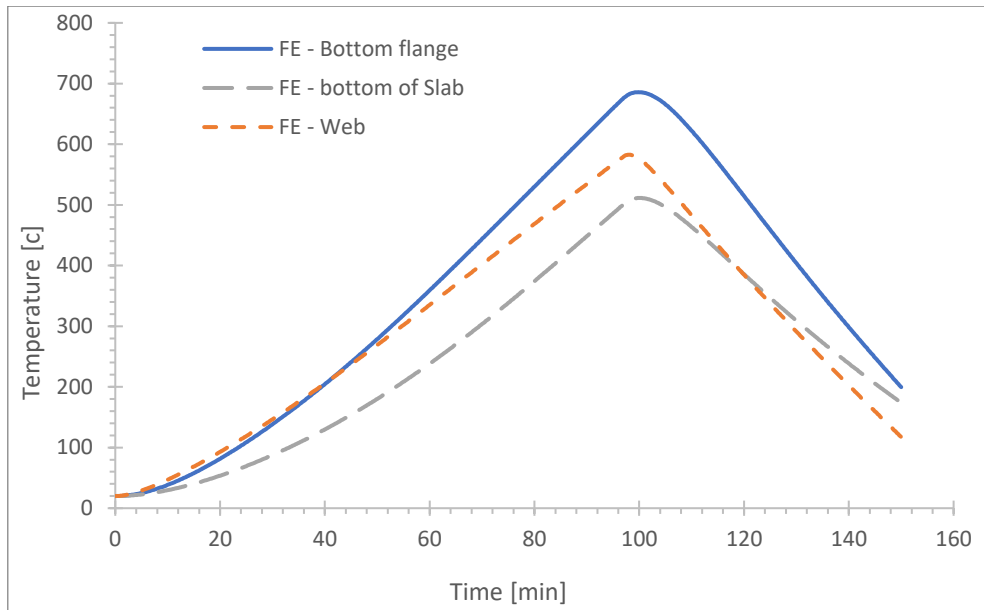


Figure 4-57: Temperature histories of the structure Case 4

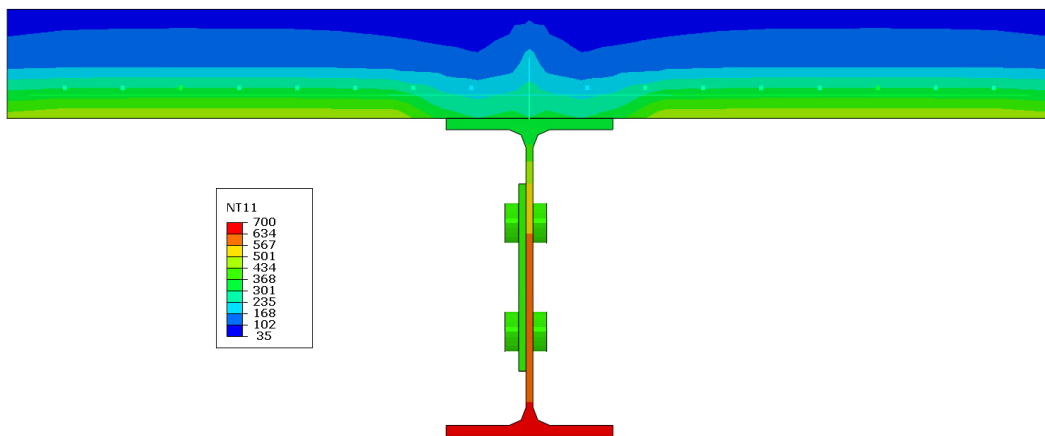


Figure 4-58: Temperature profile at the end of heating phase at 100 minutes Case 4

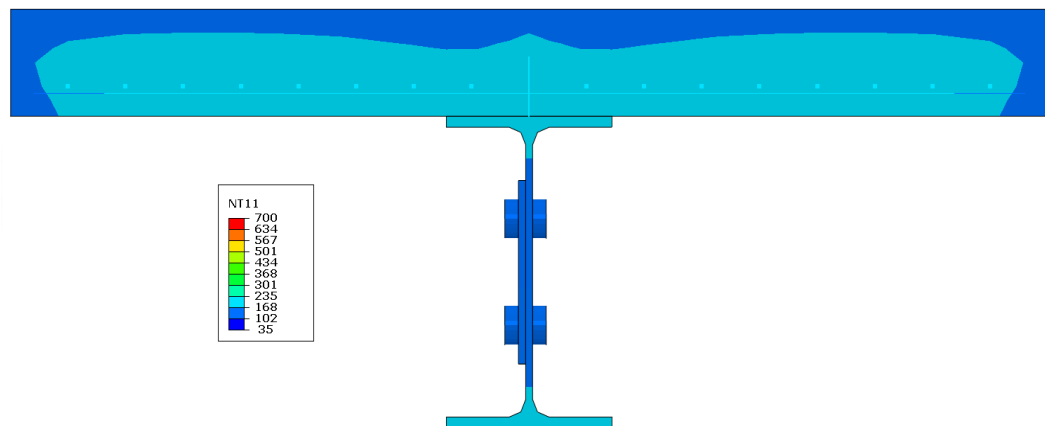


Figure 4-59: Temperature profile at the end of cooling phase at 150 minutes Case 4

4.6.1.3 Mechanical analysis results

The behaviour of the composite beam with a load of 111kN up to 700°C was quite similar to the composite beam behaviour with 156kN up to 600°C. Figure 4-60 represents the axial forces output in the connection from FE analyse during the mechanical loading phase for 30 sec followed by heating and cooling phases for 150 minutes compared with the results of case 1. The positive values present compressive axial forces and negative values represent tensile axial force. Figure 4-61 represents the vertical deflection of the midspan and quarter point.

Figure 4-60 shows that the composite beam loaded with 111 kN followed the four-stage load transferring mechanism, as in the beam loaded with 156 kN. Due to the less load applied, the beam in Case 4 developed the slightly higher compression axial load in Stage 1, reached the slightly maximum load at point 2, delayed the sudden change of axial compression load at point 3 about 20 min later, and delayed the transition of tension to compression about 20 min later.

Figure 4-61 and Figure 4-62 represent the vertical displacement for mid-span and quarter-span respectively for Case 1 and 4. Similar behaviour was noticed during the heating phase as both cases were heated similarly. Due to less applied load in Case 4, the displacement was smaller than in Case 1. Although the beam in Case 4 was heated to 700°C, which indicates that the beam in Case 4 lost more strength than the beam in Case 1. The vertical displacement at mid-span when the heating phase end was 81 mm and 79 mm for Case 1 and 4 respectively. The same behaviour occurred at quarter-span displacement. The vertical displacement at quarter-span when the heating phase end was 55 mm for both cases. After the heating phase ended, the displacement was reduced because the beam contracted and regain some strength.

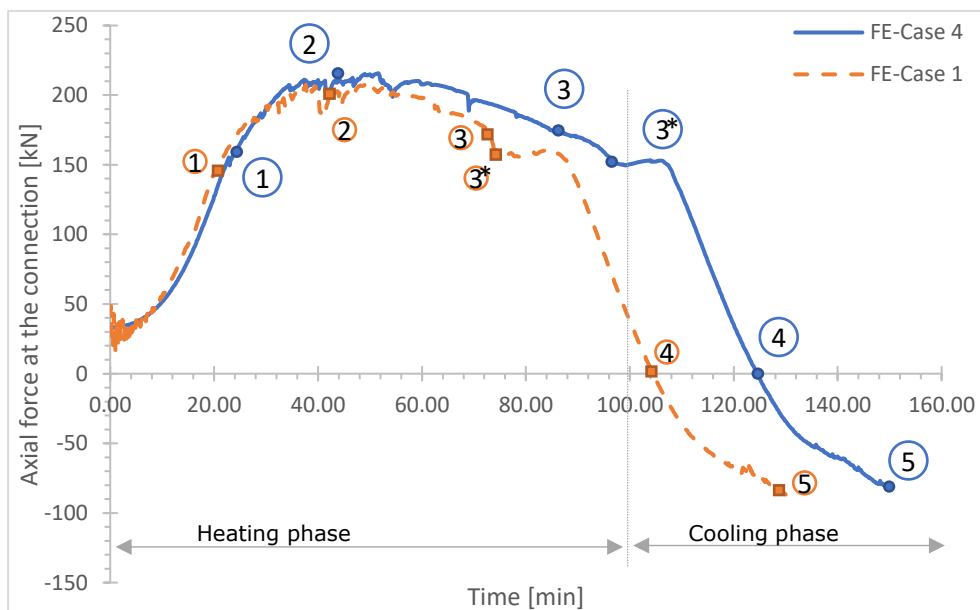


Figure 4-60: Axial force at the connection as a function of time in case 4

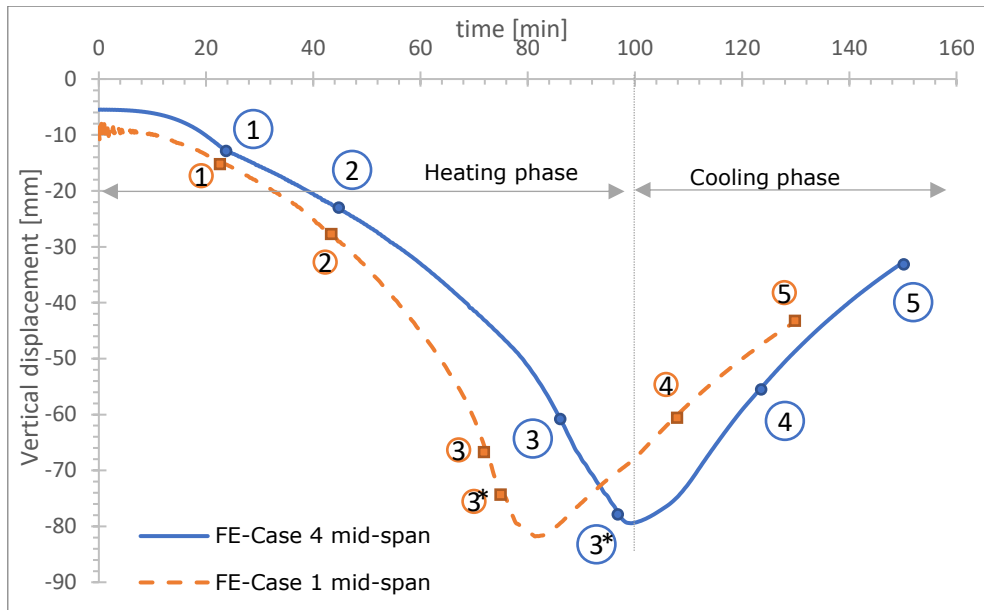


Figure 4-61: Vertical mid-span deflection as a function of time in case 4

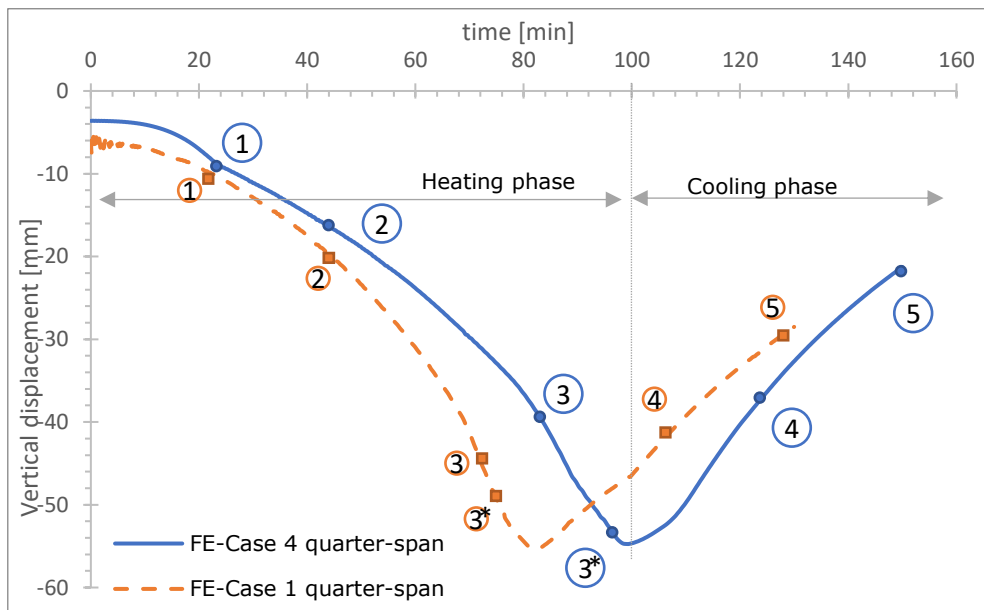


Figure 4-62: Vertical quarter-span displacement of the beam as a function of time in case 4

4.6.2 Behaviour of shear studs at different load ratios

Figure 4-63 shows the temperature development of shear studs close to the beam end in different studied cases. In Cases 1 and 3, the shear stud showed similar temperature development during the heating and cooling phases. In Case 2, the steel beam was heated similarly in the web and the bottom flange as in Case 1 and Case 3 but no heat transfer was defined on the unexposed surface of the top flange. Therefore, the top flange had higher temperatures, thus leading to higher temperatures in the shear stud. In Case 4, the shear stud showed similar temperature development as Cases 1 and 3 except that it reached a higher temperature in a long time because the beam model in Case 4 was heated till the bottom flange was 685°C. The shear studs' temperatures when the heating phase ended were around 255°C for Case 1 and 3, 418°C for Case 2, and 310°C for Case 4.

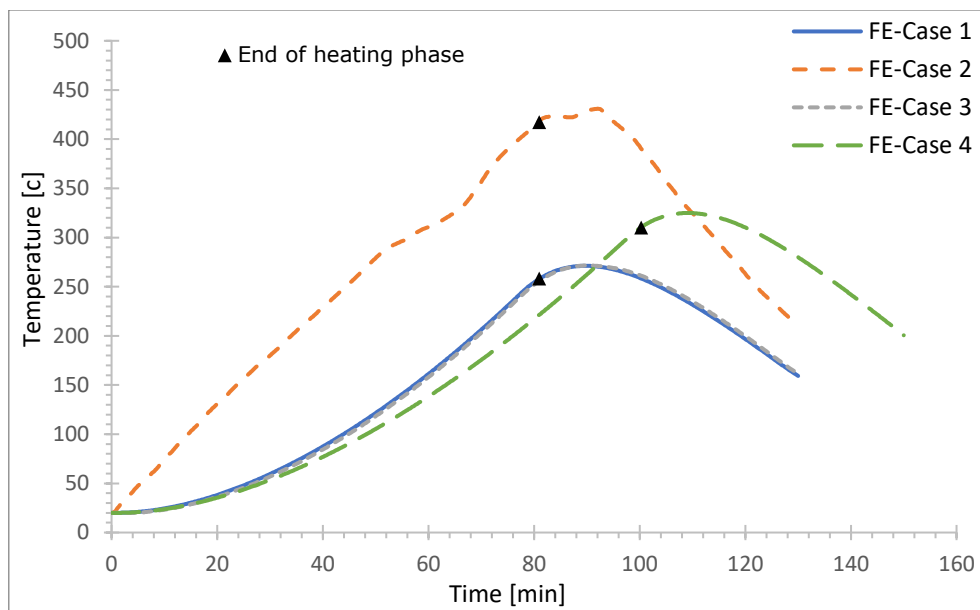


Figure 4-63: Temperature histories in the shear studs

Figure 4-64 shows the max slip at the connecting point between the shear stud at the end of the beam and the top flange for Cases 1, 2, and 4. In terms of four stages mechanism the slip of the shear stud in Case 1 can be explained as follows:

- Stage I (0-1): no slip in the shear stud was observed until point 1 when the steel beam reached 100°C. The elastic modulus of steel degraded at around 100°C.
- Stage II (1-3): The slip of the shear stud increased gradually with the temperature rise until point 2. After that, the slip of the shear stud increased sharply but stopped increasing around 40 min. Between 40 min and 75 min (point 3), the slip kept constant. Before 40 min, the material properties of the steel beam degraded. Between 40 min and 75 min, the temperature of the shear stud gradually increased from 100°C to 230°C during which the stiffness of the shear stud degraded.
- Stage III (3-4): During this stage, the slip of the shear stud increased sharply till the cooling stage started. The temperature of the shear stud reached 300°C.

- Stage IV (4-5): the slip of the shear stud is reversed till the end of the cooling stage. However, the residual slip was observed at the end of this stage.

In Case 2, the slip of the shear stud increased linearly with time up to point 3 because the temperatures of the shear stud increased linearly from 100°C to 300°C. At this range of temperatures, both stiffness and strength of the shear stud degraded. Between point 3 and the start of the cooling stage, the slip of the shear stud showed a sharp recovery before the cooling stage started due to the compression strength of the concrete degradation. The temperatures of the shear stud reached around 400°C. At this temperature, the compression strength of the concrete degraded heavily. After that, the slip of the shear stud increased slightly due to the degradation of the strength of the shear stud but started to recover till the end of the cooling stage.

In Case 4, the slip of the shear stud followed the trend of the shear stud in Case 1 up to point 2. After that, the slip of the shear stud showed constant slip as in Case 1 and a sharp increase as in Case 4 till point 3 due to the degradation of the stiffness and the strength of the shear stud. After point 3, the slip of the shear stud recovered noticeably before the cooling stage started due to the compression strength of the concrete degraded. During the cooling stage, the slip of the shear stud recovered but had residual slips till the end.

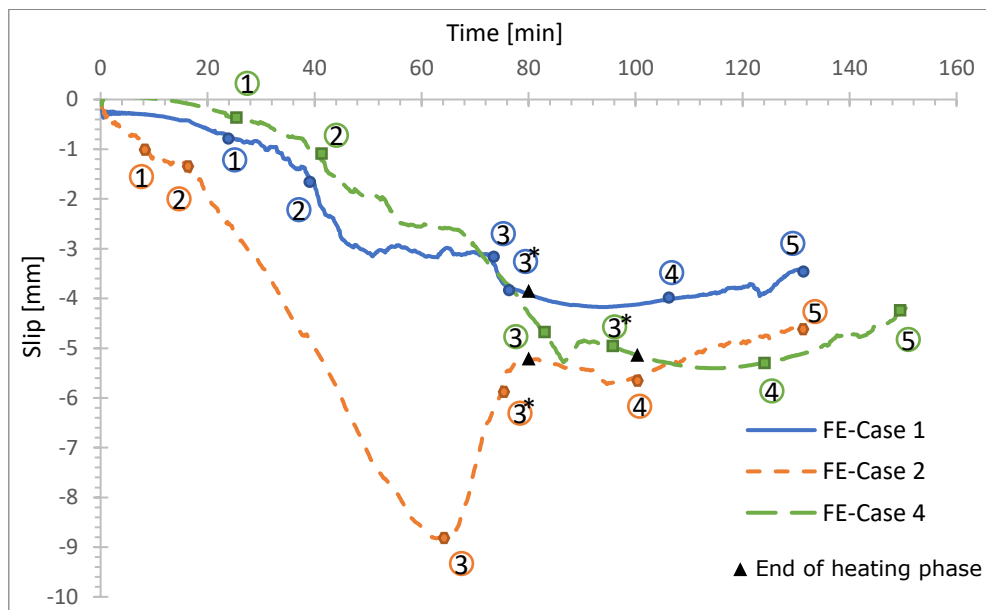


Figure 4-64: Shear studs' slip as a function of time

For the studied cases, the slip of the shear stud depended on the temperature development of the steel beam, shear stud, and concrete slab. Before the shear stud reached 100°C, the slip of the shear stud was due to the degradation of the material properties of the steel beam. Between 100°C and 300°C, the slip of the shear stud at the beam end kept constant due to the degradation of the stiffness of the shear stud. Between 300°C and 400°C, the slip of the shear stud had a sharp recovery due to the degradation of concrete strength. During the cooling stage, the

slip of the shear stud recovered but with residual slip at the end of the cooling stage.

The slip of the shear stud was affected by material degradations of steel beam, shear stud, and concrete can be visualized by the maximum absolute principal stress contour of the bottom surface of the concrete slab. The stress contour at point 0, point 3, point 3*, point 4, and point 5 for case 2 are shown in Figure 4-65 and Figure 4-66

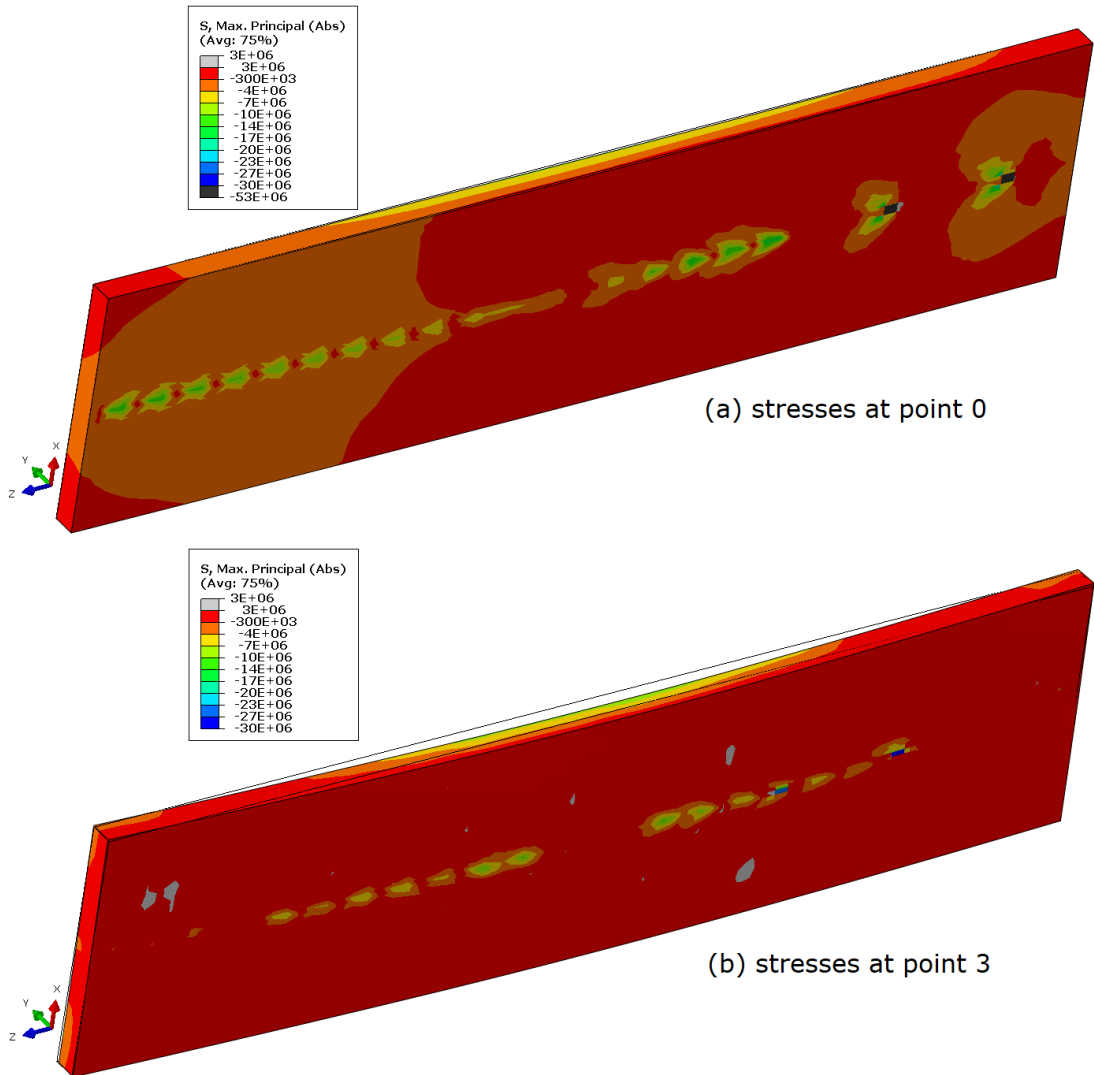


Figure 4-65: Maximum absolute principal stress contour at the bottom surface of concrete slab at (a) Point 0 (b) Point 3

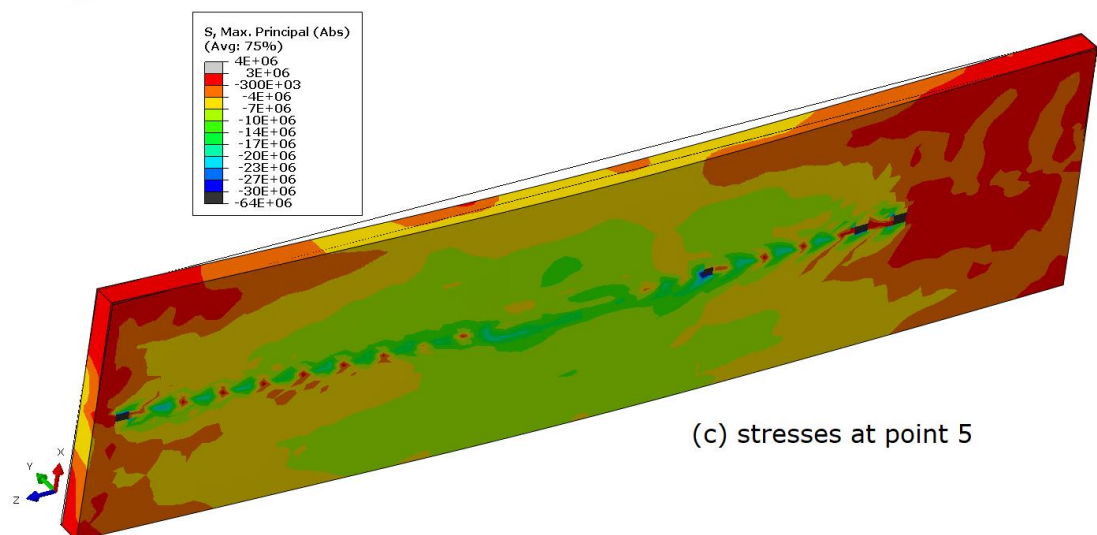
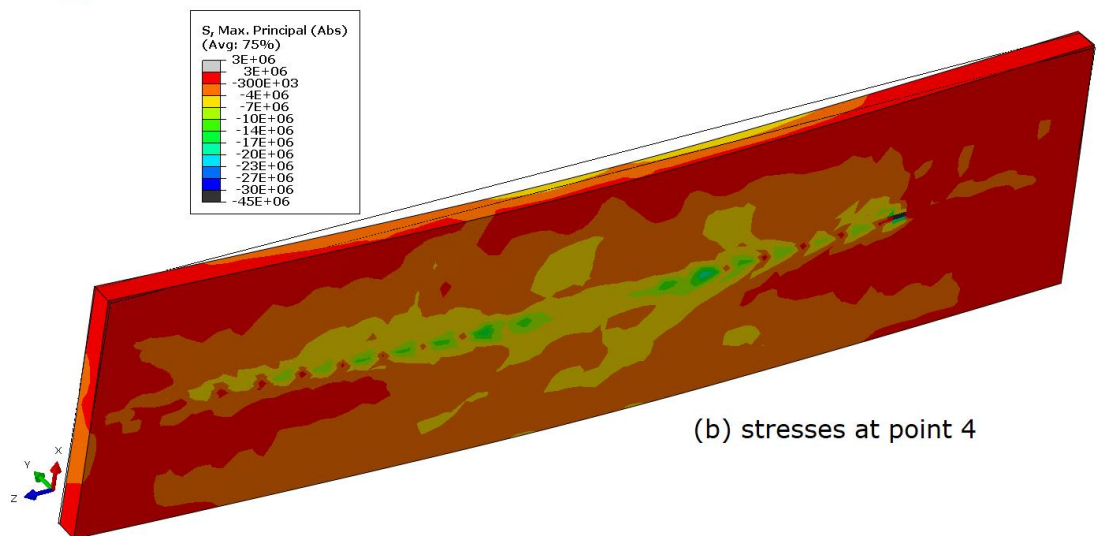
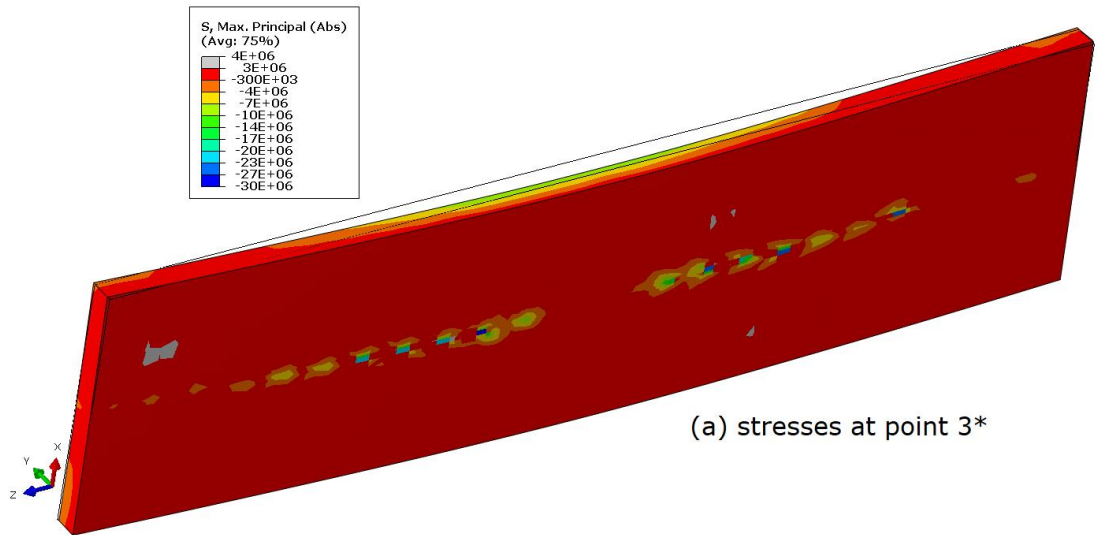


Figure 4-66: Maximum absolute principal stress contour at the bottom surface of concrete slab at (a) Point 3* (b) Point 4 (c) Point 5

4.6.3 Behaviour of beam-to-column connections at different load ratios

During the heating phase and due to thermal expansion, large compression axial force was produced at the beam end connections with temperature increasing. The compression force was limited by the local buckling capacity of the shear plate and beam web at elevated temperatures. As the temperature in the beam kept increasing, significant steel strength and stiffness loss occurred and led to large deflections of the beam and large rotations of the connections. When the beam was saged, the compression caused by the thermal expansion was compensated by the beam deflection until axial tension is developed in the beam and connections due to the controlled cooling phase. A large amount of stress was generated on the beam during the cooling stage, and the tensile axial force increased rapidly as the temperature dropped. This high tension during the cooldown led to connection failure.

Figure 4-67 and Figure 4-68 show the von Mises stresses in the connection region shear plate and bolts at the maximum compressive axial force during the heating phase point 2 in Figure 4-44, Figure 4-46 and Figure 4-60. As shown in Figure 4-67 and Figure 4-68, the von Mises stresses in the bolts are approaching but not exceeding the ultimate strength through the bolt section. Similarly, Figure 4-69 and Figure 4-70 show the von Mises stresses in the connection region at the maximum tensile axial force during the cooling phase point 5 in Figure 4-44, Figure 4-46 and Figure 4-60. As shown in Figure 4-69 and Figure 4-70, the von Mises stresses in the shear plate exceeded the steel yield strength, which eventually led to their failure. The failure in the test was along the weld line and in the FE model the weld was modelled as tie interaction, therefore no fracture was observed in ABAQUS while the stresses in the bolts did not exceed the yield strength.

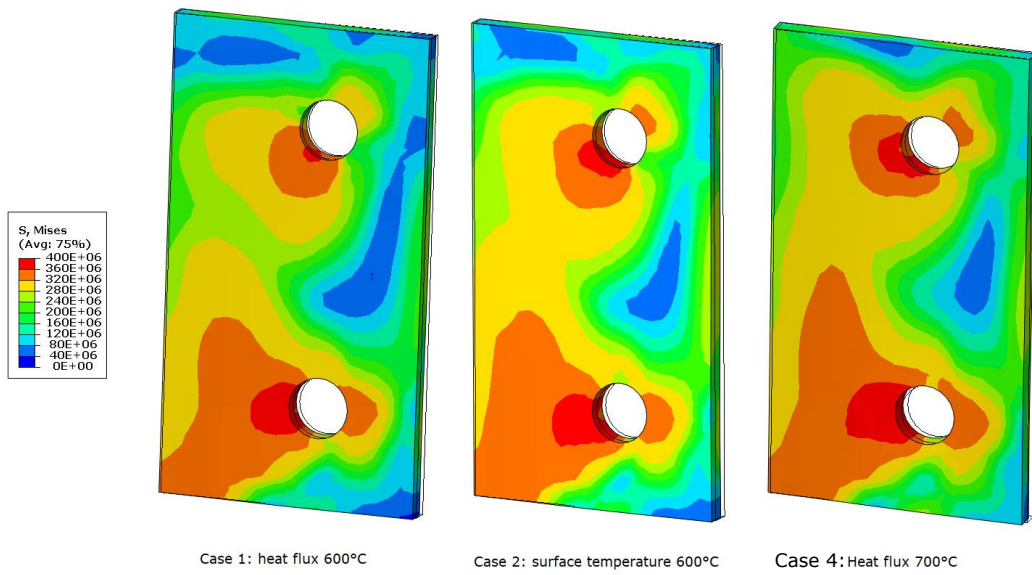


Figure 4-67: Von-Mises stress in the shear plate at Point 2

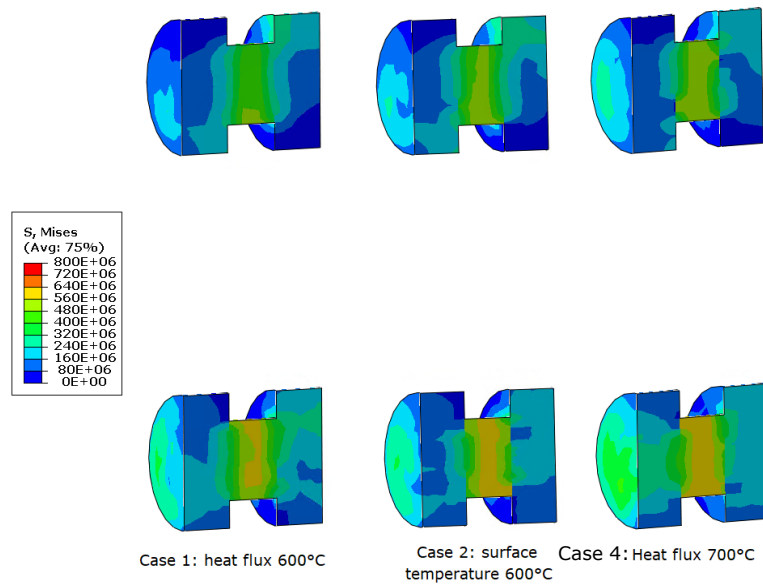


Figure 4-68: Von-Mises stress in bolts at Point 2

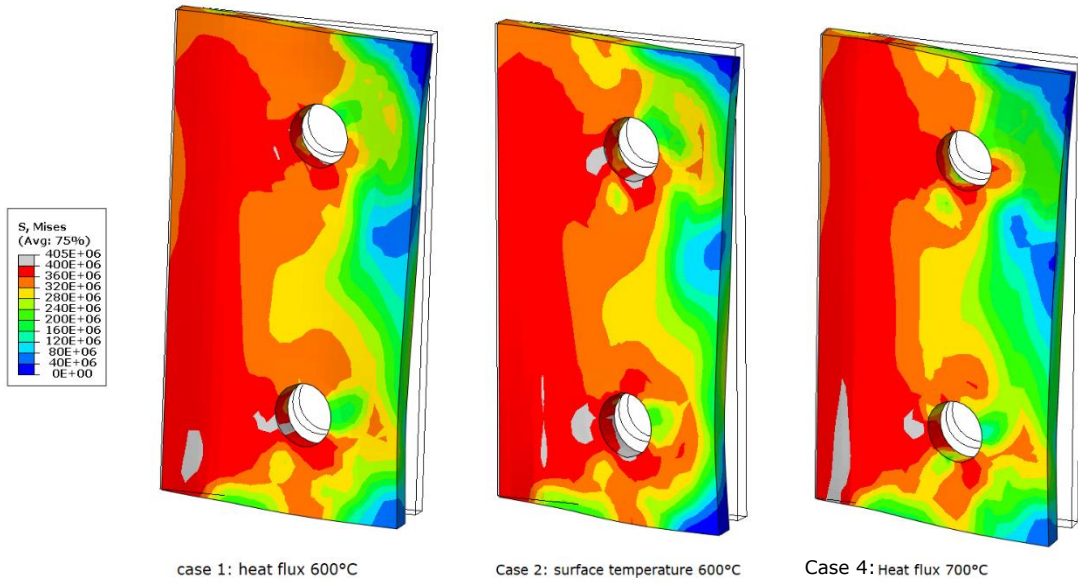


Figure 4-69: Von-Mises stress in the shear plate at Point 5

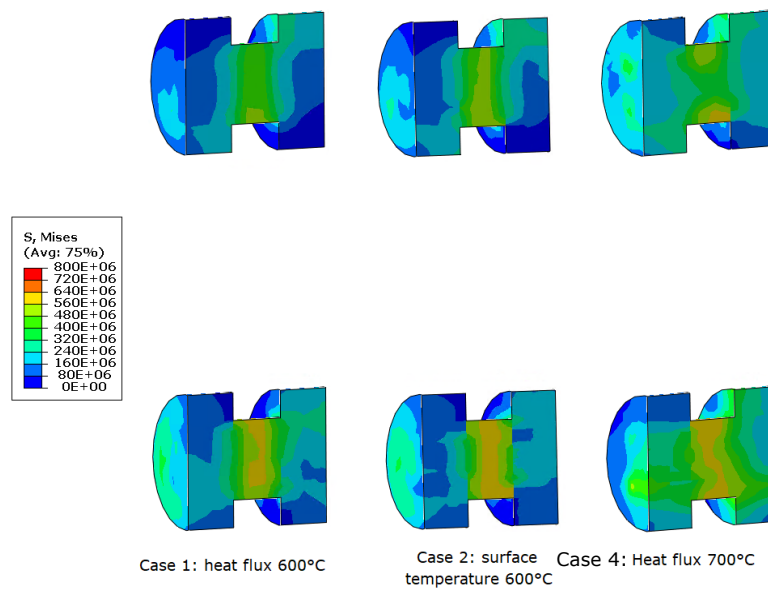


Figure 4-70: Von-Mises stress in bolts at Point 5

5. CONCLUSIONS AND FUTURE RESEARCH

This report investigated the behaviour of an unprotected structural steel-concrete composite beam exposed to fire. The commercial general-purpose finite element software ABAQUS has been used to analyze both a steel beam and a composite beam exposed to fire. Firstly; the pin-pinned steel beam with theoretically idealised boundary conditions was considered. Verification was made with hand calculations based on EN1993-1-2 [2005]. Secondly, the composite beam connected to columns with a shear plate connection was analyzed. The beam was exposed to the fire with a slow heating rate and a controlled cooling rate with different loading conditions. The columns in this analysis were treated as being fully protected, and therefore remain at ambient temperatures. The finite element model of the composite beam was validated with the results of the test experiments that were conducted at Purdue University. The validated models were further used to study the load-bearing mechanism of composite beams exposed to fires.

The structural fire design process included a fire behaviour model, a thermal response model and a structural response model. The fire behaviour model estimated the realistic gas temperature over the structural member during the fire. The thermal response model predicted the temperature distribution in structural members during the fire, and the structural response model predicted the structural response of structural members when mechanical loading and fire were present in the structure. The verification of the steel beam exposed to the nominal fire and the validation of the composite beam showed the accuracy of the coupling of thermal and mechanical analyses. Different methods were used to define the fire load during the thermal response model ie; heat flux and surface temperature. The heat flux method represented a more realistic situation in the fire. However, the surface temperature method was used to validate the model with the test results because the method represents the test conditions well. The structures simulated in this thesis were simple steel beam and composite beam connected to columns with shear plates exposed to fire. It was discovered that there was good agreement between FE models and measurement results. This research work was used for performing 3D thermal analysis using Abaqus/Standard and performing 3D structural analysing using Abaqus/Explicit dynamic procedure for modelled elements.

Composite beam behaviour was quite similar to the steel beam exposed to fire, which was expected as the steel material represented a large proportion of the composite cross-section. Therefore, the steel behaviour domain during fire events. However, the concrete slab assisted in decreasing the top flange temperature which reduced the average temperature of the cross-section and granted the composite section more strength than the steel beam individually. Different methods used in thermal analyses led to different load-carrying mechanisms in the beam depending on the average temperature of the cross-section. Depending on the axial forces at the beam end, four-stage mechanisms were defined according to the dominating actions through the beam.

- Stage I: the axial compression forces developed during the early stage of the heating because of the restrained boundary conditions that prevented the beam from expanding.

- Stage II: the material started to degrade and the bending of the beam took control until a hing behaviour formed.
- Stage III: axial compression forces decreased when the beam was about to run away as the temperature kept increasing. The large deformation at this stage activated the axial tension forces inside the beam which led to catenary action behaviour in the steel beam case and restrained thermal contraction in the composite case as the cooling stage started.
- Stage IV: the axial forces were completely in tension because of the restrained thermal contraction of the composite beam in the cooling phase and catenary action in the steel beam which prevent the beam from run-away.

The contribution of the top flange strength, shear studs and concrete close to shear studs were clearly observed through the relative slip in the model using the surface temperatures as input. While in the heat flux model due to the top flange and shear studs' low temperature the relative slip was not clearly observed. The behaviour of the shear studs was defined according to the four-stage mechanism. Slip recovery was noticed during the second stage. The slip recovery depended on the temperature of the shear stud and the concrete temperature near the shear stud: the higher the temperature was, the high the slip recovery occurred. The recovery is due to the material degradation of the steel beam, shear stud, and the concrete close to the shear stud.

Out-of-plane deformation was observed in the shear plate at elevated temperatures. The shear plate did not exceed the connection strength associated with the bolt shear failure during the loading and heating phases. The axial force-time histories from the FE model and estimated the failure mode in the shear plate connection along the welding line with fracture during the cooling phase. However, due to the tie method that has been used to model the weld, the fracture was difficult to occur. Therefore, modelling the weld connection with the exact stiffness parameter would show more accurate behaviour in the model.

The FE model should be used for further numerical studies under different loading and fire scenarios ie; parametric fire and travelling fire. Studying the behaviour of a simple shear connection will show more insightful information about the failure of the connection during the cooling phase. A better understanding of the behaviour of the connection will improve the design and detailing for fire resistance in steel-frame buildings. Further studies on the behaviour of the shear connectors and how they contribute to the fire resistance of the beam during the fire are also recommended.

SUMMARY

This thesis focuses on studying the thermal and mechanical behaviour of composite beams with simple shear beam-to-column connections subjected to vertical loads and fire conditions including heating and cooling phases. The simple shear connection was a shear -tab welded to the column and bolted to the beam web which is one of the most commonly used connections. All the structural components including steel beam, concrete slab, shear studs and connection elements (plates, bolts) were modelled in detail with ABAQUS using appropriate finite elements, contact interaction models, and material properties at elevated temperatures. The finite element model was validated with results from large-scale tests of composite beams and connections subjected to loading, heating and cooling phases. Different parameters including node temperature histories and vertical displacement at mid-span and quarter-span were compared with the test results. The composite beam was able to sustain the load with heating to the steel beam up to 700°C. However, the shear plate fractured during the cooling phase due to restrained thermal contraction. A four-stage mechanism was defined according to axial forces developed in the beam during the heating and cooling phases. The contribution of the shear studs to the beam response matched the four-stage mechanism well. The understanding of the behaviour of the composite beams and their connection to columns exposed to fire with heating and cooling phases helps to improve the structural fire resistance of the steel-concrete composite frames.

Keywords: structural fire resistance, steel beams, composite beams, beam-to-column connections, shear connectors, master thesis

KOKKUVÕTE

See lõputöö keskendub vertikaalsetele koormustele ja tuletingimustele, sealhulgas kütte- ja jahutusfaasidele allutatud lihtsate nihkeühendustega komposiittalade termilise ja mehaanilise käitumise uurimisele. Lihtne nihkeühendus oli posti külge keevitatud ja poltidega kinnitatud nihkeühendus, mis on üks sagedamini kasutatavaid ühendusi. Kõik konstruktsioonikomponendid, sealhulgas terastala, betoonplaat, lõikepoldid ja ühenduselemendid (plaadid, poldid) modelleeriti üksikasjalikult ABAQUS-iga, kasutades sobivaid lõplikke elemente, kontakti interaktsiooni mudeleid ja materjali omadusi kõrgendatud temperatuuridel. Lõplike elementide mudel valideeriti koormus-, kuumutamise- ja jahutusfaasis allutatud komposiittalade ja ühenduste suuremahuliste katsete tulemustega. Testitulemustega võrreldi erinevaid parameetreid, sealhulgas sõlmede temperatuuri ajalugu ja vertikaalne nihe kesk- ja veerandvahemikus. Komposiittala suutis taluda koormust terastala kuumutamisel kuni 700°C. Kuid nihkeplaat purunes jahutusfaasis vaashoitud termilise kokkutõmbumise tõttu. Neljaastmeline mehhanism määratleti vastavalt talas kütte- ja jahutusfaasis tekkivatele teljesuunalistele jõududele. Polttüüblide panus tala reageerimisse sobis hästi neljaastmelise mehhanismiga. Komposiittalade käitumise mõistmine ja nende ühendamine kütte- ja jahutusfaasidega tulele avatud postidega aitab parandada terasbetoonkomposiitkarkasside konstruktsioonilist tulepüsivust.

Võtmesõnad: Konstruktiivne tulikindlus, terastalad, komposiittalad, tala-posti ühendused, polttüüblid, magistritöö

REFERENCES

- [1] G. Brambilla, M. Lavagna, G. Vasdravellis and C. A. Castiglioni, “Environmental benefits arising from demountable steel-concrete composite floor systems in buildings,” 2018.
- [2] S. Shinde, P. Minde and M. Kulkarni, “Analysis of LGS- ferrocement composite construction technology as a cost-effective & sustainable alternative to RCC,” 2022.
- [3] V. Albero, A. Espinós, E. Serra, M. Romero and A. Hospitaler, “Numerical study on the flexural behaviour of slim-floor beams with hollow core slabs at elevated temperature,” 2018.
- [4] O. Vassart, B. Zhao, R. Hamerlink, B. Hauke, J. de la Quintana, I. Talvik, Z. Sokol, S. Pustorino, P. Vila Real, M. Hawes, A. Nadjai, B. Åstedt, K. Jarmai, R. D. Zaharia, A. K. Kvedaras, C. Baniotopoulos, D. Beg, J. M. Franssen and G. Wozniak, “Membrane action in fire design of composite slab with solid and cellular steel beams — Valorisation (MACS+),” RFCS Grant Agreement RFS2-CT-2011-00025, Final Report 2014.
- [5] J. Jiang, Y. Lu, X. Dai, G. Li, W. Chen and J. Ye, “Disproportionate collapse of steel-framed gravity buildings under travelling fires,” 2020.
- [6] E. Rackauskait, M. Bonner and F. Restuccia, “Fire Experiment Inside a Very Large and Open-Plan Compartment: x-ONE,” 2021.
- [7] G. Rein, X. Zhang and P. Williams, “Multi-storey fire analysis for high-rise buildings, in Proceedings of the 11th International Interflam Conference,” 2007.
- [8] F. McCann, L. Gardner and S. Kirk, “Elevated temperature material properties of cold-formed steel hollow sections,” 2015.
- [9] A. Buchanan, Structural Design for Fire Safety, 2002.
- [10] X. Zhao, R. Grzebieta, A. Ukur and M. Elchalakani, “Tests of concrete-filled double skin (SHS outer and CHS inner) composite stub columns,” 2002.
- [11] EN 1994-1-2 (2005): Eurocode 2: Design of composite steel and concrete structures - Part 1-2: General rules - Structural fire design, European Committee for Standardization (CEN).
- [12] V. Babrauskas and R. Williamson, “The historical basis of fire resistance testing— Part II, Fire Technol. 14,” 1978.

- [13] Fire Tests on Buildings Materials and Structures—Part 20:Method for Determination of the Fire Resistance of Elements of Construction, BS476-20, 1987.
- [14] Fire-resistance Tests—Elements of Building Construction—Part 1: General Requirements, ISO 834-1.
- [15] Standard Test Methods for Fire Tests of Buildings Construction and Materials, ASTM E119-00a, 2000.
- [16] D. Drysdale, An Introduction to Fire Dynamics, 2nd ed., 1998.
- [17] S. Manzello, W. Grosshandler and T. Mizukami, Furnace testing of full-scale gypsum steel stud non-load bearing wall assemblies: results of multilaboratory testing, 2010.
- [18] EN 1991-1-2 (2002). Eurocode 1: Action on structures. Part 1-2 General action. Action on structures exposed to fire, European Committee for Standardization (CEN).
- [19] J. Stern-Gottfried and G. Rein, “Travelling fires for structural design—Part I: Literature review,” 2012.
- [20] T. Lennon, Designer's guide to EN 1991-1-2, 1992-1-2, 1993-1-2 and 1994-1-2 handbook for the fire design of steel, composite and concrete structures to the eurocodes 0008. Designer's guides to the eurocodes 0011, London.
- [21] Fire safe design: A new approach to multi-storey steel framed buildings, The Steel Construction Institute, 2000.
- [22] C. Bailey, I. Burgess and R. Plank, “Analyses of the Effects of Cooling and Fire Spread on Steel framed Buildings Fire Safety Journal,” 1996.
- [23] R. Lawson, “Behaviour of steel beam-to-column connections in fire,” 1990.
- [24] Y. Yina and Y. Wang, “Analysis of catenary action in steel beams using a simplified hand calculation method, Part 1: theory and validation for uniform temperature distribution,” 2003.
- [25] M. Kodur and V. Dwaikat, “A performance based methodology for fire design of restrained steel beams,” 2010.
- [26] Y. Yin and Y. Wang, “A numerical study of large deflection behaviour of restrained steel beams at elevated temperatures,” 2003.
- [27] Guide to the advanced fire safety engineering of structures, Engineers Institution of Structural, 2007.
- [28] E. Fischer and A. Varma, “Fire behavior of composite beams with simple connections: Benchmarking of numerical models,” 2015.

- [29] S. L. Kristi, E. C. Fischer and A. H. Varma, "Experimental Investigation of Composite Beams with Shear Connections Subjected to Fire Loading," 2015.
- [30] E. C. Fischer, S. L. Kristi and A. H. Varma, "Experimental Evaluation of the Fire Performance of Simple Connections," 2016.
- [31] B. Zhao and J. Kruppa, "Fire resistance of composite slabs with profiled steel sheet and of composite steel concrete beams, part 2: composite beams. Luxembourg: European Commission," 1997.
- [32] Abaqus 6.13, Analysis User Guide, Dassault Systèmes, Providence, RI, USA, 2013.
- [33] EN 1993-1-2 (2005): Eurocode 2: Design of steel structures - Part 1-2: General rules - Structural fire design, European Committee for Standardization (CEN).
- [34] F. Dumonta, E. Wellensa, G. Thomas and J.-M. Franssen, "Loadbearing capacity criteria in fire resistance testing," 2016.
- [35] EN 1992-1-2 (2004): Eurocode 2: Design of concrete structures - Part 1-2: General rules - Structural fire design, European Committee for Standardization (CEN).